

Aus dem Max-Planck-Institut für Kolloid- und Grenzflächenforschung

The Geometry of Interacting Liquid Domains in Langmuir Monolayers

Dissertation
zur Erlangung des akademischen Grades
Doktor der Naturwissenschaften
(Dr. rer. nat.)
in der Wissenschaftsdisziplin Grenzflächenphysik

eingereicht an der
Mathematisch-Naturwissenschaftlichen Fakultät
der Universität Potsdam

von Peter Heinig
geboren am 25. Juli 1974 in Zschopau

Golm, 2. April 2003

Kurzzusammenfassung

Es werden die Strukturbildung und Benetzung zweidimensionaler (2D) Phasen von Langmuir-Monolagen im lokalen thermodynamischen Gleichgewicht untersucht. Eine Langmuir-Monolage ist ein isoliertes 2D System von Surfactanten an der Wasser/Luft-Grenzfläche, in dem kristalline, flüssigkristalline, flüssige oder gasförmige Phasen auftreten, die sich in Positionsordnung und/oder Orientierungsordnung unterscheiden. Permanente elektrische Dipolmomente der Surfactanten führen zu einer langreichweitigen repulsiven Selbstwechselwirkung der Monolage und zur Bildung mesoskopischer Strukturen. Es wird ein Wechselwirkungsmodell verwendet, das die Strukturbildung als Wechselspiel kurzreichweitiger Anziehung (nackte Linienspannung) und langreichweitiger Abstoßung (Oberflächenpotential) auf einer Skala Δ beschreibt. Physikalisch trennt Δ die beiden Längenskalen der lang- und kurzreichweitigen Wechselwirkung. In dieser Arbeit werden die thermodynamischen Stabilitätsbedingungen für die Form einer Phasengrenzlinie (Young-Laplace-Gleichung) und Dreiphasenkontaktpunkt (Young-Bedingung) hergeleitet und zur Beschreibung experimenteller Daten genutzt: Die Linienspannung benetzender 2D Tropfen wird mit Hilfe hängender-Tropfen-Tensiometrie gemessen. Die Blasenform und -größe von 2D Schäumen wird theoretisch modelliert und mit experimentellen 2D Schäumen verglichen. Kontaktwinkel werden durch die Anpassung von experimentellen Tropfen mit numerischen Lösungen der Young-Laplace-Gleichung auf Mikrometerskalen gemessen. Das Skalenverhalten des Kontaktwinkels ermöglicht die Bestimmung einer unteren Schranke von Δ . Weiterhin wird diskutiert, inwieweit das Schalten von 2D Benetzungsmodi in biologischen Membranen zur Steuerung der Reaktionskinetik eine Rolle spielen könnte. Hierzu werden Experimente aus unserer Gruppe, die in einer Langmuir-Monolage durchgeführt wurden, herangezogen.

Abschließend wird die scheinbare Verletzung der Gibbs'schen Phasenregel in Langmuir-Monolagen (nicht-horizontales Plateau der Oberflächendruck-Fläche Isotherme, ausgedehntes Dreiphasengebiet in Einkomponentensystemen) quantitativ untersucht. Eine Verschmutzung der verwendeten Substanzen ist demnach die wahrscheinlichste Erklärung, während Finite-Size-Effekte oder der Einfluss der langreichweitigen Elektrostatik die Größenordnung des Effektes nicht beschreiben können.

Abstract

The present work investigates the structure formation and wetting in two dimensional (2D) Langmuir monolayer phases in local thermodynamic equilibrium. A Langmuir monolayer is an isolated 2D system of surfactants at the air/water interface. It exhibits crystalline, liquid crystalline, liquid and gaseous phases differing in positional and/or orientational order. Permanent electric dipole moments of the surfactants lead to a long range repulsive interaction and to the formation of mesoscopic patterns. An interaction model is used describing the structure formation as a competition between short range attraction (bare line tension) and long range repulsion (surface potentials) on a scale Δ . Δ has the meaning of a dividing length between the short and long range interaction. In the present work the thermodynamic equilibrium conditions for the shape of two phase boundary lines (Young-Laplace equation) and three phase intersection points (Young's condition) are derived and applied to describe experimental data: The line tension is measured by pendant droplet tensiometry. The bubble shape and size of 2D foams is calculated numerically and compared to experimental foams. Contact angles are measured by fitting numerical solutions of the Young-Laplace equation on micron scale. The scaling behaviour of the contact angle allows to measure a lower limit for Δ . Further it is discussed, whether in biological membranes wetting transitions are a way in order to control reaction kinetics. Studies performed in our group are discussed with respect to this question in the framework of the above mentioned theory.

Finally the apparent violation of Gibbs' phase rule in Langmuir monolayers (non-horizontal plateau of the surface pressure/area-isotherm, extended three phase coexistence region in one component systems) is investigated quantitatively. It has been found that the most probable explanation are impurities within the system whereas finite size effects or the influence of the long range electrostatics can not explain the order of magnitude of the effect.

Contents

1	Introduction	1
2	Experimental setup	3
2.1	Experimental techniques for Langmuir monolayers	3
2.2	Langmuir-trough	6
2.3	Fluorescence microscope combined with optical tweezers	7
3	Interactions in monolayers	9
3.1	Long range electrostatic repulsion	9
3.2	Line tension represents short range attraction	12
3.3	Free energy	14
3.4	Mesoscopic pattern formation due to competition between long- and short-range interaction	15
4	Interfaces	17
4.1	Young-Laplace-equation in 3D	17
4.2	2D Young-Laplace-equation including long range interaction	18
4.3	Shape invariant scaling	19
4.4	Pendant droplet tensiometry in monolayers	19
4.4.1	Experimental	20
4.4.2	Numerical image analysis	21
4.5	Discussion	23
5	2D dipolar foams	25
5.1	Bubble shapes of ideal 2D foams are universal	26
5.2	Numerical calculation of bubble shapes	28
5.3	Experimental foams dry at predicted area fraction	30
5.4	Discussion	32

6	2D wetting	33
6.1	Contact angles in macroscopic 3D systems	34
6.2	Contact angles in 2D with dipole interaction	36
6.2.1	2D Young-condition	36
6.2.2	Scaling laws	36
6.2.3	Fitting contact angles with numerical solutions of the Young-Laplace-equation	38
6.2.4	Conclusion: cut-off-length Δ is a mesoscopic quantity	41
6.2.5	Discussion	45
6.3	Shape instabilities of wetting droplets	45
6.3.1	Theory	46
6.3.2	Experiment	48
6.3.3	Discussion	49
7	Biological control of wetting transitions	51
7.1	Controlling of wetting behaviour - theoretical approach	52
7.2	Enzymatic control of wetting behaviour in biomimetic system	54
7.2.1	Fundamentals - lipid-enzyme reactions in membranes	54
7.2.2	Experimental - PLA ₂ hydrolysis of DPPC/cholesterol mixture	55
7.3	Discussion	57
8	Apparent violation of Gibbs' phase rule in monolayers	59
8.1	First order phase transition and Gibbs' phase rule	59
8.2	Violations of Gibbs' phase rule observed in monolayers	60
8.3	Influence of electrostatics	62
8.3.1	Dipole pressure contribution in isotherm	62
8.3.2	Electrostatics smears triple point	62
8.4	Finite size effects become important on nm scale	64
8.4.1	Mixing entropy due to cluster formation	64
8.4.2	Curved interfaces stabilize particles smaller than 1 nm	67
8.5	Impurity could explain the apparent violation of Gibbs' phase rule	68
8.6	Summary	71
9	Summary	73
A	Appendix	77
A.1	Relative potentials	77
A.2	Variation problem	78

A.2.1	Young-Laplace equation	78
A.2.2	Young's equation	80
A.3	Line integral expression of dipolar energy and pressure	80
A.4	Scaling laws	81
A.4.1	shape invariant scaling	81
A.4.2	contact angle invariant scaling	83
A.5	Foam energy minimization	84
A.6	Numerical solution of the Young-Laplace-equation for an ideal foam	84
A.7	Numerical solution of the Young-Laplace-equation for a pendant droplet	85
A.8	Lower limit for phase specific cut-off lengths Δ_i	87
A.9	Mass action law for monomer-cluster reaction considering entropy in the cluster size	88
A.10	Monolayer isotherm with impurity	89
A.11	Software	90
A.11.1	Manual	90
A.11.2	Multimeters	90
A.11.3	Stepper motors	92
Miscellaneous		i
	List of publications	i
	Conferences and talks	ii
	Curriculum vitae	iii
	Acknowledgements	iv
	Thesen	v

List of often used symbols

A	area
α (α_i)	molecular area (of phase i)
Δ (Δ_i)	scale parameter (of phase i)
ϵ (ϵ_r, ϵ_0)	permittivity (relative~, in vacuum)
F ($F_{\text{el}}, F_\lambda, F_0$)	free energy (dipole contribution, line contribution, 2D bulk contribution)
i, j, k, l	counting index variables
κ (κ_{ij})	curvature (of interface ij)
λ (λ_{ij})	<i>bare</i> line tension (between phase i and j)
μ (μ_i, μ_{ij})	dipole density parameter (of phase i , $\mu_i - \mu_j$)
N	number of molecules, domains, or microstates
\mathbf{n}, \mathbf{n}'	normal vector
p (p_{ij})	Laplace pressure (across the interface ij) parameter characterizing the unidealty of mixing
p_{el}	electrostatic pressure
Φ (Φ_i)	area fraction (of phase i)
ϕ	angle shape parameter
π	surface pressure
R	radius
\mathbf{r} ($\mathbf{r}_{ij}, \mathbf{r}_{ij}(s)$)	position vector in 2D (pointing to interface ij , shape of interface ij)
S	entropy
σ	surface tension
T	temperature
\mathbf{t}, \mathbf{t}'	tangent vector
θ	contact angle
V (V_i)	surface potential (of phase i)
ξ	correlation length
ξ_i (ξ_{ij})	molecular bulk energy (latent heat of phase transition from phase i to j)
\bar{Q}	mean value of the quantity Q
$\langle Q \rangle$	expectation value of Q
\tilde{Q}	corresponding dimensionless quantity to Q
Q^*	corresponding renormalized quantity to Q
\tilde{Q}^*	corresponding renormalized dimensionless quantity to Q
Q_r	physical ('real') value of Q

Chapter 1

Introduction

Surfactants are molecules with a hydrophilic head group and a hydrophobic chain (figure 1.0.1). According to their amphiphilic nature they favour the formation of mono molecular layers on the air/water interface. Depending on the solubility one distinguishes between Gibbs monolayers and Langmuir monolayers. Gibbs monolayers are formed by soluble surfactants. The monolayer is in equilibrium with molecules in solution. Insoluble surfactants form Langmuir monolayers - isolated quasi 2D systems on the air/water interface. In general the length of the hydrophobic chain determines the solubility of the molecule in water, the longer the chain the less soluble the molecule.

The molecules show several degrees of freedom and various phases differing in rotational, translational or positional order occur. One observes gases, liquids or crystals according to translational order or tilted and untilted phases according to the rotational order of the chain. Langmuir monolayers are an excellent system to study complex thermodynamic behaviour

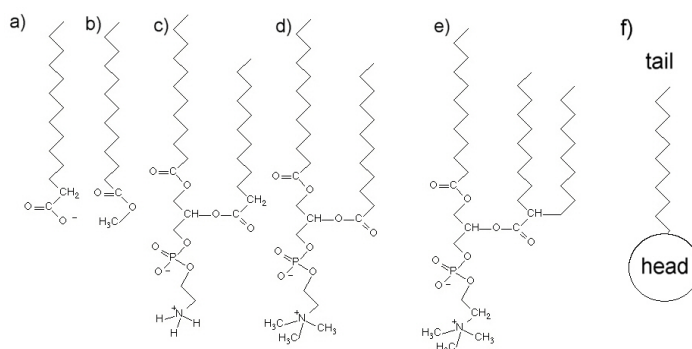


Figure 1.0.1: typical surfactants are a) fatty acid, b) methyl ester, c)-e) phospholipids, c) diacylphosphatidylethanolamine, e) diacylphosphatidylcholine. f) schematic sketch: all surfactants consist of a hydrophilic head (soluble in water) and a hydrophobic chain (not soluble in water)

with relatively simple experimental devices. The variables of state: area A , surface pressure π or temperature T are easily accessible by measurement and can be controlled. Structures can be monitored by imaging techniques. Langmuir monolayers are an ideal model system for several biological problems. For instance for lung surfactants which lower the surface tension within the lung and make breathing possible. Or for biological membranes - bilayers of amphiphilic lipids exhibiting complex structures and functions. From the physical point of view Langmuir monolayers give the opportunity to study thermodynamics in the presence of long range interactions. Since the dipole moments of the molecules are not screened at the air/water interface long range interaction influences the phase behaviour and causes the formation of self assembling patterns. By the Langmuir-Blodgett technique monolayers can be transferred on a solid substrate and one can create well defined materials on molecular scale. In the present work the effect of the dipole interaction is studied with respect to the phase behaviour, stability size and shape of two dimensional (2D) foams and especially to the wetting behaviour of 2D phases. Controlling the wetting behaviour is an essential task in technology, for instance for the design of lubricants or dyes, the design of self assembling patterns or microfluidic systems (the lab on a chip). A special field of wetting research focuses on long range interaction wetting, a feature for which Langmuir monolayers are well suited.

The present work will be ordered as follows: In chapter 2 an overview of experimental techniques used for monolayer research is presented and the experimental setup used for the experiments is presented here. Chapter 3 gives a description of the common theoretical model based on a competition between short range attraction and long range repulsion and important conclusions are presented. Then chapter 4 derives the thermodynamic equilibrium conditions for the shape of phase interfaces and applies those to experimentally observed monolayer patterns. On the one hand these conditions are used to describe the drying of 2D long range interaction foams (section 5). On the other hand they are used to study features of 2D long range interaction wetting in chapters 6 and 7. Chapter 8 deals with possible explanations for an apparent violation of Gibbs' phase rule in monolayers.

Chapter 2

Experimental setup

2.1 Experimental techniques for Langmuir monolayers

Most experiments on Langmuir monolayers are performed in a Langmuir trough. A sketch of the principle design is shown in figure 2.1.1. The trough is made of hydrophobic material (teflon) and usually equipped with movable hydrophobic barriers. With the barriers the total area accessible to the surfactant molecules on the surface can be varied. The presence of amphiphiles on the interfaces generally decreases the surface tension. The difference of the surface tension with surfactant σ to the surface tension of a pure subphase σ_0 is called the surface pressure $\pi := \sigma_0 - \sigma$ (unit mN/m). It has the dimension of a 2D pressure (energy per area) or 2D elasticity. Analog to 3D pressure-volume isotherms in Langmuir monolayers $\pi - A$ isotherms can be measured. Like in 3D, discontinuities in the isotherms indicate phase transitions. The surface tension is determined by measuring the force caused by the surface on a completely wetted plate (Wilhelmy - plate). This can be done by a balance ('film-balance') or by an electronic force sensor. Usually the trough is equipped with some external thermostat in order to control the temperature.

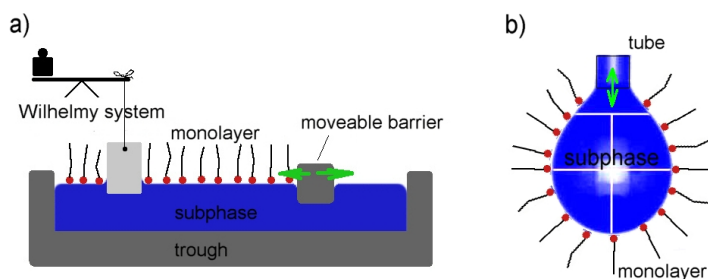


Figure 2.1.1: schematic sketch of a) Langmuir trough with Wilhelmy-sensor for surface-pressure-measurement and moveable barrier b) Pendant droplet technique. The surface tension (and surface pressure) can be evaluated out of the droplet shape.

The Langmuir trough can also be used for Langmuir-Blodgett technique [1]. By dipping a solid plate into the trough the monolayer is transferred layer by layer onto the solid substrate. The surface pressure is kept constant during this procedure and the loss of material on the air water interface is compensated by moving the barriers.

Another method of measuring the surface tension makes use of the dependence of the shape of pendant droplets in gravitational field on the surface tension and droplet volume (pendant droplet tensiometry) [2]. The pendant drop device allows to vary the volume of pendant (or sessile) droplets and with the volume also the surface area accessible to the surfactant. The surface tension can be calculated by analysis of the droplet shape, which has to be recorded by a camera. The advantage of this technique is the small total volume of subphase and a fast relaxation of the droplet shape. This setup is interesting especially for studying the adsorption dynamics of soluble surfactants. A disadvantage of the latter technique arises due to the difficulty to add additional imaging technique for the investigation of the monolayer pattern itself.

Since the 80's imaging techniques were developed enabling the observation of the monolayer structure. (Normal optical microscopy fails because the monolayer is too thin to be observed directly.) Lösche et al. [3] and McConnell et al. [4] labelled the amphiphiles with a fluorescent dye (nitrobenz-oxa-diacole (NBD) and Texas-red respectively) and observed the monolayer through a filter for the fluorescence light by a normal optical microscope. The monolayer has to be illuminated by light of a certain frequency ν_{EX} (see figure 2.1.2), usually lasers or mercury lamps (only narrow bands in the spectra) are used as light sources. The obtained

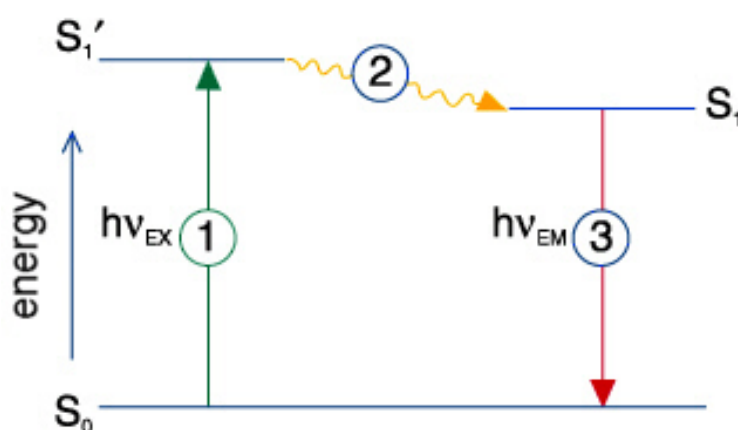


Figure 2.1.2: Exciting light with the energy $h\nu_{\text{EX}}$ is adsorbed and lifts an electron from energy level S_0 to S_1' (step 1). By radiation less processes, as impacts, the electron loses some energy and reaches energy level S_1 (step 2). Then the electron goes back to S_0 emitting light with the energy $h\nu_{\text{EM}} < h\nu_{\text{EX}}$.

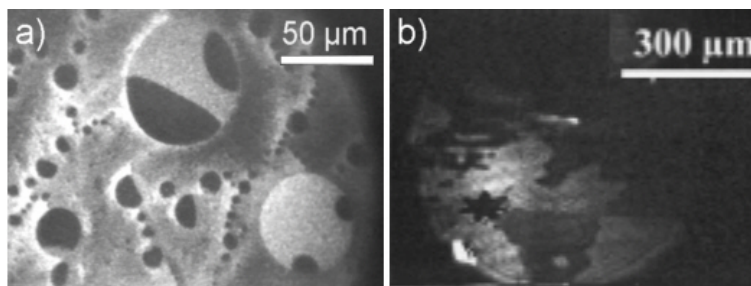


Figure 2.1.3: a) Image of methyl octadecanoate monolayer using polarized fluorescence microscopy. The matrix phase is liquid condensed phase (inhomogeneous in brightness because of unisotropy), with circular enclosures containing gaseous phase (dark, homogeneous) and liquid expanded phase (bright, homogeneous). b) BAM image of tilted phase in octadecanol monolayer. The regions of different brightness correspond to different directions of the molecule tails. Regions with low monolayer concentration reflect completely polarized light (black star) [7].

microscopy image corresponds to the distribution of the label in the monolayer. In general gaseous phases appear dark because of fluorescence quenching and the low density of molecules. 2D liquids appear bright. Because the labelled molecules differ in shape compared to the unlabelled molecules they are seldom built into an ordered lattice. This is the reason why in the fluorescence image ordered 2D phases occur less bright than the 2D liquids, but often brighter than gas phases. If polarized exciting light is used, only dye molecules within a certain angle are excited. With this technique (polarized fluorescence microscopy) tilt angles can be visualized by slight variations in the brightness. Condensed phases can be better distinguished from gaseous phases because of their inner structure (see figure 2.1.3). So fluorescence microscopy is easy to handle and allows to distinguish phases differing in orientational and positional order as well as in rotational order to some extent. The maximum resolution is limited by the wavelength of the fluorescence light ($< 1 \mu\text{m}$). One disadvantage of this technique is the always present fluorescence label which acts in the system as trace impurity and might influence the thermodynamic behaviour.

A common technique in order to study anisotropic properties of monolayers is the Brewster angle microscopy (BAM). This method was introduced by Hönig and Möbius [5] and Hénon and Meunier [6] and does not need any dye. A laser beam hits the surface in the Brewster angle and completely polarized light is reflected. The presence of monolayer influences the polarization of the reflected beam. Using a microscope images of the monolayer can be obtained. This technique is very useful in order to distinguish tilted and untilted phases. Phases without any rotational order, however, cannot be distinguished in the BAM image. The resolution is limited by the tilt of the local phase with respect to the air/water interface.

Other common techniques for the determination of the molecular structure in monolayers are

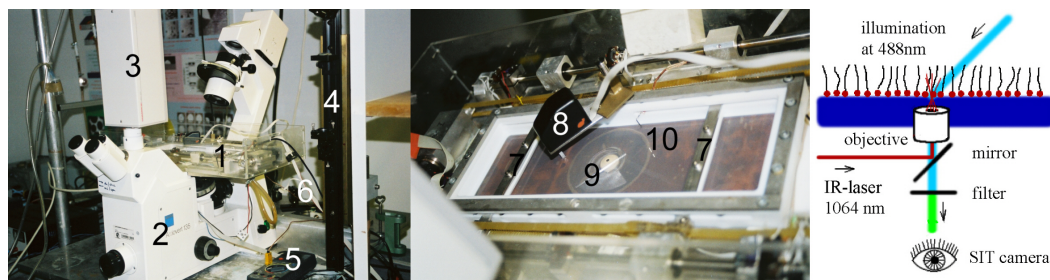


Figure 2.2.1: left: fluorescence microscope. 1 - Langmuir trough; 2 - microscope; 3 - SIT camera head; 4 - optics for fluorescence laser; 5 - Multimeter for temperature measurement; 6 - optics of IR-laser behind the microscope
middle: Langmuir trough. 7 - moveable barriers; 8 - Wilhelmy sensor; 9 - objective; 10 - temperature sensor
right: schematic principle of apparatus

electron microscopy [8], X-ray diffraction [9] or IR-spectroscopy [10]. Langmuir-Blodgett films can be further analyzed for instance using atomic force microscopy (AFM) [11].

2.2 Langmuir-trough

The trough for the experiments presented here was designed by Lautz and built by the author together with Steffen (figure 2.2.1). The walls and barriers are made of solid teflon and the bottom is covered with a teflon foil. The area can be varied by two symmetrical movable barriers between 211 and 58 cm² leaving the center of the film in rest. The barriers are moved by stepper motors (model: C-842) from PI. The motors are controlled via a PC card. The software is described in Appendix A.11. The area between the barriers is obtained by counting the steps of the motors, so it is not a direct measurement and demands calibration from time to time. The measurement error of the area does not exceed 1%. Vibrations are suppressed by a NFT vibration isolation system.

The surface pressure π is measured by Wilhelmy sensors working with an optical feedback circuit. One of the sensors was designed and manufactured by Kohlstrunk (university of Leipzig), later also a sensor of 'Riegler and Kirstein' working on the same principle was used. The time for the feedback circuit to reach its final value (tuning time) is about 30 s. Then the error of the measurement is about 1 mN/m. The measured pressure has been digitized by an AD transformer card (ADA 16-2) or by a multimeter (Metex-22, Digitek DT-4000ZC) connected to the PC via the RS232 interface.

The temperature can be controlled by Peltier-elements attached to the bottom of the trough. An electrical potential applied to Peltier-elements leads to a temperature difference on the two sides of the element. This feature can be used for heating and cooling dependent on the sign

of the applied potential. The Peltier-elements are manually controlled by laboratory power supply (EA-4021) and use the cooling circuit of the institute as heat reservoir with a defined temperature. The advantage of using this setup compared to the common external thermostat is that temperature changes can be performed very fast. Unfortunately the temperature distribution within the trough is not homogeneous and large temperature differences compared to the environment lead to convectional flow of the subphase.

The temperature is measured by an electronics assembly designed by Kohlstrunk using Pt100 elements and the AD transformer card or by a multimeter with RS232 interface and temperature measure function.

2.3 Fluorescence microscope combined with optical tweezers

The trough is combined with a fluorescence microscope built up by Lautz. An air cooled Argon laser from Optlectra (488 nm) with a power up to 150 mW is used as excitation light source. The monolayer is illuminated at an angle of 45° , polarized fluorescence microscopy can be performed in order to distinguish tilted and untilted phases. In the middle of the trough the objective faces the air/water interface from below. The choice of the sight direction has the advantage that objectives with a high numerical aperture can be used. Unfortunately then the objective is fixed and cannot be moved in order to investigate monolayer patterns. Using the optics of an inverted optical microscope (Zeiss, model: Axiovert 135) and a filter for the fluorescence light the monolayer is observed with a secondary ion tube (SIT) camera (Hamamatsu, model: C2400) directly connected to a commercial video tape recorder and TV-screen, on which the monolayer can be monitored instantaneously. The measured physical quantities pressure, temperature and area are plugged in with a Genlock adapter (VineGeN 2) from the computer screen and videotaped together with the monolayer images.

Additionally, an Y-YAG laser (from Jenoptik) is plugged in the optics of the microscope. This IR-laser has a power of up to 2 W and is focused on the air water interface. It can be used for local heating of the monolayer or - at lower power - in order to capture small silica beads within the focus and allow controlled mechanical manipulation of the monolayer patterns [12]. The laser then functions as optical tweezers [13]. Because the objective faces the surface from below the laser beam does not heat up the bottom and effects caused by heat convection are reasonably small. In order to compensate the fixed objective and allow some control of the observed region of the monolayer a device has been built confining a small region of the monolayer by a glass tube and move it using an XY-table (Lstep-12) (figure 2.3.1).

The XY-table can be controlled manually turning the positioning wheels or using a controlling

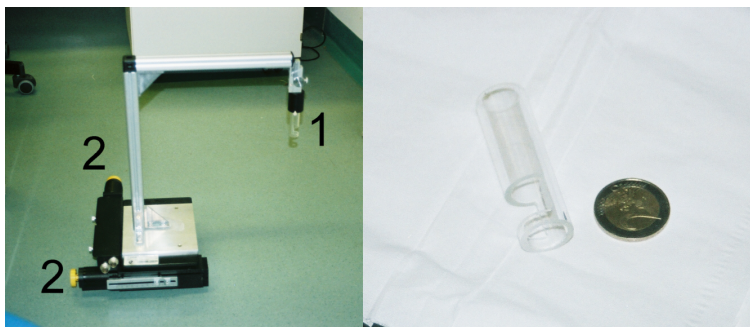


Figure 2.3.1: XY table. The monolayer is fixed by the glass tube (1, right figure). the glass tube can be moved by turning the wheels (2).

electronics assembly with a joystick. The glass tube has been silanized as described in [14]. One obtains a contact angle between water and the glass close to 90° . The air/water interface confined in the glass tube is flat in the focus of the microscope. The device allows a less efficient control compared to movable objectives facing from above. If the monolayer is quite dense and rigid a reasonable control is obtained. However, the nearby glass interface might have non-negligible effects on the pattern formation. This makes this device useful only for some special applications.

Chapter 3

Interactions in monolayers

This chapter deals with the interactions between monolayer surfactants considered in the common theories.

3.1 Long range electrostatic repulsion

Each molecule on the air water interface carries a dipole moment \mathbf{p} because of its polar head group and mirror charges within the water [15] and the CH_3 group also carrying a dipole moment. Unlike in the bulk phase the component perpendicular to the surface p_z is not screened by the polar water. This results in an electrostatic repulsion between any monolayer molecules 1 and 2 in distance \mathbf{r} with the interaction energy

$$F_{\text{dipole } 1,2} = \frac{1}{4\pi\epsilon} \frac{p_{z,1}p_{z,2}}{|\mathbf{r}|^3}, \quad (3.1.1)$$

where ϵ is the permittivity. The interaction leads to a repulsive force between distinct monolayer domains and between different parts of one domain (self interaction). It can be observed in experiments like the one shown in figure 3.1.1 b) [16], where small circular liquid expanded (LE) domains immersed in gaseous phase (G) form a depletion layer close to a liquid condensed (LC) wall because of dipolar repulsion.

If the monolayer phases are assumed to be phases in the sense of Gibbs, i.e. homogeneous with sharp interfaces, then to each phase i belongs a particular dipole density $\langle p_z \rangle_i / \alpha_i$ with the average dipole moment per molecule $\langle p_z \rangle_i$ and the average molecular area α_i . In order to calculate the total dipolar energy of the monolayer a simple lattice model can be taken into account [17]. In this model the molecules are assumed to be placed on the lattice sites of a regular quadratic lattice with the lattice constant $\Delta_{\text{latt.},i}$. Each molecule carries the average dipole moment of the corresponding phase. Then the total dipole energy of the monolayer is obtained by the summation over all possible pair interactions between all the molecules of the

monolayer N

$$F_{\text{lattice}} = \sum_{k=1}^N \sum_{l=k+1}^N F_{\text{dipole } k,l} \quad (3.1.2)$$

$$= \frac{1}{4\pi\epsilon} \sum_{k=1}^N \sum_{l=k+1}^N \frac{\langle p_z \rangle_i \langle p_z \rangle_j}{\mathbf{r}_{kl}^3}, \quad (3.1.3)$$

where the molecule k belongs to phase i and the molecule l belongs to phase j (If k and l belong to the same phase, i equals j). If the lattice constant $\Delta_{\text{latt.},i}$, or rather the molecular area $\alpha_i = \Delta_{\text{latt.},i}^2$ is small compared to the extension of the phases the sum can be approximated by a continuous distribution

$$F_{\text{dipole}} \approx \frac{1}{4\pi\epsilon} \sum_{i,j} \frac{1}{2} \frac{\langle p_z \rangle_i \langle p_z \rangle_j}{\alpha_i \alpha_j} \int_{A_i} \int_{A_j} \frac{dA dA'}{\sqrt{(\mathbf{r} - \mathbf{r}')^2 + \Delta_{\text{latt.},i}^2}^3}, \quad (3.1.4)$$

where the summation is done over all monolayer phases i and j and the integration is performed over the area of the individual phases. The lattice constant $\Delta_{\text{latt.},i}$ (in the range of some Å) becomes important if the interacting area elements come very close to each other. This is the case mostly in the 2D bulk ($i=j$) seldom on the interface between two different phases. Then $\Delta_{\text{latt.},i}$ prevents the integral (3.1.4) from diverging. Note that the $\Delta_{\text{latt.}}$ carries the length scale in the integral expression of the dipolar energy - with the physical meaning of the cut-off length of dipolar interaction. If one assumes that also van-der-Waals interactions act as a short range attraction between the molecules, the cut-off-length represents the length scale, where the van-der-Waals interactions overbalance the electrostatics (Δ_{vdW} in the range of some nm). In most systems the cut-off-length is not known. Since equilibrium shapes can be described using any sufficient¹ small Δ it is not easily accessible by measurements. This

¹to be defined in section 4.3

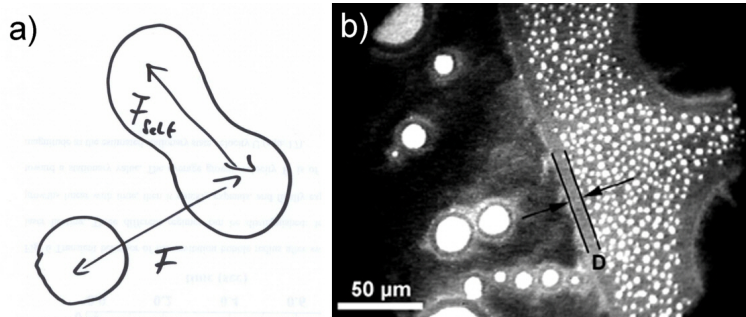


Figure 3.1.1: a) Sketch. The dipole moment of the surfactants leads to a repulsive force between monolayer domains and between different region of one domain b) Fluorescence image of methyl octadecanoate monolayer in the three phase coexistence region of bright LE, dark G and grey LC. Due to electrostatic repulsion the small LE domains form a depletion layer of thickness D close to the LC wall [16].

property will be derived in section 4.3 and can be formulated as a shape invariant scaling transformation, transforming the interaction parameters leaving shapes invariant. The Δ in equation (3.1.4) will be denoted as 'scaling parameter' in general, while 'cut-off-length' stands for the physical length on which short range interactions overbalance the dipole interaction. For ferrofluids, which share the same free energy as Langmuir monolayers, Δ is interpreted as the film thickness of the ferrofluid.

The common theory takes into account only one Δ for all the phases instead of one Δ_i for each. This amplification is justified due to the freedom of choice of the scaling parameter. However, in the limits of validity of the shape invariant scale transformation this simplification has to be discussed again.

The permittivity in (3.1.2) and (3.1.4) $\epsilon = \epsilon_0 \epsilon_r$ is expected to have a value between the permittivity of air ($\epsilon_r = \epsilon_{\text{air}} = 1$) and water ($\epsilon_r = \epsilon_{\text{water}} = 80$) [18, 19]. $\epsilon_0 = 8.854 \text{ pN/V}^2$ is the vacuum permittivity. A simple model for the monolayer is a series connection of two symmetrical capacitors one in air and one in water. The dipole density $\frac{p_{z,i}}{\Delta_{\text{latt}}^2}$ is proportional to the surface potential V_i :

$$C = \frac{1}{\frac{1}{C_{\text{air}}} + \frac{1}{C_{\text{water}}}} = \frac{A\epsilon_0}{d} \frac{2\epsilon_{\text{air}}\epsilon_{\text{water}}}{\epsilon_{\text{air}} + \epsilon_{\text{water}}} = \frac{q}{V} \quad (3.1.5)$$

$$\frac{p_{z,i}}{\Delta_{\text{latt}}^2} = 2\epsilon_0 \frac{\epsilon_{\text{air}}\epsilon_{\text{water}}}{\epsilon_{\text{air}} + \epsilon_{\text{water}}} V_i \approx 2\epsilon_0 V_i \quad (3.1.6)$$

Further, the notation with the dipole density parameter μ_i and μ_{ij} commonly used in the literature will be used

$$\mu_i^2 = \frac{\epsilon_0}{2\pi} V_i^2 \quad \text{and} \quad \mu_{ij} = \mu_i - \mu_j. \quad (3.1.7)$$

Experimental methods for the measurement of the dipole densities The classical method of surface potential measurement is with a Kelvin probe [20–22]. The probe is a mechanically oscillating capacitor with a periodic change of capacity, a detailed description is given by Adamson [23]. With a Kelvin probe one measures the surface potentials on the air-water interface on cm-scales, usually in the range of some 100 mV. The method is suitable especially in one phase regions of the monolayer. Generally the length scale of the structures in phase coexistence regions is much smaller than cm. Then the Kelvin probe measures the average surface potential \bar{V} . If the area fractions Φ_i of all phases i are known - i.e. extracted from monolayer pictures using an imaging technique - the surface potential contribution V_i of each phase can be calculated [16, 24–26]. For the calculation a lever rule is applied

$$\bar{V} = \sum_i \Phi_i V_i. \quad (3.1.8)$$

Measuring $\bar{\mu}$ at different Φ_i leads to a set of linear equations, which can be resolved for the unknown μ_i . The problem here is that the area fractions of the phases are most probably

different in the observed region (which is heated by the fluorescence light source or BAM-laser) compared to the unilluminated one within the Kelvin probe. The validity of the lever rule and the independence of the individual surface potentials from e.g. the area fraction, however, is plugged in a priori.

Other methods study the experimentally observed patterns. McConnell and Benvegnu [27,28] studied the behaviour of a small LE-droplet confined in a G-bubble surrounded by LC. The droplet performs Brownian motion, and out of its positional probability the interaction energy between the droplet (with kT energy on average) and the LC-wall can be evaluated. The disadvantage of this method is that domains performing Brownian motion are very small (some μm^2) and the measurement of the size is not very accurate. Within his diploma thesis the author of the present work together with Wurlitzer measured the equilibrium positions of domains in force equilibrium with the surroundings [16,26,29] and determined the ratio of the surface potentials of the LE- and LC-phase in the three phase coexistence region. Within the errors the results agree well with macroscopic measurements with a Kelvin probe. So the lever rule seems to be a good approximation at least. However, some experiments also point toward a decrease of the surface potential of smaller domains, leaving some doubt about the lever rule. Klopfer and Vanderlick [30] reported on evidences of violation of this rule as well. Nevertheless, the following theory will be developed assuming phases in the sense of Gibbs - i.e. sharp boundaries and constant properties in phase coexistence. Later in chapter 8 possible effects causing deviations will be discussed.

3.2 Line tension represents short range attraction

Similar to 3D systems the interface between the phases costs energy and it is possible to define the line tension - the 2D equivalent to the surface tension. Taking the direct analogue from 3D one defines the effective line tension as the partial derivative of the energy with respect to some deformation $\delta\mathbf{r}$ in an interface point \mathbf{r} :

$$\lambda_{\text{eff}}[\mathbf{r}(s), \delta\mathbf{r}(s)] = \left. \frac{\delta F}{\delta P} \right|_A \quad (3.2.1)$$

Because of the long range dipole interaction the effective line tension as defined in (3.2.1) is not a materials constant but depends on the shape $\mathbf{r}(s)$ and the mode of deformation $\delta\mathbf{r}(s)$. In figure 3.2.1 a) a line tension driven droplet fusion is shown which points toward a positive sign of the total energy per interface line. In figure 3.2.1 b) long range and short range interactions are in equilibrium and result in total effective line tension equal to zero. Here structures occur which do not minimize the length of the interface line.

So in literature [17] the *bare* line tension λ_{ij} between the phases i and j is introduced as the

line tension in the case of vanishing dipole interaction:

$$F_{\text{line}} = \frac{1}{2} \sum_{ij} \lambda_{ij} \int_{\text{facet } ij} ds \quad \text{for } \mu_i = 0, \quad (3.2.2)$$

where the summation is performed over all interface lines (=facets between domain i and domain j) and the line energy is directly proportional to the length of the interface. The bare line tension does not depend on the structure of the monolayer, it is a materials constant for each interface type.

Stable equilibrium structures can only be explained within a positive sign of the bare line tension. If the sign were negative the formation of new interface would always decrease the total energy and no stationary structure could occur. So the interactions represented by the line tension are attractive forces. The length scale of these forces is modelled by the cut-off-length Δ , which defines the dividing length between short range interaction (represented by the line tension) and long range interactions (represented by the dipole-dipole potential). Note that the line tension represents some average of all the interactions within the Δ -range, i.e. also short range contribution of the dipole interaction are included. Apparently, the value of the line tension depends on the dividing length scale Δ . I.e. stating a value for the line tension makes only sense with stating a scale parameter Δ simultaneously.

Experiments for measuring line tension Unlike the macroscopic surface potentials there exists no method measuring the bare line tension directly. It is a theoretical quantity describing - together with the scale parameter Δ - the strength of short range interactions. The first evaluation of the line tension known to the author was done by Muller et al. [31, 32], who studied the nucleation of needle shaped domains. Benvegnu and McConnell [33] applied shear to domains and evaluated the line tension from the deformation, and Mann et al. [34] studied the hydrodynamics of domain relaxation and determined the line tension. Another method

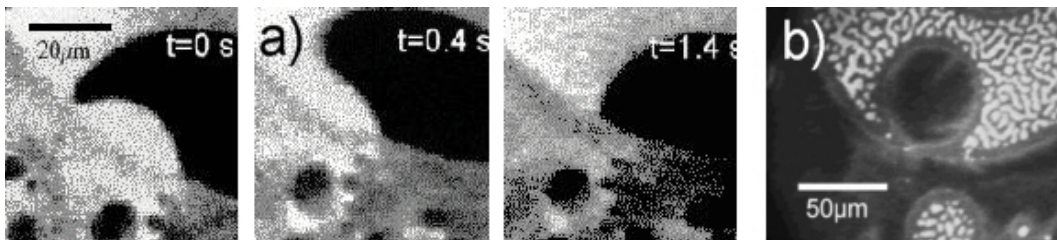


Figure 3.2.1: Fluorescence image in three phase coexistence of methyl octadecanoate monolayer phases (G: black, LE: bright, LC: gray). a) Domain fusion. The bigger LE-droplets on the left 'eats' the smaller droplet on the right. The total length of 2D interface line is reduced by this process, i.e. the total effective line tension has a positive sign. b) Elongated domains occur forming a labyrinthine pattern. The total effective line tension in equilibrium is zero.

applying mechanical forces has been published by Wurlitzer et al. [35, 36]. Wurlitzer used optical tweezers for a local deformation of the monolayer and studied the relaxation. In an other experiment a circular domain picked with the optical tweezers is moved and deformed by the shear flow. An approach without the need of external forces is studying equilibrium patterns for curvature and sizes. Rivière et al. [37] analyzed the curvature in two phase coexistence whereas Wurlitzer et al. [38] analyzed the equilibrium size of circular domains and evaluated the line tension. In literature it is common to calculate the line tension on \AA scale ($\Delta = \Delta_{\text{latt.}}$). On this scale the line tension for all measured systems is in the range 0.1–10 pN. Chapter 4 and 5 will present pendant droplet tensiometry and measurement of equilibrium size of 2D foams as a method for the determination of the bare line tension by analysis of equilibrium structures in more detail.

3.3 Free energy

The common model [39–44] takes the total free energy as the sum of the dipolar energy F_{el} , bare line energy F_{λ} the 2d-bulk energy F_0 :

$$F = F_{\text{el.}} + F_{\lambda} + F_0 \quad (3.3.1)$$

with the electrostatic energy

$$F_{\text{el.}} = \sum_{i,j} \frac{\mu_i \mu_j}{2} \int_{A_i} \int_{A_j} \frac{dA dA'}{\sqrt{(\mathbf{r} - \mathbf{r}')^2 + \Delta^2}^3}, \quad (3.3.2)$$

and the line energy (with the perimeter P_{ij} of the interface ij)

$$F_{\lambda} = \sum_{\{ij\}} \lambda_{ij} \int_0^{P_{ij}} ds_{ij} \quad \text{and} \quad F_0 = \sum_i F_0^i(A_i). \quad (3.3.3)$$

The bulk free energy F_0 is independent of the shapes of the domains and solely depends on the areas occupied by the individual phases. It also contains the entropy contributions, which are proportional to the area. Entropy arising due to the arrangements of the patterns is neglected. The shape dependent terms can be described using only the relative differences $\mu_{ij} = \mu_i - \mu_j$ of the surface potentials (dipole densities). This property is useful for calculations, since the surface potential of one phase (e.g. phase 1) can be set to zero.

Sometimes it might be useful to use line integral expressions instead of the area integrals in (3.3.2). It can be obtained by applying twice Greens' theorem on (3.3.2) (appendix A.3).

3.4 Mesoscopic pattern formation due to competition between long- and short-range interaction

The bigger the line tension the more costly the interface line and consequently the larger the structures. The bigger the surface potentials the bigger the self repulsion within a domain and the smaller the structures. The short range and long range interaction are competing interactions and the structures formed should have a well defined length scale. In 1988 McConnell and Moy [17] calculated the equilibrium radius of an isolated domain. The free energy (3.3.1) can be calculated for a free circular disc with radius R and is given by ²

$$F = \pi \mu_{12}^2 R^2 \left(\frac{\pi}{\Delta} - \frac{2}{R} \ln \frac{8R}{e\Delta} \right) + 2\pi \lambda_{12} R + F_0, \quad (3.4.1)$$

where the phases of the domain and surroundings are denoted with 1 and 2. Minimizing the free energy of N such discs with respect to R while keeping a fixed amount of phase (NR^2) yields the equilibrium area A_0

$$\sqrt{A_0} = \Delta \frac{\sqrt{\pi} e^2}{8} e^{\lambda_{12}/\mu_{12}^2}. \quad (3.4.2)$$

Increasing the size of the domain beyond its equilibrium size leads to shape instabilities at a critical size [17, 27, 40, 41, 45–47] of

$$\sqrt{A_2} = \Delta \frac{\sqrt{\pi} e^2}{8} e^{\lambda_{12}/\mu_{12}^2} e^{7/3}, \quad (3.4.3)$$

which describes the instability size with respect to a two-fold deformation. A general equation of the critical size with respect to n -fold deformation is given in [47, 48]:

$$A_n = A_0 e^{2Z_n}, \quad (3.4.4)$$

with

$$Z_n = 1 + \frac{n^2}{3} \sum_{k=0}^{n-2} \frac{1}{k!} \prod_{j=0}^{k-1} \frac{(1+j)^2(2-n+j)(2+n+j)}{(3/2+j)(5/2+j)(3+j)}. \quad (3.4.5)$$

Experiments on shape instabilities have been presented by deKoker and McConnell [40] and Lee and McConnell [41]. Fluorescence images from the latter are shown in figure 3.4.1.

A free circular domain prefers a certain size in equilibrium and becomes unstable when exceeding a critical size. This behaviour is different from 3D macroscopic systems. In 3D systems the larger structure has always less energy per unit material than the smaller one since it has less interface compared to the bulk. This is the reason why in 3D no specific length scale exists.

Since in monolayers mesoscopic patterns are formed the question arises which morphology minimizes the free energy (3.3.1) for given thermodynamic state variables, e.g. pressure π and

²in [17] is a mistake, here the corrected equation

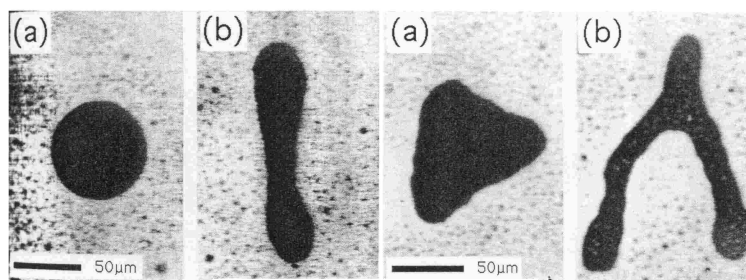


Figure 3.4.1: Taken from [41]. Fluorescence images of a L- α -dimyristoylphosphatidylcholine/dihydrocholesterol binary mixture. Circular domains perform two- and three-fold shape transitions.

area fraction of the phases Φ_i . For simplification two phases forming periodic structures were assumed, and the investigation was focused on the connectivity of the phases [44, 49, 50]. In principle three different morphologies occur. They are presented in figure 3.4.2. Kwok-On and Vanderbilt [49, 50] found the emulsion morphology minimizing the total free energy of the monolayer up to an area fraction of domain forming phase $\Phi \approx 0.28$. Between 0.28 and 0.72 area fraction stripe phases minimize the total free energy. In fact there is some contradiction to the experiments, where stripe phases are relatively rarely observed. Experiments reported by Stine and Kretzer [51] showed a transition from a stripe phase (connectivity 0) to a 2D foam - according to Kwok-On and Vanderbilt less stable than the inverted emulsion. A later stability analysis of Kwok-On and Vanderbilt [50], however, supported their theory. Recently McConnell and de Koker showed that the monolayer might be trapped within one of infinity local energy minima [46]. The structures observed in monolayer are most probably metastable, but in local thermodynamic equilibrium.



Figure 3.4.2: Connectivities of periodic structures. a) Emulsion. Droplets of phase 1 are immersed in phase 2. The connectivity is 1. b) Stripe structure. The two phases form a stripe- or labyrinthine-pattern. The connectivity is 0. c) Inverted emulsion. The connectivity is -1 .

Chapter 4

Interfaces

Two different phases meet at an interface. The present chapter deals with the thermodynamical equilibrium conditions for interfaces between 2D phases. In the sense of Gibbs an ideal interface is infinitely narrow, i.e. the properties of the bulk phases close to the interface are not affected. In the following such Gibb's interfaces are assumed.

4.1 Young-Laplace-equation in 3D

Sessile or pendant droplets in a gravitational field are characteristically deformed. Minimization of the free energy of a droplet with respect to shape under constraint of constant droplet volume yields the Euler-Lagrange equation: a condition for the shape [2, 52, 53], well known as Young-Laplace equation containing the pressure difference between inside and outside as a Lagrange parameter

$$\sigma\kappa = p_i - p_a. \quad (4.1.1)$$

The curvature $\kappa = \frac{1}{R_1} + \frac{1}{R_2}$ is directly proportional to the pressure difference across the interface with the surface tension σ as coefficient.

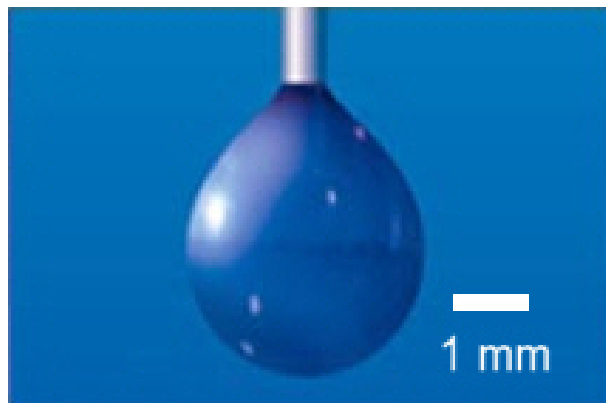


Figure 4.1.1: Pendant water droplet in gravity field.

In a gravitational field the pressure difference is the sum of the Laplace-pressure - a constant within the whole droplet - and gravity pressure, which is a function of the height. Droplet shapes can be evaluated by solving the Young-Laplace equation (a differential equation) for a boundary condition on the droplet neck (figure 4.1.1).

The determination of surface tension by the evaluation of pendant or sessile droplet shapes is a common technique (pendant droplet tensiometry).

4.2 2D Young-Laplace-equation including long range interaction

Assume a monolayer structure consisting of N domains. The interfaces (facets) between the domain i and j ($i, j = 1 \dots N$) are described by \mathbf{r}_{ij} . Minimizing the total free energy (3.3.1) while varying the shapes under constraint of constant domain area directly yields the local stability criteria for the shape. A detailed derivation is done in the appendix (A.2).

One finds that the curvature $\kappa_{ij}(\mathbf{r})$ in \mathbf{r} is proportional to the pressure difference across the phase boundary with the bare line tension λ_{ij} as coefficient [37, 54]:

$$\lambda_{ij}\kappa_{ij}(\mathbf{r}) = p_{ij} + p_{\text{el}}(\mathbf{r}) \quad (4.2.1)$$

This equation is similar to the Young-Laplace equation describing the shape of 3D droplets in

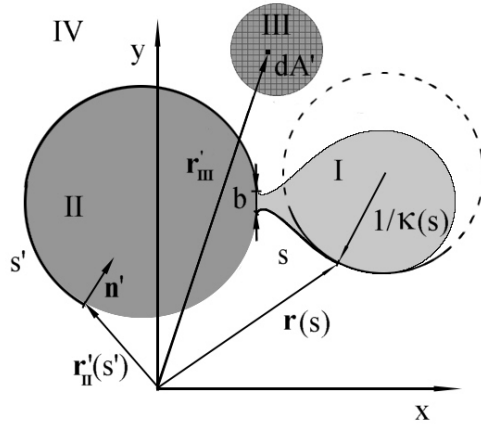


Figure 4.2.1: Sketch of a monolayer pattern. The domains I-IV are separated by the facets IV/I, IV/II, IV/III respectively I/II. Facets are either closed loops (IV/III) or start and end in intersection points. The curvature $\kappa(s)$ is affected by the electrostatic pressure (4.2.2) from surrounding domains. The total dipole pressure is obtained by integration of infinitesimal dipole contributions over the domain area (example domain III) (4.2.2) or along the facets after twice application of Greens theorem (example domain II) (using (A.3.3)).

the gravitation field with the Laplace-pressure p_{ij} and the dipole pressure p_{el} instead of the gravity pressure:

$$p_{el}(\mathbf{r}) = - \sum_k \mu_{ij} \mu_k \int_{A_k} \frac{dA'}{\sqrt{(\mathbf{r} - \mathbf{r}')^2 + \Delta^2}^3} \quad (4.2.2)$$

Unlike in 3D the electrostatic pressure depends on the structure of the whole monolayer and the shape of the droplet itself. Because of the electrostatic pressure LE-droplets attached on LC-walls in gaseous surroundings are deformed to a typical pendant droplet shape (sketch in figure 4.2.1).

4.3 Shape invariant scaling

One finds that the Young-Laplace-equation is invariant to the scale transformation [37, 40, 54]:

$$(\Delta_1, \lambda_{ij,1}, p_1, \mu_{i,1}) \rightarrow (\Delta_2, \lambda_{ij,2}, p_2, \mu_{i,2}), \quad (4.3.1)$$

where

$$\lambda_{ij,2} = \lambda_{ij,1} - \mu_{ij,1}^2 \ln \frac{\Delta_2}{\Delta_1},$$

$$p_2 = p_1 - (\mu_{i,1}^2 - \mu_{j,1}^2) \left(\frac{\pi}{\Delta_2} - \frac{\pi}{\Delta_1} \right), \text{ and}$$

$$\mu_{i,2} = \mu_{i,1},$$

provided Δ_1 and Δ_2 are smaller than then the curvature radius $R = 1/\kappa_{ij}$:

$$\Delta \kappa_{ij} \ll 1 \quad (4.3.2)$$

The detailed derivation is done in the appendix A.4. So any pairs (Δ_1, λ_1) and (Δ_2, λ_2) describe a shape equally well if they are connected by the shape invariant scale transformation (4.3.1). The scaling parameter Δ and bare line tension λ_{ij} can be expressed by one parameter, the renormalized line tension

$$\lambda_{ij}^* = \lambda_{ij} + \mu_{ij}^2 \ln \frac{\Delta}{l}, \quad (4.3.3)$$

where l is an arbitrary length unit and often set to the square root of the droplet area \sqrt{A} . Note that the scaling law is valid only if Δ is smaller than the curvature radius, i.e. if the shape is sufficiently smooth on Δ -scale. At three phase intersection points a singularity in the curvature occurs and the scaling law is not applicable in these points. In two phase coexistence the scaling law holds if Δ is sufficient small.

4.4 Pendant droplet tensiometry in monolayers

The idea is to apply the Young-Laplace-equation (4.2.1) to experimentally observed structures and to determine interaction parameters. The electrostatic pressure (4.2.2) can be calculated numerically by integration over the images.

4.4.1 Experimental

Methyl octadecanoate (MOD) from Sigma-Aldrich and 1 mol % of the fluorescence dye nitrobenzoxadiazol-hexadecylamin (NBD-HDA) from Molecular Probes were spread on pure millipore water (Milli Q) from chloroform solution. The spreading was performed at a temperature of $T = 27.5^\circ\text{C}$ to an area of $\alpha \approx 40\text{\AA}^2/\text{molecule}$.

Under these conditions the three phases G, LE and LC coexist and wetting LE droplets on LC interfaces in gaseous environment are observed. After expansion to $\alpha \approx 100\text{\AA}^2$ and recompression 2D pendant LE-droplets on LC-border lines occur. Two fluorescence microscopy images of such droplets are shown in figure 4.4.1. Figure 4.4.1 a) shows a droplet at an area per molecule of $\alpha = 30\text{\AA}^2$. The droplet curvature changes as one moves along its LE/G boundary. Close to the points where the droplet is attached to the LC-phase the curvature is negative with a concave droplet shape. About $20\text{ }\mu\text{m}$ from the LC phase the curvature changes sign and the droplet is convex with a radius of curvature of roughly $20\text{ }\mu\text{m}$. The droplet partially wets an extended LC-region. The characteristic shape of the droplet is a result of the interplay of the line tension, electrostatic self interaction, and the electrostatic repulsion from the LC-phase to which the droplet is attached. Figure 4.4.1 b) is taken at an area per molecule of $\alpha = 25\text{\AA}^2$, where the droplets are confined to circular gas cavities. Its shape is closer to a circle than that of figure 4.4.1 a). The change in sign of the droplet curvature occurs much closer ($\approx 5\text{ }\mu\text{m}$) to the LC-boundary than that of the less confined droplet.

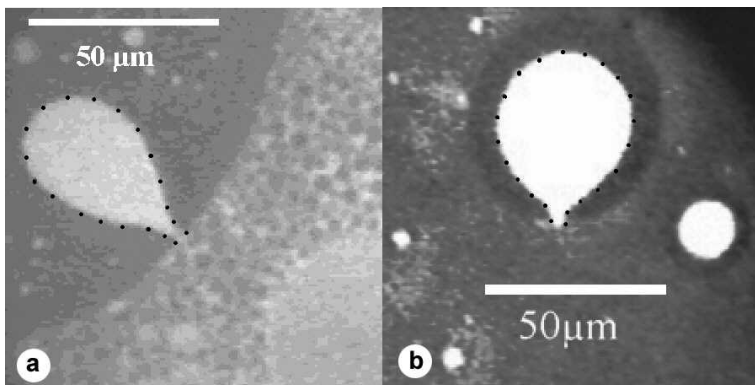


Figure 4.4.1: Pendant droplets in the three phase coexistence region LE (bright), LC (gray) and gas (dark) of a methyl octadecanoate monolayer. The interaction parameters $\tilde{\mu}$ and $\tilde{\lambda}_{\text{LE/G}}$ are calculated from the geometry of the images using the Young Laplace equation. a) pendant droplet at $\alpha = 30\text{\AA}^2$ attached to a straight LC-wall b) pendant droplet of a denser monolayer ($\alpha = 25\text{\AA}^2$) formed in a circular gas-bubble

4.4.2 Numerical image analysis

For any point on the droplet LE/G interface the Young-Laplace-equation (4.2.1) has to be fulfilled

$$\lambda_{\text{LE/G}}\kappa(\mathbf{r}) = p - \sum_k \mu_{\text{LE/G}}\mu_k \int_{A_k} \frac{dA'}{\sqrt{(\mathbf{r} - \mathbf{r}')^2 + \Delta^2}^3}, \quad (4.4.1)$$

where the surface potential of the gaseous phase is taken as the reference potential (A.1.7). For numerical calculation of the integrals in (4.4.1) it is useful to take the line integral expression instead of the surface integral expression. The line integral expression is obtained by application of Green's theorem (A.3.2) given in the appendix A.3. The pressure integrals in eq. (4.4.1) can be separated into interactions of the droplet with the LE-regions:

$$I_{\text{LE}} = - \int_{\partial A_{\text{LE}}} d s' \frac{\mathbf{n}' \cdot (\mathbf{r} - \mathbf{r}')}{\Delta(\rho + \Delta)\rho} \quad (4.4.2)$$

with

$$\rho = \sqrt{(\mathbf{r} - \mathbf{r}')^2 + \Delta^2} \quad (4.4.3)$$

and into interactions of the droplet with the LC-regions:

$$I_{\text{LC}} = - \int_{\partial A_{\text{LC}}} d s' \frac{\mathbf{n}' \cdot (\mathbf{r} - \mathbf{r}')}{\Delta(\rho + \Delta)\rho}, \quad (4.4.4)$$

where the integration is performed over all LE (LC) boundaries in the monolayer. All tangent vectors \mathbf{t}' are chosen in such a way that the LE (LC) phase is to the left and \mathbf{n}' is pointing into the LE (LC) phase. The integrals (4.4.2) and (4.4.4) are determined by the structure and can be calculated by numerical integration over the experimental images. This has been done by approximating the boundaries by cubic splines traveling through sampling points set at a separation of approximately $5 \mu\text{m}$. The scale parameter has been set to $\Delta = 10 \text{ pixels} \approx 4 \mu\text{m}$ (making use of shape invariant scaling). This chosen scale contains all the information, is much smaller than the minimum curvature and much larger than step width of the integration ($0.4 \mu\text{m}$).

For each sample point $\mathbf{r}(s_i), i = 1, 2, 3 \dots N$ at the LE/G droplet boundary the Young-Laplace-equation (4.4.1) can be formulated, which yields an overdetermined linear system of equations

$$\tilde{\mu}I_{\text{LE}}(s_i) + I_{\text{LC}}(s_i) + \tilde{\lambda}_{\text{LE/G}}\kappa(s_i) = \tilde{p}. \quad (4.4.5)$$

In equation Eq. (4.4.5) the integrals I_{LE} and I_{LC} and the curvature κ are geometrical quantities determined from the fluorescence images while the dimensionless pressure

$$\tilde{p} = \frac{p}{\mu_{\text{LE/G}}\mu_{\text{LC/G}}}, \quad (4.4.6)$$

the dimensionless line tension

$$\tilde{\lambda}_{\text{LE/G}} = \frac{\lambda_{\text{LE/G}}}{\mu_{\text{LE/G}}\mu_{\text{LC/G}}} \quad (4.4.7)$$

and the ratio between the relative surface potentials

$$\tilde{\mu} = \frac{\mu_{\text{LE/G}}}{\mu_{\text{LC/G}}}, \quad (4.4.8)$$

are the unknown material parameters in units $\mu_{\text{LE/G}}\mu_{\text{LC/G}}$.

One can eliminate \tilde{p} in eq. (4.4.5) by introducing the fluctuations

$$\delta f(s_i) = f(s_i) - \frac{1}{N} \sum_j f(s_j) \quad (4.4.9)$$

to find:

$$\tilde{\mu}\delta I_{\text{LE}}(s_i) + \tilde{\lambda}_{\text{LE/G}}\delta\kappa(s_i) = -\delta I_{\text{LC}}(s_i). \quad (4.4.10)$$

The two parameters $\tilde{\lambda}_{\text{LE/G}}$ and $\tilde{\mu}$ are determined by applying a least square procedure to equation (4.4.10).

In figure 4.4.2 the integrals $\delta I_{\text{LE}}(s)$, $\delta I_{\text{LC}}(s)$, $\delta\kappa(s)$ as well as $\tilde{\mu}\delta I_{\text{LE}}(s) + \delta I_{\text{LC}}(s) + \tilde{\lambda}_{\text{LE/G}}\delta\kappa(s)$ are plotted as a function of the position s along the LE/G boundary for the droplet in figure 4.4.1 a).

As one can see the least square deviations are approximately 10% of the values of the integrals and errors are in the same order of magnitude. The least square procedure is more accurate for the determination of $\tilde{\lambda}$ than for $\tilde{\mu}$. We applied it to 14 different LE-droplets and found $\tilde{\mu} = 0.26 \pm 0.12$ and $\tilde{\lambda}_{\text{LE/G}}^{4\mu\text{m}} = 3.3 \pm 0.2$.

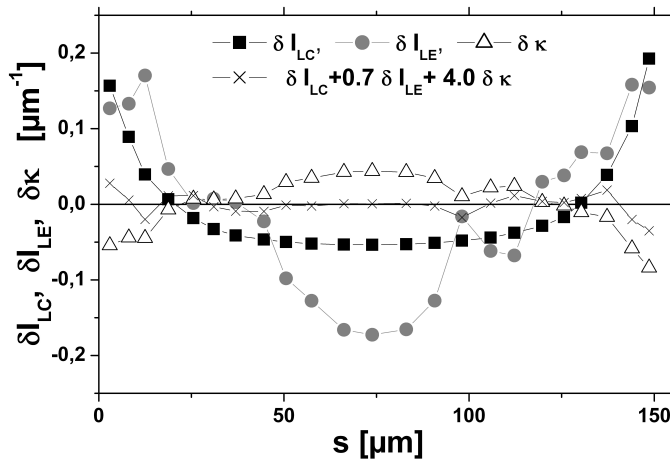


Figure 4.4.2: Plot of the integrals $\delta I_{\text{LC}}(s)$, $\delta I_{\text{LE}}(s)$, $\delta\kappa(s)$ and $\delta I_{\text{LC}}(s) + \tilde{\mu}\delta I_{\text{LE}}(s) + \tilde{\lambda}\delta\kappa(s)$, ($\tilde{\mu} = 0.7$, $\tilde{\lambda} = 4$) along the boundary of the droplet presented in 4.4.1 a). The deviation of the latter sum from zero is about 10% of the size of the first three graphs and the error in $\tilde{\lambda}$ for this individual droplet is also around 10%.

In order to be able to compare the line tension with values in literature usually given on \AA -scale the shape invariant scale transformation is applied. It yields with $\Delta = 5 \text{\AA}$ [46] and $V_{\text{LC}} - V_{\text{G}} = 0.41 \pm 0.01 \text{ V}$, $V_{\text{LE}} - V_{\text{G}} = 0.15 \pm 0.03 \text{ V}$ [16] the line tension $\lambda_{\text{LE/G}}^{5\text{\AA}} = (0.6 \pm 0.2) \text{ pN}$. Wurlitzer [26] measured in methyl octadecanoate monolayer the relaxation of G stripes in LE $\lambda_{\text{LE/G}}^{5\text{\AA}} = (0.4 \pm 0.2) \text{ pN}$ and of LE stripes in G $\lambda_{\text{LE/G}}^{5\text{\AA}} = (2.2 \pm 0.7) \text{ pN}$.

4.5 Discussion

The concept of interfacial tension and long range interaction, together with a scaling law for the dividing length scale, is suitable in order to describe shapes in a 2D dipolar systems. In Appendix A.2.1 the derivation of the Young-Laplace equation is extended to any pair interaction and external potential. The model demands only sharp interfaces and constant material parameters within each phase. A number of interactions could be described by the line tension/long range potential-concept. Dietrich [55, 56] found a dependence of the surface tension of water probed by X-ray reflection on the wave vector of the X-ray beam. The wave length of the X-ray beam can be interpreted as the length scale of the surface tension measurements. The results point out a decrease in surface tension at smaller scales, consistent with a scaling theory with attractive long range forces. So the concept looks very promising for systems with long range van-der-Waals forces or other long range interaction systems. However, the usual concept of describing long range van-der-Waals interaction in 3D is taking into account only the interaction of the substrate as a function of the distance (surface function $P(z)$). The interaction is described by a Hamaker constant and the self interaction is neglected.

In 1997 it was reported by Yeung et al. [57] that dissipative processes lead to violation of the Young-Laplace-equation in non-equilibrium. Rey derived the Young-Laplace equation for anisotropic liquid crystals [58], and Minkov and Novick-Cohen [59] reported on droplet shapes under the influence of van-der-Waals forces. The latter stated a Young-Laplace-equation with pressure arising from interaction with the substrate taking no account of self interaction.

Chapter 5

2D dipolar foams

Foams are structures with a high surface to volume ratio. They are formed by a collection of bubbles surrounded by a continuous phase. One distinguishes between wet and dry foams. Wet foams, including emulsions, are solutions of spherical bubbles where the bubble interfaces are stabilized by soluble surfactants. Dry foams are formed by reducing the volume fraction of the liquid towards the critical packing density of the bubbles. They consist of facets of minimal surfaces bounded by Plateau borders [60]. Most of the liquid remains in the Plateau borders, where generically three different thin films meet. The cross over from the wet foam to a dry foam occurs in conjunction with the change in shape of the foam during formation of facets and Plateau borders. It is governed by short range interactions within the thin films. On a macroscopic scale the shape consists of spherical segment films, and also the Plateau border surfaces are constant curvature surfaces. A non constant curvature of the surfaces becomes apparent only on the length scale of the short range interactions. Foams are metastable structures with a finite relaxation time.

In the present paragraph we investigate 2D foams in Langmuir monolayers of fatty acids. In contrast to the 3D foams (or non-dipolar 2D foams [61–64]) no interface active substances (in 3D: surfactants) are necessary in order to stabilize the foam. The presence of long range dipole repulsion leads to the formation of discontinuous phases ([39, 50] and section 3.4) and stabilizes the interface of the 2D-structures. Unlike short range interaction foams the foam does not coarsen persistently but reaches a local equilibrium at a well defined bubble size. We observe wet foams at low area fraction of gaseous phase immersed in a liquid expanded phase (LE) as shown in figure 5.0.1 a) and dry them by expansion (fig. 5.0.1 b) and c)). According to the calculations of Kwok-On and Vanderbilt [50] the morphologies in figure 5.0.1 b) and c) are metastable. However, Berge et al. [65] reported on experimentally observed foam stability over several days.

The equilibrium size of a bubble increases on drying. Theoretical studies on the bubble size by Wurlitzer et al. [38] showed good agreement with the experiments. The foam was approximated

by circular bubbles and the interaction model presented here was used. The bubble size has been found to be determined by the ratio of the line tension and dipole density to the square. Here we extend these studies focusing on the deformation of the bubble shapes.

5.1 Bubble shapes of ideal 2D foams are universal

Let us assume an ideal periodic hexagonal foam or emulsion (Fig. 5.1.1). The structure is determined by the gas fraction of the phases $\Phi = A/a^2 \sin \frac{\pi}{3}$ (a the lattice constant) and the shape of one bubble \mathbf{r} . The shape depends on Φ , the area of one bubble A and the materials constants dipole density parameter $\mu = \mu_{12}$, line tension $\lambda = \lambda_{12}$ and the scale parameter Δ . Making use of the shape invariant scaling law (4.3.1), the materials parameters can be expressed by the renormalized dimensionless line tension

$$\tilde{\lambda}^* = \frac{\lambda}{\mu^2} + \ln \frac{\Delta}{\sqrt{A}} \quad (5.1.1)$$

and one can write for the shape

$$\mathbf{r} = \sqrt{A} \tilde{\mathbf{r}}(\Phi, \tilde{\lambda}^*), \quad (5.1.2)$$

where the dimensionless $\tilde{\mathbf{r}}$ stands for a shape of unit area.

At thermodynamic equilibrium the free energy (3.3.1) is a minimum with respect to the size of a domain [38, 66]:

$$\left. \frac{\partial F}{\partial A} \right|_{\Phi, \Delta, \lambda, \mu^2} = 0 \quad (5.1.3)$$

De Koker and McConnell [40] could show that the renormalized dimensionless free energy \tilde{F}^* (defined in appendix A.5 equations (A.5.1, A.5.2)) is invariant to shape invariant scale transformation. So the minimization (5.1.3) can be replaced by a minimization of \tilde{F}^* with respect to the interaction parameter $\tilde{\lambda}^*$:

$$\frac{\partial}{\partial \tilde{\lambda}^*} e^{\tilde{\lambda}^*} \tilde{F}^*(\tilde{\lambda}^*, \Phi) = 0 \quad (5.1.4)$$

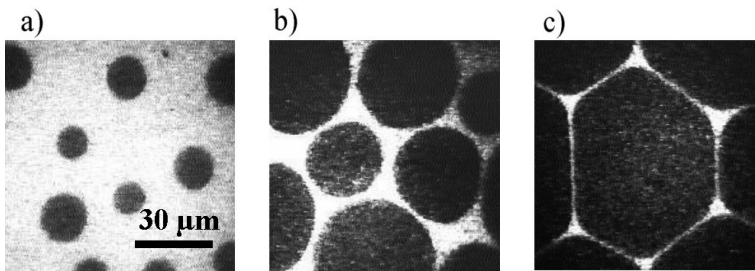


Figure 5.0.1: Fluorescence microscopy images of a myristic acid monolayer at a) $41 \text{ \AA}^2/\text{molec}$, b) $46 \text{ \AA}^2/\text{molec}$ and c) $51 \text{ \AA}^2/\text{molec}$ showing the cross over from a wet foam toward a dry foam.

and determines $\tilde{\lambda}^*$ in equilibrium as a function of Φ .

Inserting $\tilde{\lambda}^*(\Phi)$ into equation (5.1.2) yields the unit equilibrium shape

$$\tilde{\mathbf{r}}_{\text{eq}} = \tilde{\mathbf{r}}_{\text{eq}}(\Phi). \quad (5.1.5)$$

So the shape $\tilde{\mathbf{r}}_{\text{eq}}$ of the bubbles in a periodic dipolar foam is universal and depends only on the area fraction Φ and not on the material constants (λ , Δ , or μ).

For the size one finds (appendix A.5)

$$\sqrt{A} = \sqrt{A_0} e^{Y(\Phi)} \quad (5.1.6)$$

where $Y(\Phi)$ is a universal size function and A_0 the equilibrium size of an isolated domain (3.4.2) [66]

$$\sqrt{A_0} = \Delta \frac{\sqrt{\pi} e^2}{8} e^{\lambda/\mu^2} \quad \left(\equiv \tilde{\lambda}_0^* = \ln \frac{8}{\sqrt{\pi} e^2} \right). \quad (5.1.7)$$

The size A_0 depends on the materials parameters. At vanishing dipole interaction, $\mu = 0$, it diverges.

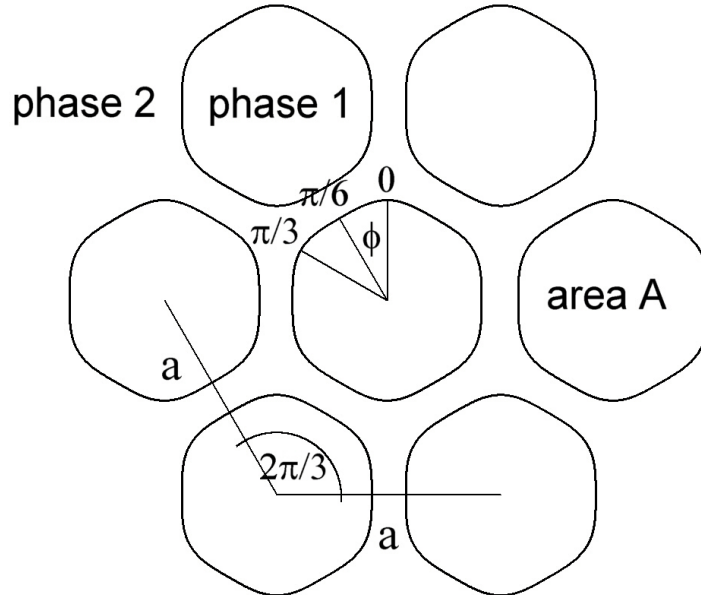


Figure 5.1.1: Sketch of an ideal periodic foam. All bubbles (phase 1) have the same shape and area A and form a hexagonal lattice with the lattice constant a . The bubble shape is assumed to have a C_{6v} point group symmetry and is entirely described by its behaviour in a polar angle range of $0 < \phi < \pi/6$.

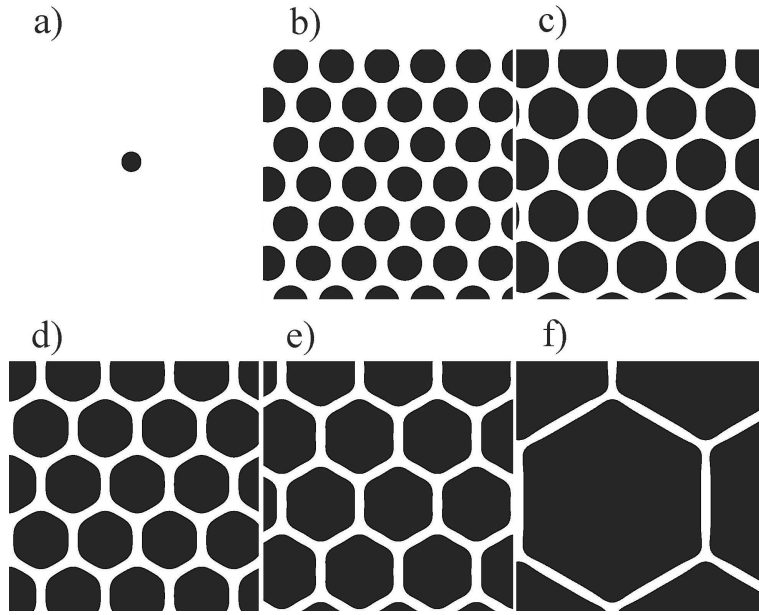


Figure 5.2.1: Simulated foams for area fractions a) $\Phi = 0$, b) $\Phi = 0.5$, c) $\Phi = 0.683$, d) $\Phi = 0.74$ and e) $\Phi = 0.9$. Upon increasing Φ , the bubble size increases. The foam structure changes from an emulsion of circular bubbles a), b) via c), d), e) to a dry foam with almost hexagonal shape f).

5.2 Numerical calculation of bubble shapes

The aim is to numerically find the equilibrium foam structure (bubble size and shape) for a given area fraction Φ of the two phases. We approximated the foam by one central bubble and 1260 surrounding bubbles in hexagonal order with the lattice constant a (Fig 5.1.1). The Young-Laplace-equation is solved assuming all bubbles of the foam have the same shape. The shape for a given Φ and $\tilde{\lambda}^*$ has been calculated using the procedure described in appendix A.6. The free energy is minimized using the renormalized dimensionless free energy \tilde{F}^* (A.5.4) and solving the minimum condition (5.1.4) as described in the appendices A.5 and A.6.

In figure 5.2.1 simulated foams and emulsions are shown. In a) at $\Phi \approx 0$ there is an isolated domain. Its size A_0 is given by equation (3.4.2) found by McConnell [66]. In b) the amount of the black phase is 50% and the domains are almost circular. Further increasing of the area fraction to c) (65%) leads to an increase of equilibrium size and a deformation of the bubbles. In d) (68.3%) and e) (74%) foams are formed and at high Φ f) (90%) dry foams occur with almost perfect hexagonal bubble shape.

bubble size

In figure 5.2.2 the relative size $\sqrt{A/A_0}$ is plotted as a function of the area fraction Φ (black dots). At lower surface fractions $\Phi \lesssim 0.85$ the relative bubble size is well described by a model

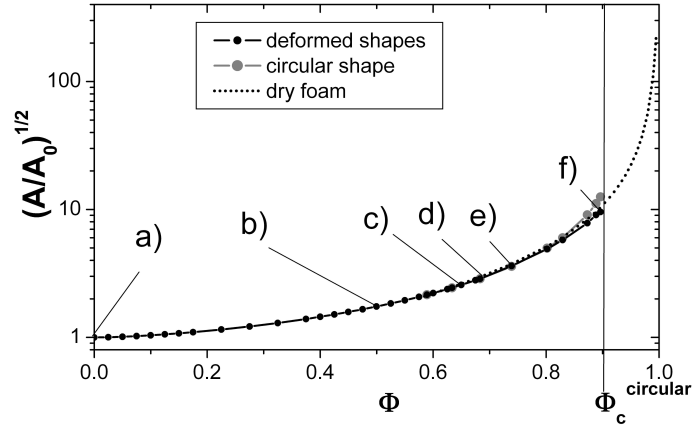


Figure 5.2.2: Relative bubble areas $\sqrt{A/A_0} = e^{Y(\Phi)}$ versus the area fraction Φ at thermodynamic (metastable) equilibrium of deformed bubbles (black dots), circular bubbles [38] (grey dots) and a dry hexagonal foam of non interacting facets (grey line).

considering circular domains [38] (grey dots) while at higher surface fractions $\Phi \gtrsim 0.85$ the approximation of the foam by noninteracting liquid facets (grey line) fits quite well

$$\frac{A_{\text{dry foam}}}{A_0} = \frac{8}{e^2} \sqrt{\frac{2\sqrt{3}}{\pi}} \sqrt{\frac{\Phi}{1-\Phi}}. \quad (5.2.1)$$

The bubble size of a dry foam diverges at $\Phi = 1$.

bubble shape

Figure 5.2.3 shows the results of the shape analysis. The numerical equilibrium shapes are expressed as a function of their arc length s . A change of the coordinate system from the arc length toward a polar coordinate system is performed, $\tilde{r}(s) \rightarrow \tilde{r}(\phi)$. Due to symmetry reasons the Fourier expansion of the unit bubble shape reads :

$$\tilde{r}(\phi) = \frac{c_0}{2} + \sum_{n=1}^{\infty} c_{6n} \cos(6n\phi) \quad (5.2.2)$$

The origin is set to the center of the bubble and $\mathbf{r}(\phi = 0)$ is pointing to an edge. We express the Fourier coefficients c_{6n} as

$$c_{6n} = c_{6n}^{\text{hex}} f_{6n}(\Phi), \quad (5.2.3)$$

with c_{6n}^{hex} the Fourier coefficients of the unit hexagon ¹ and the $f_{6n}(\Phi)$ area fraction dependent coefficients describing the deviation of the shape from a hexagon. The coefficient f_0 is

¹The Fourier coefficients of the unit hexagon are $c_{6n}^{\text{hex}} = 2^{-1/2} 3^{3/4} \pi^{-1} [\ln 3 + \Psi(n + \frac{1}{2}) - \Psi(3n + \frac{1}{2})]$, where $\Psi(z) = d/dz \ln(\Gamma(z))$ is the digamma-function. The values of the first coefficients are $c_0^{\text{hex}} = 0.564$, $c_6^{\text{hex}} = 1.64 \cdot 10^{-2}$, $c_{12}^{\text{hex}} = 4.54 \cdot 10^{-3}$, ...

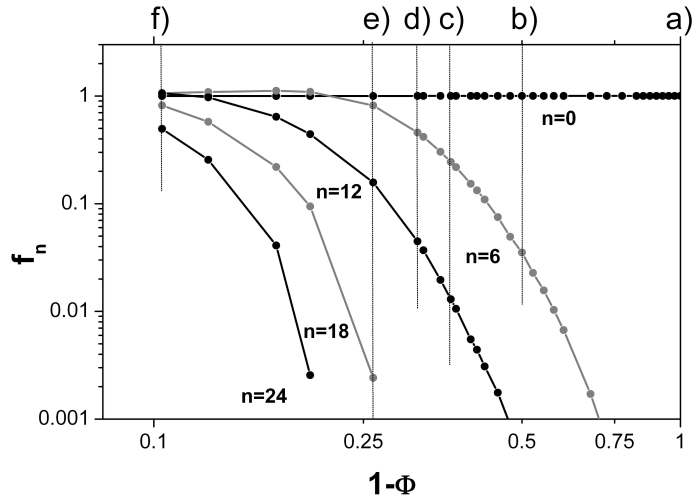


Figure 5.2.3: Bubble shape parameters f_{6n} versus area fraction. The shape parameters f_{6n} (5.2.3) switch from 0 to 1 as the shape changes from circular toward hexagonal upon increasing the area fraction Φ .

approximately 1 for all values of Φ . For $n > 0$ $f_{6n} = 0$ corresponds to a circle and $f_{6n} = 1$ to a hexagon. In figure 5.2.3 we plot the values of f_{6n} versus the area fraction. The cross over from circular shapes to hexagonal shapes happens between 65% and 80% area fraction, where $0.3 < f_6 \leq 1$.

5.3 Experimental foams dry at predicted area fraction

Myristic acid and pentadecanoic acid from Sigma were spread at room temperature ($\approx 20^\circ\text{C}$) from a chloroform solution on pure water subphase (Milli Q). 1 % mol fluorescence dye (NBD-HDA, Molecular Probes) was added to the chloroform solution. The monolayer was spread to an area of $\alpha \approx 35\text{\AA}^2$ per molecule, where no gaseous phase occurs. Slow isothermal expansion leads to the formation of small gas bubbles at $\alpha \approx 40\text{\AA}^2$ per molecule (figure 5.0.1 a)), deformed bubbles at $\alpha \approx 45\text{\AA}^2$ per molecule (figure 5.0.1 b)) and dry foams at areas larger than $A_{\text{mol}} \approx 50\text{\AA}^2$ per molecule. The images were recorded and digitized for further evaluation. The observed foams are non-ideal with polydisperse bubbles in unregular order (Fig. 5.0.1 a)-c)). Deformations are in general not 6-fold symmetric, and a direct comparison of the shape coefficients f_{6n} (5.2.3) is not possible. We decided to take the mean square deviation from a circle

$$\sigma^2 = \frac{\langle(|\mathbf{r} - \mathbf{r}_c|)^2\rangle - \langle|\mathbf{r} - \mathbf{r}_c|\rangle^2}{\langle|\mathbf{r} - \mathbf{r}_c|\rangle^2} \quad (5.3.1)$$

as a measure for the deformation of the bubbles, where the average of a quantity B over the

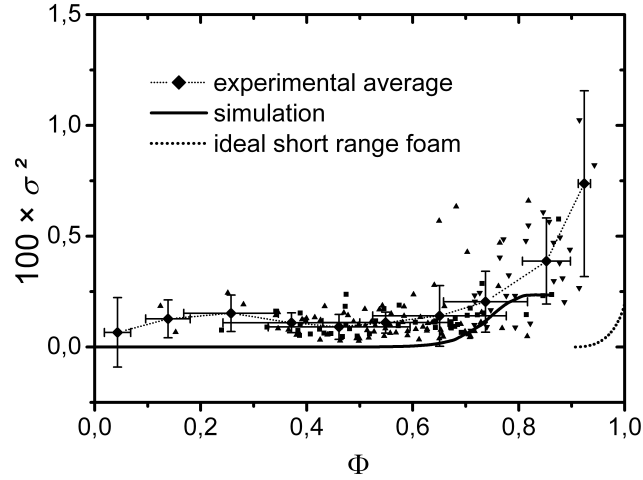


Figure 5.3.1: Experimental (\blacktriangle and \blacktriangledown Myristic acid , \blacksquare Pentadecanoic acid, \blacklozenge average of the experiments) and theoretical (periodic hexagonal foam) values of the deformation parameter σ^2 defined in (5.3.1) versus the area fraction Φ . The experimental averages were calculated over an interval of $[\Phi - 0.5, \Phi + 0.5)$ with the standard deviation plotted as error bar. For comparison the deformation parameter of an ideal short range interaction foam is plotted (lower right).

boundary of the domain is defined as:

$$\langle B \rangle = \frac{\int B(\mathbf{r} - \mathbf{r}_c) \cdot \mathbf{n} ds}{\int (\mathbf{r} - \mathbf{r}_c) \cdot \mathbf{n} ds} \quad (5.3.2)$$

and $\mathbf{r}_c = \langle \mathbf{r} \rangle$. This choice of weighted average coincides with the definition of an area average

$$\langle B \rangle = \frac{\int B dA}{A} \quad (5.3.3)$$

if B is continued from the domain boundary to the interior such that $\int \nabla B \cdot (\mathbf{r} - \mathbf{r}_c) dA = 0$. The deformation parameters σ^2 were determined for 150 experimental bubbles at different area fractions Φ . The result is plotted in figure 5.3.1. An experimental trend is obtained by averaging the σ^2 of domains falling into the same intervals of widths 0.1 of the area fraction Φ . The error bars in σ^2 are due to statistical fluctuations between different domains, while the errors in Φ arise due to a limited field of view and due to a biased choice of images associated with this (Only images where domains ly entirely within the field of view can be analyzed). Values of σ^2 measured in experiments are larger than the theoretical predictions. At low area fractions $\Phi < 0.6$, this deviation is an artifact arising from fractal boundaries of the domains on the scale of the pixels of the images. At larger area fractions $\Phi > 0.6$, where deformations are larger, it is a real effect due to the fluctuations in shape between individual domains. These shape fluctuations are suppressed in the ideal periodic foam simulations. Large domains in

the experiments often exhibit a twofold deformation, which can be much larger than the deformation of a circle toward an ideal hexagon. So the unregular experimental foam is not directly comparable to the idealized theoretical foam. However, the cross over from a wet foam (circular droplets) toward a dry foam (distorted or faceted droplets) in the experiments occurs at the same area fraction $\Phi \approx 0.7$ as predicted for the ideal periodic foam. This cross over happens well below the critical area fraction of closed packed monodisperse circular domains $\Phi_c = 0.9$ and the critical area fraction of poly disperse short range interaction foams $\Phi_c = 0.84$, according to Bolton and Weaire [64]. The latter simulated a polydisperse foam using a random Voronoi lattice as described in [67]. The drying at low bubble fraction is an effect of the long range nature of the electrostatic interactions.

5.4 Discussion

Due to long range dipole interactions foams in Langmuir monolayers do not coarsen persistently but reach a local thermodynamic equilibrium on a well defined length scale. The scale of the bubbles depends on the materials parameters (dipole density, line tension) and diverges as the dipole density approaches zero. Only in this particular limit the foams are intrinsically unstable, the larger structure always has less energy. It has to be mentioned that Berge et al. [65] observed a coarsening in Langmuir foams. The presented images of Berge et al., however, are not at constant gas fraction and consistent also to the interpretation that the size is determined by the gas fraction rather than the relaxation time. The fact of the formation of at least metastable mesoscopic patterns in Langmuir monolayers is well accepted [38, 50, 66]. The bubble shapes of an ideal (monodisperse, hexagonal) dipolar 2D foam in equilibrium are universal. They depend only on the area fraction of the phases and not on material constants. The size of the bubbles is described by a universal size function in units of the equilibrium radius of an isolated domain A_0 and diverges as the bubble fraction approaches $\Phi = 1$. In fact, A_0 is the only materials parameter necessary for the description of ideal dipolar 2D foams. It is a function of the dipole densities, line tension and cut-off length. The cross over from a wet to a dry ideal dipolar 2D foam occurs at a bubble fraction of $\Phi \approx 0.7$ which is significantly lower than the critical area fraction $\Phi_c = 0.91$ of an ideal short range interaction 2D foam [62]. Experimental foams observed in Langmuir monolayers are non-ideal polydisperse foams. The transition point from wet to dry foam, i.e. the area fraction at which bubbles are significantly deformed, agrees quite well with the calculated ideal foam. We suspect that effects of non-ideality just compensate. The measured transition fraction of $\Phi \approx 0.7$ is lower than in polydisperse short range interaction 2D foams $\Phi_c = 0.84$ estimated by Bolton and Weaire [64] by computer simulations using a random Voronoi lattice [67].

The presented theory could be applied also to foams observed in ferrofluids [68, 69].

Chapter 6

2D wetting

The question of wetting is whether and in which morphology a substance on a substrate is thermodynamically stable. If a droplet of a liquid is put on a substrate in principle three different wetting regimes may occur: The first scenario corresponds to a droplet that spreads and covers the whole surface with a thin film (complete wetting), the contact angle is zero. In the second scenario the interfaces form a contact angle between 0° and 180° ($< 90^\circ$ partial wetting, $> 90^\circ$ partial dewetting). In the third regime the contact angle equals 180° and one speaks of complete dewetting. Only in the case of partial (de)wetting the three phases (substance, substrate and matrix phase) meet in a contact line (figure 6.0.1).

For technological application sometimes a certain wetting regime is required. So lubricants and dyes should completely wet the substrate while water on the rain jacket or bacteria on implants are preferred to dewet the substrate. So the understanding of wetting and possibly of a control of the wetting behaviour is an essential question in technology. The wetting behaviour is very sensitive to impurities or substrate roughness. In the last decades technology has advanced enough to create smooth and clean surfaces, which are the precondition for well

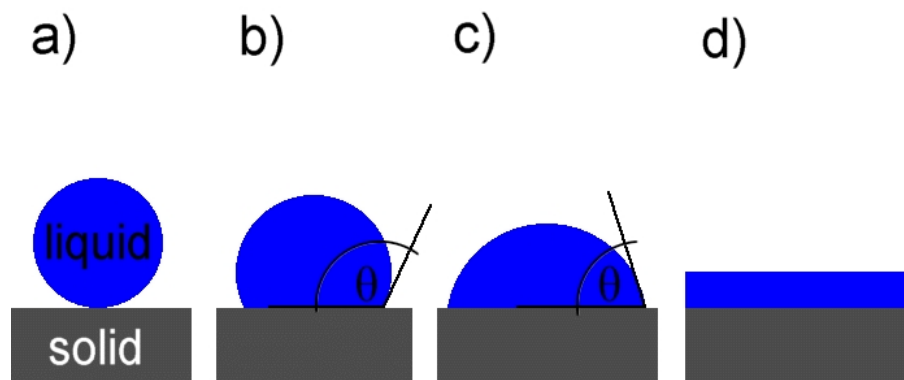


Figure 6.0.1: wetting regimes a) complete dewetting ($\theta = 180^\circ$) b) partial dewetting ($90 \leq \theta \leq 180^\circ$) c) partial wetting ($0 \leq \theta \leq 90^\circ$) d) complete wetting ($\theta = 0^\circ$)

defined wetting experiments. In the last decade wetting research was extended to systems with long range interaction¹. Especially the effect of long range van-der-Waals interactions on pattern formation in self assembling systems is a feature of recent basic research [70–72], or the control of the contact angle by application of an external electrical potential (electrowetting) [73, 74].

6.1 Contact angles in macroscopic 3D systems

Experiments by Young [75] showed that the contact angle on very clean and smooth surfaces is determined by the interfacial tensions

$$\cos \theta = \frac{\sigma_{\text{gs}} - \sigma_{\text{ls}}}{\sigma_{\text{lg}}}, \quad (6.1.1)$$

where σ_{gs} denotes the surface tension of the gas/solid interface and σ_{ls} and σ_{lg} the surface tension of the liquid/solid and liquid/gas interface respectively. The Young-condition (6.1.1) might be interpreted as a force balance with the interfacial tensions pulling on the contact line. One can derive it by minimization of the total droplet energy. It has been shown that it holds also in external gravitational field [76].

The Young-condition holds only for ideal surfaces, i.e. the three phase intersection line is sufficiently flexible in order to equilibrate perfectly. In real systems the contact angle often depends on its history. In general the regressive contact angle is smaller than the progressive contact angle. The contact angle hysteresis occurs because of pinning effects due to surface roughness or chemical impurities on the surface. A detailed description of the effects of nonideality on wetting is given by de Gennes [77].

A feature of recent research is the control of the contact angle making use of the electrowetting effect [73, 74, 78]. Assume a sessile partially wetting droplet of a conductive liquid on an insulating substrate of the thickness d (Figure 6.1.1). Application of an electrical potential U on the droplet and the conductor below the insulating layer reduces the contact angle described by the Lippmann equation (19th century):

$$\cos \theta = \cos \theta_0 + \frac{\epsilon \epsilon_0 U^2}{2\sigma d} \quad (6.1.2)$$

This effect can be explained by an electrical contribution to the surface tension of the substance/substrate interface. Since the substance is conductive the electrical potential within the droplet is a constant. Then the droplet behaves like one plate of a plate capacitor with the capacity

$$C = \frac{\epsilon \epsilon_0 A}{d}. \quad (6.1.3)$$

¹long range force = the range of force is in the order of the extension of the system

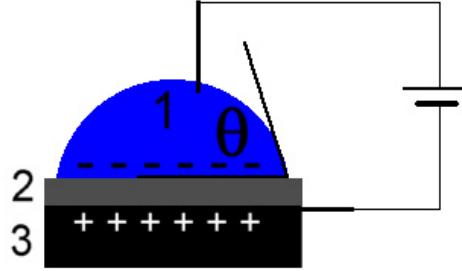


Figure 6.1.1: 1 - conducting liquid; 2 - insulator of thickness d ; 3 - conductor. Application of an electrical potential between the conductor 3 and the liquid 1 changes the contact angle.

The energy stored in the capacitor is given by

$$W_{\text{el.}} = \frac{CU^2}{2} = \frac{\epsilon\epsilon_0 AU^2}{2d} \quad (6.1.4)$$

and can be interpreted as a surface tension

$$\sigma_{\text{el.}} = \frac{\epsilon\epsilon_0 U^2}{2d}. \quad (6.1.5)$$

Plugging this in Young's equation (6.1.1) yields the Lippmann equation (6.1.2). The electro-wetting effect is the result of a change of the surface energy of the substance/substrate interface. At low voltages it agrees well with the experimental results. The change in the contact angle can be several 10 degrees. At higher voltages saturation effects are observed, i.e. the contact angle stays constant even if the electrical potential is increased. The cause of this saturation effect is still controversially debated [73].

For completeness also dynamical contact angles should be mentioned. If the three phase intersection line is moved with a velocity u the contact angle deviates from the static contact angle with the deviation $\Delta\theta$. Experiments were performed by Hoffman in 1975 [79] and he found the empirical relation for small velocities

$$u \propto \Delta\theta^{3\pm 0.5} \quad (6.1.6)$$

which agrees well with the theories of deGennes [77] and Cox [80] which predict an exponent of exactly 3.

6.2 Contact angles in 2D with dipole interaction

6.2.1 2D Young-condition

Assume a 2D liquid (LE) droplet in gas partially wetting an LC substrate. The minimization of the free energy F (3.3.1) with respect to variation of the three phase intersection points yields Young's condition with bare line tensions (appendix A.2):

$$\cos \theta = \frac{\lambda_{\text{LC/G}} - \lambda_{\text{LC/LE}}}{\lambda_{\text{LE/G}}} \quad (6.2.1)$$

For any Δ the contact angle is a materials constant and does not depend on the droplet shape or size nor the structure of the surroundings.

In the appendix the derivation is extended to arbitrary pair interactions and external potentials. Young's condition holds for *any* 2D system, which can be described by the concept of bare line tension and long range potential with dividing length scale Δ . Young's condition is indeed very strong.

Hagen and McConnell [81] published a paper in 1995 about three phase intersection points in Langmuir monolayers. They assumed the validity of Young's condition (6.2.1) without a proof. We will show in subsection 6.2.2 that the direct measurement of contact on experimental images is problematic because of the scaling behaviour of the contact angle with respect to shape invariant scaling.

6.2.2 Scaling laws

Shape invariant scale transformations changes contact angle

Let us apply the shape invariant scale transformation (4.3.1) to a LE-droplet in G partially wetting an LC-wall. Using Youngs equation (6.2.1) for the initial and rescaled droplet we find that the contact angle is changed. Since the curvature κ of the droplet exhibits a singularity at the three phase intersection point the requirement (4.3.2) for the shape invariant scaling law is violated. So the shape is invariant only not too close to the three phase intersection point. Eliminating the LC/LE and LC/G line tensions in both Young-equations one finds the contact angle (shape invariant) rescaling (4.3.1):

$$\theta_1 \rightarrow \theta_2 = \arccos \frac{\tilde{\lambda}_{\text{LE/G},1} \cos \theta_1 - (2 - \tilde{\mu}) \ln \frac{\Delta_2}{\Delta_1}}{\tilde{\lambda}_{\text{LE/G},1} - \tilde{\mu} \ln \frac{\Delta_2}{\Delta_1}} \quad (6.2.2)$$

with the dimensionless line tension $\tilde{\lambda}_{\text{LE/G}}$ defined in equation (4.4.7) and the dimensionless surface potential parameter $\tilde{\mu}$ defined in equation (4.4.8).

In figure 6.2.1 two numerical solutions are shown of the Young-Laplace equation of a partially wetting droplet of size A with two different sets of (unrealistic) model parameters ($\Delta_1, \theta_1,$

$\tilde{\lambda}_{LE/G,1}$) and $(\Delta_2, \theta_2, \tilde{\lambda}_{LE/G,2})$ connected via the shape invariant scale transformation (4.3.1). As one can see the shape of both droplets is the same, with deviations only occurring in the vicinity (distances to the wall smaller than Δ) of the intersection point. The deviations of both solutions close to the LC-wall are such that their contact angles with the LC-wall differ in the way predicted by contact angle scaling law (6.2.2).

A consequence of the contact angle rescaling is the following. Because of the shape invariant scale transformation for the description of sufficiently smooth shapes (4.3.2) it is not necessary to know the physical cut-off-length, and shapes can be described on an arbitrary (4.3.2) scale Δ equally well. This does not hold for the contact angle. If one wants to know the real (physical) contact angle θ_r and the wetting regime it is necessary to know the physical cut-off-length Δ_r (real scale parameter). If the scale parameter Δ is reduced to a point below the optical resolution the contact angle changes are impossible to be resolved optically. So the contact angle θ_r is in principle not directly measurable since it 'happens' most probably below the optical scale. In subsection 6.2.3 a method of determining the scale dependent contact angle $\theta(\Delta)$ by droplet fitting is presented.

Contact angle invariant scale transformation describes shape dependence on droplet size

Here another scale transformation shall be considered, leaving the contact angle invariant. Young's equation (6.2.1) only involves the bare line tensions. Consequently the contact angle

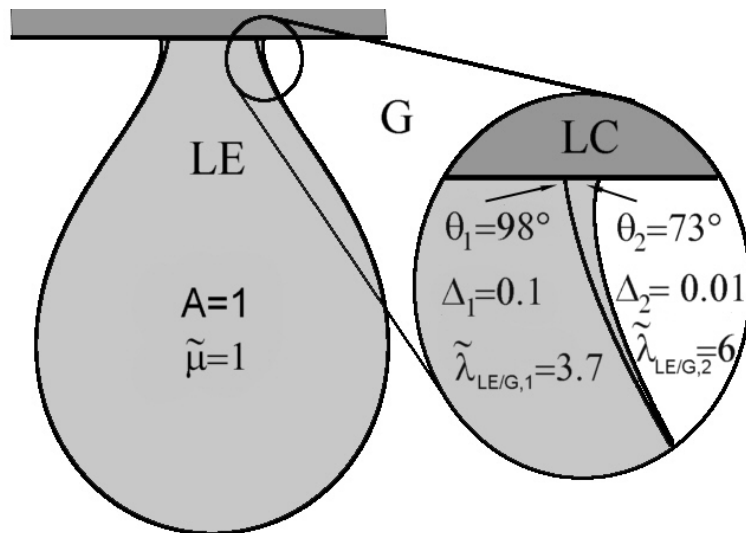


Figure 6.2.1: Two calculated (artificial) droplets connected via shape invariant scale transformation. Close to the edge in the three phase intersection point the shape invariance is violated and two different contact angles connected by equation (6.2.2) occur.

is invariant to a scale transformation, which leaves the bare line tensions unchanged, i.e.:

$$(\Delta_1/\sqrt{A_1}, \lambda_{ij,1}, p_1, \mu_{i,1}) \rightarrow (\Delta_2/\sqrt{A_2}, \lambda_{ij,2}, p_2, \mu_{i,2}) \quad (6.2.3)$$

where

$$\lambda_{ij,2} = \lambda_{ij,1},$$

$$p_2 = p_1, \text{ and}$$

$$\mu_{i,2} = \mu_{i,1}.$$

A contact angle invariant scale transformation (6.2.3) does change the shape of a droplet. The physical relevance of this scale transformation is to describe the changes in shape of a droplet with its size. Since all droplets should have the same bare line tension their contact angle must be the same - a materials parameter dependent on the scale Δ .

If one could determine the contact angle on a well defined scale $\theta(\Delta)$ for experimental droplets of different size one could check out the validity of Young's equation and determine another materials parameter $\theta(\Delta)$ ².

6.2.3 Fitting contact angles with numerical solutions of the Young-Laplace-equation

Experiments Pendant drops of different size were observed in methyl octadecanoate (MOD) monolayers with 1% mol NBD-HDA fluorescence label. The experiments were performed as described in subsection 4.4.1. Four droplets of different size are shown in Figure 6.2.2. Some of the material parameters of this system are well investigated. So are the surface potentials [16], and the bare line tension of the LE/G boundary [26, 54].

Numerics A way to measure the contact angle on a well defined scale is to compare theoretical droplet shapes (numerical solutions of the Young-Laplace-equation) with the fluorescence images of monolayer droplets. The contact angle is the fit-parameter in this droplet fitting procedure (figure 6.2.3).

Experimental droplets usually have droplet sizes ranging between $10 - 10^4 (\mu\text{m})^2$ and the position of droplet interface lines or three phase intersection points can be measured with an accuracy of about $\pm 1 \mu\text{m}$. As long as the chosen Δ is smaller than the resolution of the experimental image, all Δ 's describe the same experimental droplet equally well (cf. shape invariant scaling). The calculation of the integrals in the Young-Laplace-equation (4.2.1) numerically is most efficient on a scale which contains only the measurable information of the monolayer structure. So for numerical treatment the scale of the optical resolution ($\Delta \approx 1 \mu\text{m}$) is the best choice.

²better: the renormalized contact angle $\tilde{\theta}$



Figure 6.2.2: Droplets observed using fluorescence microscopy in the three phase coexistence region of a methyl octadecanoate monolayer (LE: bright, G: black, LC: gray) with different droplet areas $A = 8.9 \times 10^{-10} \text{m}^2$, $2.0 \times 10^{-10} \text{m}^2$, $0.7 \times 10^{-10} \text{m}^2$ and $0.1 \times 10^{-10} \text{m}^2$. The droplet shapes depend on their size.

The Young Laplace equation (4.2.1) together with Young's equation (6.2.1) depend on the set of parameters $(\Delta, \lambda_{LC/G} - \lambda_{LC/LE}, \lambda_{LE/G}, \mu_{LC/G}, \mu_{LE/G}, p)$. In the numerical treatment (appendix A.7) the line tension difference of the LC tensions is replaced by the contact angle, and the pressure is replaced by the area. Also all quantities are made dimensionless (equations (4.4.8) and (4.4.7)) so that the remaining parameters are: $(\Delta/\sqrt{A}, \theta, \tilde{\lambda}_{LE/G}, \tilde{\mu})$

The material parameters of the methyl octadecanoate monolayer phases used for the droplet simulation were taken from [16, 35, 54] (surface potentials: $V_{LC/G} = 0.41 \text{ V}$, $V_{LE/G} = 0.145 \text{ V}$, line tension: $\lambda_{LE/G}^{\Delta=5\text{\AA}} = 0.54 \text{ pN}$).

Rescaling the line tension to $\Delta = 1 \mu\text{m}$ results in the following parameters for the simulation: $\tilde{\lambda}_{LE/G} = 3.81$ cf. equations (4.3.1, 4.4.7) and $\tilde{\mu} = 0.354$ cf. equation (4.4.8). The area of the droplets was measured directly on the image ($A = 8.9 \times 10^{-10} \text{m}^2$, $2.0 \times 10^{-10} \text{m}^2$, $0.7 \times 10^{-10} \text{m}^2$ and $0.1 \times 10^{-10} \text{m}^2$).

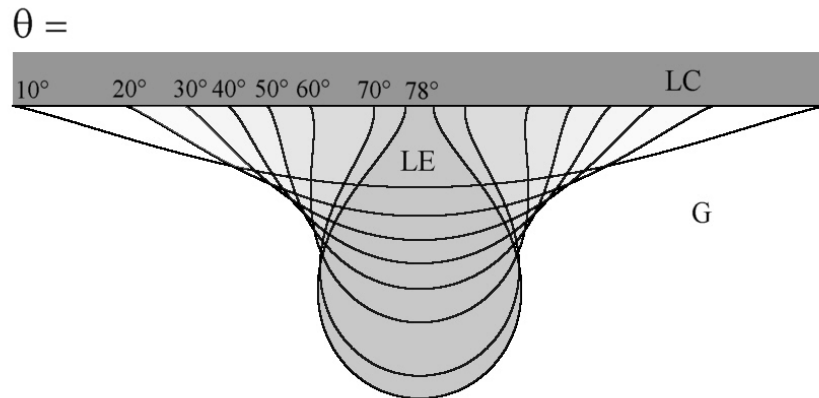


Figure 6.2.3: If the interaction parameters λ^* (respectively $\tilde{\lambda}^*$) and $\tilde{\mu}$ are known (here $\tilde{\lambda}^* = 2.6$, $\tilde{\mu} = 0.354$) the Young-Laplace-equation (4.2.1) has infinity solutions according to the boundary condition θ . Experimental images of droplets can be fitted by solutions of the Young-Laplace equation where the contact angle θ functions as a fit parameter.

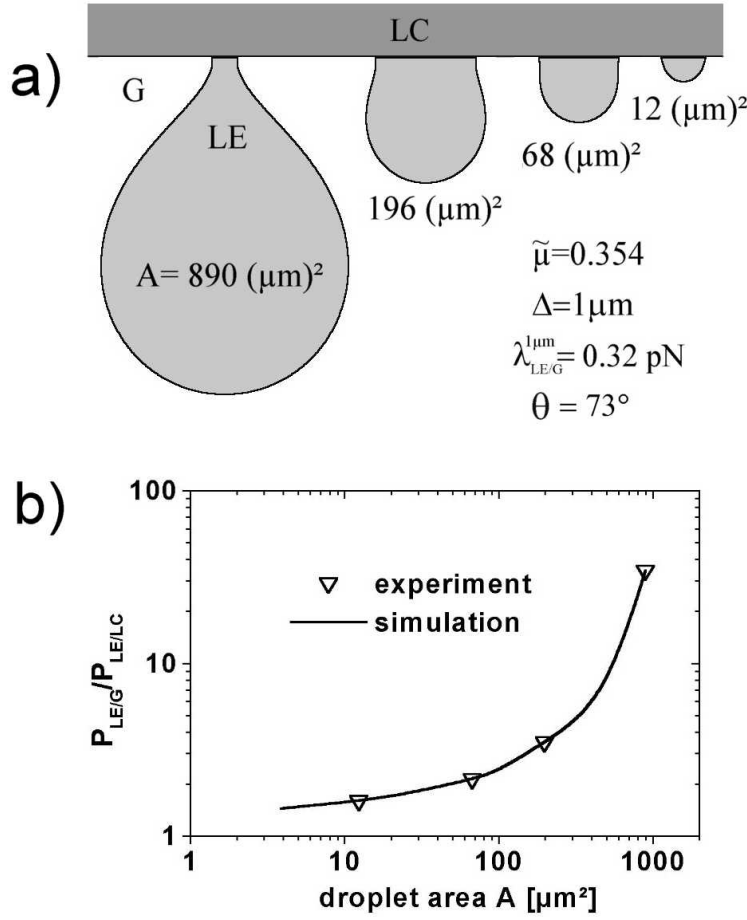


Figure 6.2.4: a) Simulated droplets using $\tilde{\mu} = 0.354$ [16] and $\tilde{\lambda}_{LE/G} = 3.81$ [54], $\Delta = 1 \mu\text{m}$ and the experimental areas of the droplets of figure 6.2.2. A value of $\alpha = 73^\circ$ for the contact angle has been found by shape fitting.

b) (∇) Experimental and theoretical (solid line) values for the global wetting parameter $P_{LE/G}/P_{LE/LC}$. $P_{LE/G}/P_{LE/LC}$ diverges in the simulations as A approaches $A_{dw} \approx 10^{-9} \text{m}^2$. For $A > A_{dw}$ droplets are globally unstable and should not be observed in experiments. Note however that the numerical iteration procedure used for the simulations no longer converges for $A \approx A_{dw}$, so that one can only extrapolate the value of A_{dw} .

The according simulated droplets are shown in figure 6.2.4 a). On this scale ($\Delta = 1 \mu\text{m}$) the fitted contact angle is $\alpha = 73^\circ$. With Young's equation (6.2.1) one finds $\lambda_{LC/G}^{\Delta=1 \mu\text{m}} - \lambda_{LC/LE}^{\Delta=1 \mu\text{m}} = 0.093$ and for the spreading coefficient:

$$S = \frac{\lambda_{LC/G} - \lambda_{LC/LE} - \lambda_{LE/G}}{\lambda_{LE/G}} \quad (6.2.4)$$

it was found $S_{\Delta=1 \mu\text{m}} = -0.7$.

An eye inspection of the droplet shapes in figure 6.2.2 and figure 6.2.4 a) shows reasonable agreement between the numerical solution and experiment. A more quantitative comparison

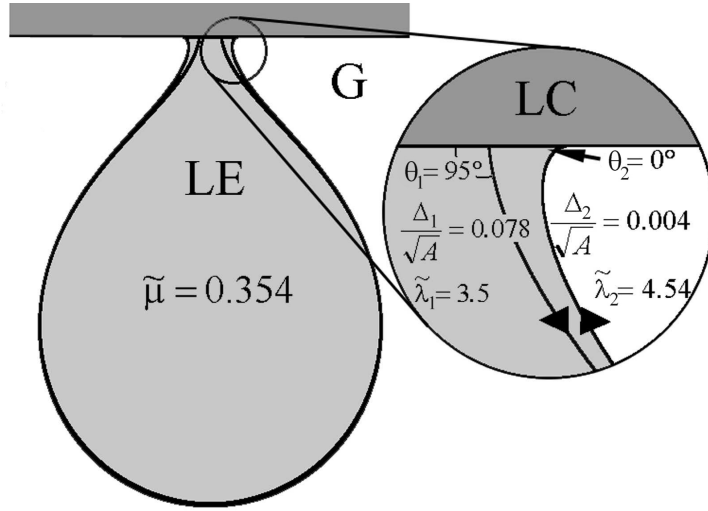


Figure 6.2.5: Numerical solutions of the Young-Laplace-equation (4.2.1) fitted to the largest experimental droplet in figure 6.2.2 demonstrating the shape invariance of the droplet under shape invariant scaling (4.3.1). Close to the wall (distance of the order Δ) the droplet shape is not invariant. It ends at the wall with a Δ dependent contact angle described by eq. (6.2.2). The parameter sets ($\tilde{\mu} = 0.354$, $\Delta_1/\sqrt{A} = 0.078$, $\theta_1 = 95^\circ$, $\tilde{\lambda}_1 = 3.5$,) and ($\tilde{\mu} = 0.354$, $\Delta_2/\sqrt{A} = 0.004$, $\theta_2 = 0^\circ$, $\tilde{\lambda}_2 = 4.45$) of both numerical solutions are related by a shape invariant scale transformation.

may be obtained by measuring the ratio of lengths $P_{LE/G}/P_{LE/LC}$ of the LE/G and LE/LC boundaries (figure 6.2.4 b)). The ratios $P_{LE/G}/P_{LE/LC}$ obtained from the experimental droplets agree well with those calculated by the numerical procedures for all droplet sizes. So the validity of Youngs rule could be confirmed by the experiments.

6.2.4 Conclusion: cut-off-length Δ is a mesoscopic quantity

Now it shall be studied what happens if the scale transformation (4.3.1) is applied in order to reduce Δ to a more realistic value. Remember that Δ_r is expected to be in the range of nm - the length scale of attractive van-der-Waals interactions. The transformation changes the shape of the droplet only close to the LC-wall, where it cannot be resolved in experiment anyhow. The contact angle scaling law (6.2.2) predicts that the droplet with lower Δ partially wets the LC-interface with a lower (for $0 < \tilde{\mu} < 1$) contact angle. Because the contact angle is restricted to values between 0° and 180° also the scale parameter Δ cannot be arbitrary. In the figures 6.2.5 and 6.2.6 the experimental contact angle $\theta_{\Delta=1\mu m} = 73^\circ$ in dependence of the scale parameter Δ using equation (6.2.2) is plotted. One finds real contact angles only for Δ -values larger than $\Delta_{min} = 0.12\mu m$. For values $\Delta < \Delta_{min}$ the contact angle is imaginary and the droplet can no longer be a partially wetting droplet.

Can the droplet be explained within the framework of the outlined theory with $\Delta < \Delta_{min}$?

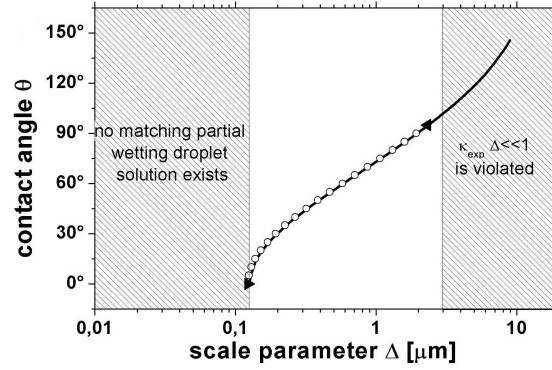


Figure 6.2.6: ○ Fits of the contact angle to the large experimental droplet in figure 6.2.2 with different scale parameters $0.12 \mu\text{m} < \Delta < 2.3 \mu\text{m}$ using bare line tensions related by shape invariant scale transformations. The shapes in the entire Δ -range are lying between the extremal shapes ($\blacktriangleright \hat{=} \Delta = 0.12 \mu\text{m}$ and $\blacktriangleleft \hat{=} \Delta = 2.3 \mu\text{m}$) presented in figure 6.2.5. The fitted contact angles agree well with those calculated via equation (6.2.2) (solid line) - a check for the reliability of the numerics. With increasing Δ the wetting mode changes from partial wetting to partial dewetting. For $\Delta < 0.12 \mu\text{m}$ one finds no numerical solution fitting the experimental droplet. For $\Delta > 2.3 \mu\text{m}$ Δ comes in the range of the radius of curvature of the experimental droplet and the shape invariance fails on the experimentally observable resolution.

The droplet approaching Δ_{\min} from above approaches complete wetting. A straightforward guess is therefore that the droplet for $\Delta < \Delta_{\min}$ can be described by a completely wetting droplet, with a thin film of thickness d (figure 6.2.7 b)). Since we did not observe any thin film in the microscope images, the theoretically calculated film thickness d must be below the resolution of the microscope, if this assumption were true. We will show in the following that the theoretically predicted film thickness is larger than the microscopic resolution and a completely wetting droplet can be excluded.

The Young Laplace equation of a thin LE-film separating an LC and a G semiplane can be solved analytically. For such a film one finds the disjoining pressure (using (4.2.1)) of the film to be:

$$p - \frac{(\mu_{\text{LE}}^2 - \mu_{\text{G}}^2)\pi}{\Delta} = \frac{2\mu_{\text{LE/G}}\mu_{\text{LC/LE}}}{\Delta} \operatorname{arccot} \frac{d}{\Delta} \quad (6.2.5)$$

In equilibrium this pressure is in balance with the Laplace-pressure inside the droplet. We have arranged the terms in equation (6.2.5) in a way that the left hand side does not change upon shape invariant scale transformations. The Laplace pressure inside the pendant droplet can be calculated from the numerical droplet (Appendix A.7). For the large droplet ($A = 8.9 * 10^{-10} \text{ m}^2$) in figure 6.2.4 it is found to be

$$p - \frac{(\mu_i^2 - \mu_j^2)\pi}{\Delta} = 5.7 * \frac{\mu_{\text{LE/G}}\mu_{\text{LC/G}}}{\sqrt{A}}. \quad (6.2.6)$$

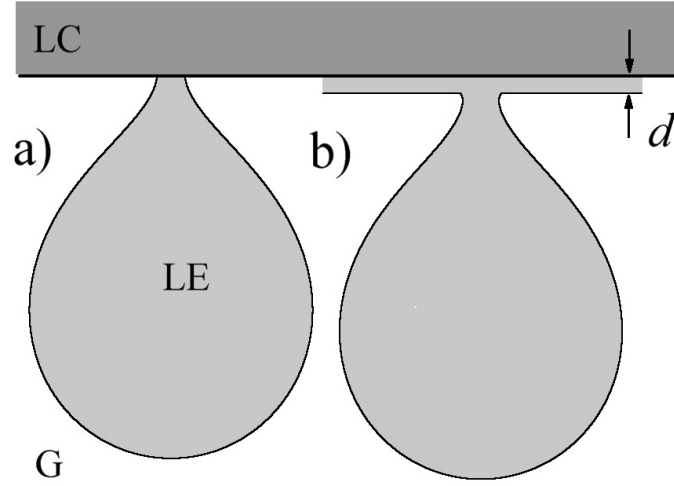


Figure 6.2.7: Sketch of a pendant LE droplet a) partially b) completely (pseudo-partially) wetting an LC/G interface. If the film thickness d of the completely wetting droplet were smaller than the optical resolution an experimentally observed droplet could be interpreted in both ways.

Plugging equation (6.2.6) in equation (6.2.5) one obtains the film thickness d in dependence of the scale parameter Δ :

$$d = \Delta \cot \frac{5.7 * \Delta}{2\sqrt{A}(1 - \tilde{\mu})} \approx \frac{2\sqrt{A}(1 - \tilde{\mu})}{5.7} = 6.8 \mu\text{m} \quad (6.2.7)$$

The approximation in (6.2.7) holds in the whole range of the model ($\Delta \ll \sqrt{A}$). One finds that the film thickness has a value of $d = 6.8 \mu\text{m}$ for all scale parameters Δ - this is large enough to be observed. Because we did not observe such film we conclude that the droplet is a partially wetting droplet and a three phase intersection point exists.

Another weak point of the theory is that only one scale parameter Δ is taken into account instead of one cut-off-length Δ_i for each phase i . If the shape invariant scaling law holds, i.e. the shapes are sufficiently smooth, this simplification is justified and mathematically correct. In the three phase intersection point the scaling law is not valid and that's why the effect of different Δ_i has to be studied: The generalized scaling law (4.3.1) for the line tension has the form

$$\lambda_{ij,2} = \lambda_{ij,1} - \mu_i \mu_{ij} \ln \frac{\Delta_{i,2}}{\Delta_{i,1}} + \mu_j \mu_{ij} \ln \frac{\Delta_{j,2}}{\Delta_{j,1}}. \quad (6.2.8)$$

Note that $\Delta_i = \Delta_j$ yields equation (4.3.1). Now the 'down-scaling' from scale Δ has to be performed considering each individual cut-off-length for the individual line tensions. The calculations are performed in appendix A.8 and show that no set Δ_i in range of some \AA and tens of nm yield a real contact angle $\theta(\Delta_i)$.

So indeed Δ_r is a mesoscopic quantity. With an interpretation of Δ_r as the length scale on which short range attraction overbalance the dipole long range repulsion one would expect Δ_r in the order of nm. With the most common interpretation in literature as the molecular distance between the molecules one would expect even \AA . So the lower limit here determined for Δ_r is at least two orders of magnitude larger than expected - no short range interaction known to us has this range.

It shall be pointed out again that Δ_r has been never measured. In systems with smooth surfaces (4.3.2) it is in principle not measurable from the shape because of the shape invariant scale transformation. So the large Δ is not in contradiction of any *experiment*, only of its suggested *interpretation*. The theory demands a scale parameter Δ for keeping the long range interaction energy finite and within this concept several features in monolayers can be explained satisfactorily. We might think about an interpretation of Δ_r , other than the range of short range attraction:

Pinning effects It might be possible that the LE droplet is pinned to the LC substrate by some impurity. If the impurity - maybe a small particle - is unpolar and larger than $0.12 \mu\text{m}$ in diameter the droplet can be stably attached to the wall via the impurity. However, other observations give evidence that this is not the case. In corresponding experiments we disturbed the thermodynamic equilibrium using an IR-Laser as heating device [12] and let the monolayer relax. During the procedure the three phase intersection points moved and equilibrated very fast ($t \approx 1 \text{ s}$). Pinning on the highly viscous LC wall would not allow this fast movement and equilibration of the droplet shape.

Surface effect of the phase boundaries We suggest an interpretation of the large Δ_r as an interfacial effect on the droplet border line. Note that the Δ which enters the Young-Laplace equation occurs only in integrals describing the electrostatic pressure on the droplet interface. With this interpretation Δ has the meaning of a dipole correlation or healing length on the phase boundary and describes the nonideality (in the sense of Gibbs) of the 1D interface. Previous papers [16, 54, 82] report on a change of the materials parameters on phase boundaries from that in the bulk, which is consistent with this interpretation. In 3D van der Waals already presented a microscopic theory describing the density profile of a liquid on a liquid/gas interface by a correlation length ξ [83], later Buff, Lovett and Stillinger [84] extended the theory including surface fluctuations leading to a broadening of the density profile. Presumably in 2D the surface potential cannot switch from its value in the LE-phase toward that in the G-phase on length scales smaller than $0.1 \mu\text{m}$ as the electric fields around this transition become energetically too costly. Another explanation might be unpolar impurities which form a kind of 1D monolayer on the 'droplet surface'.

6.2.5 Discussion

It has been found theoretically that Young's condition in 2D is not affected by external or pair interaction potentials. Contact angle measurements by droplet fitting approve this result in a Langmuir monolayer - leaving the physical meaning of the scale parameter Δ open for interpretations.

One should expect a similar universality of Young's condition in 3D. In 1966 Gretz [85] found a deviation of experimental contact angles from Young's condition if the droplets are very small. He resolved the problem by postulating a line energy proportional to the length of the three phase intersection line. The (3D) line tension causes a size dependence of the contact angle for small droplets. Young's condition (6.1.1), modified by the line tension term then yields the Gretz-condition

$$\cos \theta = \frac{\sigma_{\text{gs}} - \sigma_{\text{ls}} - \frac{\lambda_{\text{gls}}}{R \sin \theta}}{\sigma_{\text{lg}}}, \quad (6.2.9)$$

where λ_{gls} is the line tension of the three phase intersection line and R the curvature radius of the cap. The Gretz equation is an empirical equation but quite popular in the description of small polymer drops [86]. Joanny and de Gennes [87] theoretically predicted a positive line tension. Further computer simulations were published indicating a violation of Young's law for droplets containing polymer chains [86,88,89], but in quite good agreement with the Gretz equation.

The deviation from Young's law arises from another interfacial energy - the line tension of the three phase intersection line. One might conclude that the experiments and simulations with 3D systems in the length scale of van-der-Waals forces approves that the contact angle is determined by the interfacial tensions and not by the long range interaction.

6.3 Shape instabilities of wetting droplets

Free circular domains become unstable if they exceed a certain size (see subsection 3.4)

$$\sqrt{A_2} = \sqrt{A_0} e^{7/3}, \quad (6.3.1)$$

where A_2 denotes the critical area with respect to a two-fold deformation and A_0 is the equilibrium area of an isolated domain (3.4.2). Free droplets with a larger area are deformed. For these droplets several different shapes fulfil the Young-Laplace-equation 4.2.1 instead of one solution for smaller sized droplets (circle). The question arises whether these shape bifurcations occur also for wetting droplets and whether the presence of the dipolar substrate has a stabilizing or destabilizing effect.

6.3.1 Theory

The straightforward approach would be to find shapes fulfilling the Young-Laplace-equation using the numerical procedure described in 6.2.3. If several metastable droplet shapes exist also for the Young-Laplace-equation several solutions for one set of parameters $(\tilde{\mu}, \tilde{\lambda}_{\text{LE/G}}, \Delta/\sqrt{A}, \theta)$ exist.

However, testing the numerical procedure showed that in a restricted region of parameter space one and only one solution of the Young-Laplace equation could be found. Most probably this is a property of the used algorithm. The iteration procedure does not converge in the parameter range where bifurcations are expected or the algorithm finds only one shape fulfilling the Young-Laplace equation even if there exist many. So this approach fails here.

Khattari and coworkers (the author included) [90] developed a theory for a simplified geometry avoiding an explicit calculation of the shape. Assume an LE-droplet wetting a LC-substrate in gaseous surroundings. The droplet is approximated by a circular segment attached to a straight wall (figure 6.3.1). This circular segment is determined by only two parameters: the droplet area A and the angle ϕ on the intersection point of the sphere and the wall (figure 6.3.1).

Note that the angle ϕ is not equivalent to the contact angle θ . It is a shape parameter describing how 'pendant' the droplet is. If shape bifurcations occur, several ϕ exist which locally minimize the free energy. The contact angle θ is a materials parameter while ϕ is not.

For this simplified geometry it is now possible to find an analytic expression for the free energy

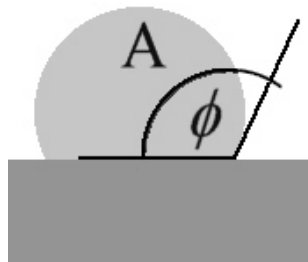


Figure 6.3.1: The shape of a wetting droplet is modeled by a circular segment with the area A and the angle ϕ . The parameter ϕ describes how 'pendant' the droplet is and is not equal to the contact angle θ . $\phi > 90^\circ$ correspond to pendant droplets and $\phi < 90^\circ$ to sessile droplets.

(3.3.1) of the circular segment³. It has been tested by comparison with numerical calculations of the free energy for some arbitrary interaction parameters.

In thermodynamic equilibrium the free energy is a minimum with respect to the shapes represented by ϕ under constraints of constant droplet area

$$\left. \frac{\partial F}{\partial \phi} \right|_A = 0. \quad (6.3.5)$$

Equation (6.3.5) has been solved numerically. A special case with a continuous splitting into two (meta)stable branches is shown in figure 6.3.2. Generally the following results could be found:

- the maximum number of solutions for one set of materials parameters is 2
- shape bifurcations occur only if $\mu_{LE/G}$ and $\mu_{LC/G}$ have the same sign
- shape bifurcations occur only if the dipole interaction within the droplet is stronger than within the wall $|\mu_{LE/G}| > |\mu_{LC/G}|$
- the critical area always exceeds the critical area A_2 of a free droplet (6.3.1)

Generally, the circular segment model predicts a stabilizing effect of the substrate on the wetting droplet. In methyl octadecanoate holds $\mu_{LC/G} > \mu_{LE/G}$ and therefore according to the circular segment model all the droplets presented in the last subsection 6.2 are the only solution of the Young-Laplace equation. In another scenario in methyl octadecanoate, where LE-droplets wet LC-foams ($\mu_{LE/G} > \mu_{foam/G}$), bifurcations are expected if the droplet area at least exceeds the critical area of a free domain A_2 . Using equations (6.3.1) and (3.4.2) and the materials parameter for methyl octadecanoate [16, 54] yields a critical area of $A_c > A_2 \approx 40 \times 10^{-10} \text{ m}^2$. This is 4 times larger than the largest pendant droplet observed in the system.

³Khattari found for the free energy the expression

$$\begin{aligned} F = & 2R\lambda_{LE/G} \left(\phi \left(1 - 2 \frac{\mu_{LE/G}\mu_{LC/G} \cos(\phi)}{\lambda_{LE/G}} - \frac{\mu_{LE/G}^2}{\lambda_{LE/G}} \ln \frac{8R}{\Delta e} \right) \right. \\ & + \sin(\phi) \left(\lambda_{LC/LE} - \lambda_{LC/G} + \frac{\mu_{LE/G}\mu_{LC/G}}{\lambda} \ln \frac{4R^2 \sin^4(\phi)}{\Delta^2} \right. \\ & \left. \left. - \frac{\mu_{LE/G}^2}{\lambda_{LE/G}} \ln \frac{8R \sin^2\left(\frac{\phi}{2}\right) \tan\left(\frac{\phi}{2}\right)}{\Delta} - \frac{\mu_{LE/G}^2}{\lambda_{LE/G}} \Im \left(\text{dilog}(1 + e^{i\phi}) - \text{dilog}(1 - e^{i\phi}) \right) \right) \right) \end{aligned} \quad (6.3.2)$$

with

$$\text{dilog} x := - \int_1^x \frac{\ln t}{t-1} dt \quad (6.3.3)$$

and

$$R = \sqrt{\frac{A}{\phi - \frac{1}{2} \sin 2\phi}}. \quad (6.3.4)$$

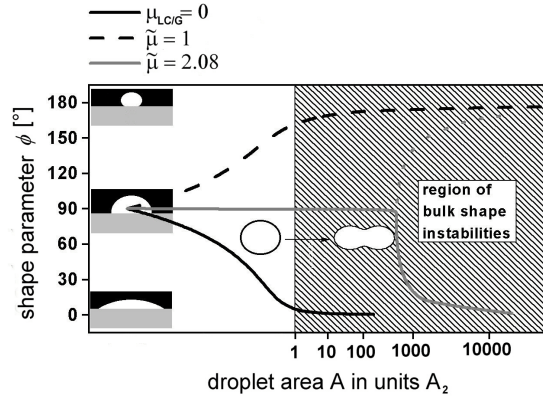


Figure 6.3.2: (Taken from [90]) Calculated shape parameter ϕ by numerical solution of equation (6.3.5). The scale has been set to $\Delta/\sqrt{A} = 0.001$ and the line tension difference of the LC-line tensions is set to zero on any scale $\lambda_{LC/G} - \lambda_{LC/LE} = 0$ (In fact with this assumption the LC-line tensions do not obey the shape invariant scaling transformation and represent different physical systems on each scale. For the problem here this is not important.) The dimensionless line tension $\tilde{\lambda}_{LE/G}$ (4.4.7) has been used as control parameter in the numerics and this corresponds to a change in area keeping the materials parameters Δ , $\tilde{\mu}$ and $\lambda_{LE/G}^\Delta$ constant. ϕ is plotted versus the droplet area in units of A_2 - the critical area of two-fold deformation of an isolated droplet (6.3.1).

Solid black line: μ_{LE} differs from $\mu_G = \mu_{LC}$. Dashed black line: $\mu_{LE} = \mu_{LC}$. Gray lines: value for $\tilde{\mu}$ on which a continuous split into two bifurcation branches occurs.

Solid gray lines represent stable contact angles while dotted lines represent metastable solutions.

6.3.2 Experiment

In the paper [90] an experiment is presented which is interpreted as a shape bifurcation of wetting droplets in a methyl octadecanoate monolayer. After a local distortion of the monolayer pattern a partially wetting droplet remained for 0.5 s in a metastable state before it spontaneously flips to another shape. Fluorescence images are shown in figure 6.3.3.

The materials were used as described before in subsection 4.4.1 (1% mol NBD-HDA fluorescence label). The monolayer was spread to an area of $\approx 40 \text{ \AA}^2$ and slow expansion to $\alpha \approx 100 \text{ \AA}^2$) leads to the formation of dry LE- and LC-foams in the gaseous matrix phase. The droplet in figure 6.3.3 was created by cutting a LE-lamella with the IR-laser. The laser was focused on the air water interface and used at low power ($\approx 100 \text{ mW}$). The relaxation of the monolayer to this local distortion has been observed and recorded.

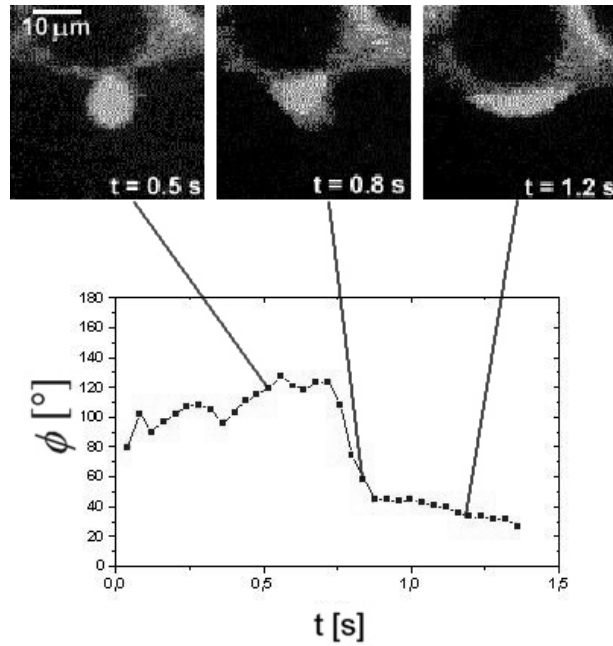


Figure 6.3.3: Upper: Fluorescence image in the three phase coexistence region (LE- and LC-lamellas in G) of methyl octadecanoate monolayer. For about 0.5 s the LE-droplet wetting the LC-foam bubble remains in a pendant droplet shape (left image). Then it flips spontaneously into a flatter sessile droplet shape (right image). Pinning effect or shape bifurcation of wetting droplet?

Below: The shape parameter ϕ from a circular segment model plotted versus time. At $t = 0$ s a stable droplet was established.

6.3.3 Discussion

In the qualitative behaviour experiment and theory agree, i.e. the theory predicts bifurcations of wetting droplets if LC-foams are wetted. However, the predicted size of a bifurcating droplet and the experimentally observed one are in obvious contradiction. The area of the experimental droplet is small ($\approx 1 \times 10^{-10} \text{ m}^2$) compared to the expected critical size (larger than $40 \times 10^{-10} \text{ m}^2$).

In fact the theory takes a very simple geometry into account and one might doubt whether the behaviour is modeled correctly. On the other hand the stabilizing effect of the surroundings on monolayer domains is also found in the 2D foams, where bubble sizes exceed the critical area of two-fold deformation because of the presence of neighbour-bubbles. And the experimental bifurcating droplet is indeed very small compared to the area of other wetting droplets or LE-domains observed in the system.

One interpretation is that the theory assuming constant bare line tensions and surface potentials reaches its limits in this case. This interpretation is suggested in [90] and the graph 6.3.2 is plotted versus the ordinate $\mu_{\text{LE/G}}^2/\lambda^*$ instead of the droplet area A . If the materials

parameter $\mu_{\text{LE/G}}^2/\lambda^*$ is not a constant but dependent on the surrounding structure also smaller droplets might bifurcate. Another experiment by Khattari et al. [48] also found a destabilizing effect of LC-surroundings which cannot be explained within the presented theory. The theory predicts generally an increase of the critical droplet area as the local area fraction of G decreases.

Another interpretation of the experiment is as a pinning effect, rather than a droplet shape bifurcation. Impurities adsorbed to the LC/LE/G-contact point and that's why the droplet could not equilibrate immediately after the LE lamella was cut. So the contact point was pinned to the substrate for half a second. Then the droplet overcame the pinning impurity and flipped into equilibrium. A detailed description of pinning in 3D macroscopic systems is given in [77].

Chapter 7

Biological control of wetting transitions

There is no doubt about the importance of 3D wetting in our macroscopic world or in the biological micro cosmos (figure 7.0.1). The question arises whether 2D wetting in cell membranes plays a similarly significant role in biological processes within membranes. The wetting behaviour could function as a trigger for chemical reactions of surface active substances dissolved within different 2D phases. Biological membranes are very complex systems consisting of several phospholipid components as well as proteins. The length scale of the self assembling patterns of phospholipids is in the range of nm [91] and not easily accessible to direct observation. Biology discovered the role of several proteins for regulation and as trigger for other processes, so for instance signal transduction. If processes within membranes are investigated proteins are within the focus of research . Here the thermodynamics will be studied, i.e. structure formation and wetting of 2D phases within biological membranes modeled with a phospholipid Langmuir monolayer.

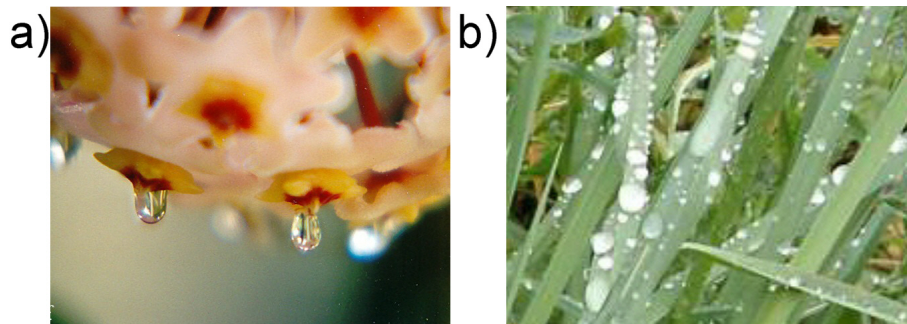


Figure 7.0.1: Wetting in biological systems. a) partial wetting of nectar on a flower of *Hoya carnosa* b) partial dewetting of rain drops on grass (*Porneo spez*)

7.1 Controlling of wetting behaviour - theoretical approach

For technical application and the understanding of biological processes within cell membranes it might be important to investigate how the wetting behaviour of 2D phases could be controlled by external manipulation, for instance by temperature change, an external potential or the concentration of an additional substance in the subphase. Of special interest are transitions from complete or partial wetting (phases are in contact) to complete dewetting (phases are not in contact) or vice versa. The external manipulation could be used either to produce well defined patterns or to trigger chemical reaction between chemicals dissolved in the different phases.

In macroscopic 3D systems the contact angle, i.e. the wetting mode, is determined only by the surface tensions of the different interfaces. If the wetting occurs in an external field, for instance gravity, the contact angle and wetting mode remain unchanged while a characteristic dependence of the shape on the droplet size (volume) occurs. In 2D wetting three kinds of parameters determine the wetting mode: the line tensions between the phases λ_{ij} , the surface potentials $\propto \mu_i$ and the cut off length Δ . Young's condition for the contact angle holds, however the contact angle is not directly measurable by image analysis - due to the behaviour of the droplet interface close to the 2D substrate. In contrast to macroscopic 3D systems the line tensions λ_{ij} are defined only together with stating the corresponding scale of observation (cut-off length) Δ , which is also not directly accessible to measurement.

The effect of the line tensions on the wetting mode is obvious, more complicated might be to understand the effect of the surface potentials and the cut-off length. In order to understand the effect of the different parameters on the wetting mode the scale transformation with respect to some special cases will be studied:

1. the surface potentials of all phases are equal $\mu_i = \mu_j$ (for all phases i and j)

Plugging this into the scaling law for the line tension (4.3.1) one finds

$$\lambda_{ij}(\Delta_1) = \lambda_{ij}(\Delta_2), \quad (7.1.1)$$

i.e. the line tensions do not depend on the choice of the cut-off-length. And for the curvature one finds using the Young-Laplace equation (4.2.1)

$$\kappa = \text{const}, \quad (7.1.2)$$

i.e. all interfaces between the 2D phases are circle segments. Setting all surface potentials to the same value is equivalent with switching off the dipole interaction. The resulting system behaves like a 3D macroscopic system with no external field. The structure

is formed out of circular segments without any characteristic length scale. As in 3D macroscopic systems larger structures are favoured because they have a lower interfacial energy per unit area than the smaller ones. One expects macroscopic phase separation instead of the formation of mesoscopic patterns.

2. the surface potentials of the substrate (phase 1) and the substance (phase 2) are equal, but unequal to the surface potential of the matrix phase (phase 3) $\mu_1 = \mu_2 \neq \mu_3$

Plugging this into the scaling law (4.3.1) for the line tension leads to a dependency of the line tensions λ_{13} and λ_{23} on the scaling parameter

$$\lambda_{13} = \lambda_{13}(\Delta), \quad \text{respectively} \quad \lambda_{23} = \lambda_{23}(\Delta) \quad (7.1.3)$$

while λ_{12} is a constant

$$\lambda_{12}(\Delta) = \text{const.} \quad (7.1.4)$$

Due to competition between short range attractive and long range repulsive forces (line tension versus dipole repulsion) the formation of patterns on a well defined length is favoured. Plugging $\mu_{13} = \mu_{23}$ into the scaling law for the contact angle (6.2.2) leads to

$$\alpha_1 \rightarrow \alpha_2 = \arccos \frac{\tilde{\lambda}_{23}(\Delta_1) \cos \alpha_1 - \ln \frac{\Delta_2}{\Delta_1}}{\tilde{\lambda}_{23}(\Delta_1) - \ln \frac{\Delta_2}{\Delta_1}} \quad (7.1.5)$$

A contact angle of $\alpha_2 = 0$ implies always a contact angle $\alpha_1 = 0$ independent of Δ_1 and Δ_2 . And $\alpha_1 > 0$ leads for all Δ_1 and Δ_2 to a real solution for $\alpha_2 > 0$. So in this system the scale parameter can be chosen arbitrarily small and transforms a droplet without changing the wetting mode (partial to complete or complete to partial).

3. all surface potentials are unequal $\mu_i \neq \mu_j$ for $i \neq j$ (general case)

As discussed already in section 6.2.4 there generally exists a lower limit for Δ on which the contact angle becomes zero. At further decrease of Δ the droplet would be unstable and spread to a film. The fact that the coexistence of such a film together with the droplet could be excluded is also shown in section 6.2.4.

In order to predict wetting transitions by changing some external parameter the interaction parameters have to be known very well. In most systems this is not the case, but let us try to formulate some general rules: Slight changes of materials parameters have the largest effect on the wetting behaviour if the cut-off length Δ is small and substance phase and substrate phase have almost the same surface potential. The bigger Δ the smaller the effect of a parameter change.

7.2 Enzymatic control of wetting behaviour in biomimetic system

Biological membranes consist of lipid bilayers containing other constituents like proteins or cholesterol. In general membranes are asymmetric, i.e. the composition of the intra- and extra cellular monolayer of the membrane is different. Membrane potentials arise through this asymmetry of the dipole densities and due to differences in ion concentrations between the intracellular and extracellular fluid.

Langmuir monolayers are common model systems in order to study the mode of operation of enzymes in cell membranes [92–99]. A. Fischer, student of biology, prepared her diploma thesis with the task to investigate how enzyme reactions are suitable for the triggering of wetting transitions. Experiments are presented in subsection 7.2.2.

In section 7.3 the possibility of controlling wetting reactions with enzymes in membranes is discussed in the frame work of the theory outlined in chapter 3.

7.2.1 Fundamentals - lipid-enzyme reactions in membranes

Lipids are esters of glycerol (a triple alcohol) with three (organic) acids. In phospholipids one of the organic acids is an ester of phosphoric acid and an alcohol. This part is hydrophilic and forms the 'head' of the surfactant. The two other organic acids are mostly fatty acids and their carbon chains form two hydrophobic tails (figure 7.2.1). In living cells they are involved in chemical reactions catalyzed by enzymes - i.e. proteins located in the subphase or in the membrane.

Enzyme controlled manipulations of phospholipids in membranes are for instance flips from the inside monolayer to the outside (controlled by flippases), the phosphorylation of phospholipids

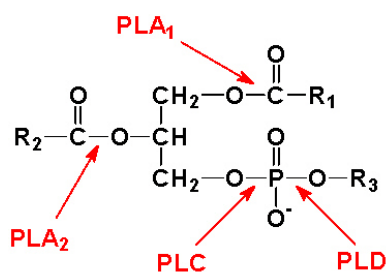


Figure 7.2.1: Phospholipids consist of glycerol (involving the three carbon atoms in the center), fatty acids with the hydrophobic residues R₁ respectively R₂, phosphate group and residue R₃ which can be choline, inositol (containing a sugar ring) or others. The lipases PLA₁, PLA₂, PLC and PLD catalyze the hydrolysis of the ester bonds marked in the figure.

(e.g. of phosphatidyl-inositol-phosphates) with a parallel reaction of adenosine-triphosphate (ATP) to adenosine-diphosphate (ADP) or the catalytic hydrolysis of ester bonds in the phospholipids by lipases (PL). In general these enzymes act specific on certain ester bonds as shown in figure 7.2.1. The hydrolysis with PLC changes the structure of the surfactant head by cutting a soluble group which is solved in the subphase. This reaction is expected to have an effect on the dipole moment of the phospholipid, i.e. the surface potential of the monolayer phases. Using PLA cuts one fatty acid from the phospholipid and results in two different kinds of surfactants. This results in a mixture of several components and one expects a change of the phase behaviour, i.e. occurrence of new (mixed) phases with new properties after injection of the enzyme. Interaction with lipases and monolayers were investigated for instance by Pierony et al. [93]. Experiments with PLC in DPPC monolayers were performed for instance by Grandbois et al. [100] and experiments with PLA₂ in monolayers by Dahmen-Levison [95,98]. Since flip-flop processes do not occur in Langmuir monolayers and the phosphorylation demands the additional ATP-ADP dephosphorylation, experiments on enzymatic wetting in our group were focused on the catalyzed hydrolysis of phospholipids with lipases as the simplest reaction type.

7.2.2 Experimental - PLA₂ hydrolysis of DPPC/cholesterol mixture

For wetting experiments three phase systems with two liquid phases or one liquid and one gaseous phase are required. Tests of several lipases and phospholipids showed that a suitable system is a phosphatidylcholine/cholesterol mixture in combination with PLA₂ (the authors contribution is mainly in this part of the experiments). So for instance DPPC¹ or DMPC² mixed with dihydrocholesterol, providing two liquid phases in G. DMPC/dihydrocholesterol has been investigated by McConnell et al. for several years and is suitable for studying wetting. So did Hagen and McConnell in the first paper on 2D wetting [81].

The injection of PLA₂ changes the area fraction of the phases but does not lead to the formation of rigid monolayer. So PLA₂ is suitable for the wetting experiments. In order to be sure that a chemical reaction takes place Fischer measured the activity of the enzyme in the bulk and the air/water interface by AMD-TLC³. She found a higher activity on the interface by a factor of ≈ 1.2 . A qualitative AMD-TLC result for the enzyme reaction is plotted in figure 7.2.2 [101]. Commonly in literature the activity of the enzyme is indirectly monitored by some physical quantity as surface pressure [92, 97] or structure of fluorescence images. With AMD-TLC

¹dipalmitoyl-phosphatidylcholine

²dimyristoyl-phosphatidylcholine

³Automated Multiple Development (AMD) technique is suitable for the separation of multi component mixtures in thin layer chromatography (TLC)

the educts and products can be identified and indicate that indeed the enzyme reaction is responsible for the observed structural changes.

Fluorescence images before and after the injection of the enzyme are shown in figure 7.2.3. For experimental details please consult [102]. As one can see the injection of enzyme leads to a change of the area fraction of the phases. The number of phases does not change. The structures after the hydrolysis have a smaller length scale which indicates a decrease of the line tensions - as one would expect of a mixture compared to pure substances. However, before and after the injection of the enzyme partial wetting can be observed. So the change of the line tension did not cause a change of the wetting mode to complete dewetting.

In another experiment 46% mol DMPC and 54% mol dihydrocholesterol together with 2% NBD-PC fluorescence label were spread from chloroform solution with a total concentration of ≈ 2 mM (the unit M is equivalent to mol/l). As subphase a buffer consisting of 150 mM NaCl, 5 mM CaCl₂ and 10 mM TRIS was used. The spreading was performed at maximum area (210 cm²) of the film balance. After relaxation for 30 min the monolayer was compressed at very slow rate (1×10^{-2} cm²/s) to an area of 80 cm². Now three phase coexistence with three phase intersection points could be observed. The enzyme PLA₂ had been injected into the subphase. For this a teflon tube and a syringe was used. The injection was located just beside the objective and performed very slowly in order to keep the flow within the monolayer small. The final concentration of enzyme in the subphase was about 7×10^{-3} units/l [101,103]. Also here partial wetting was observed before and after the injection of the enzyme. However, the counting of the number of partially wetting domains compared with completely dewetted

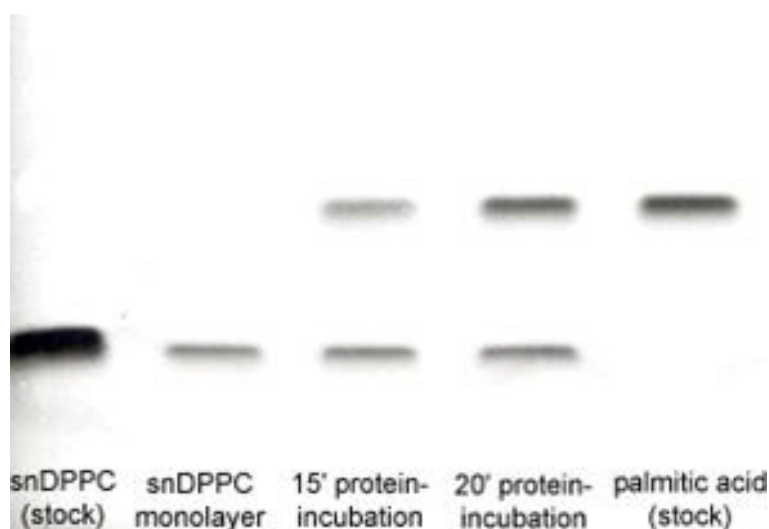


Figure 7.2.2: DPPC monolayer hydrolysis by PLA₂. The monolayer composition in dependence of reaction time was investigated using a AMD-TLC device. For comparison the pure educt (left) and product (right) were measured. The experiment allows to monitor the ratio of educts and products in time. For details please consult [102].

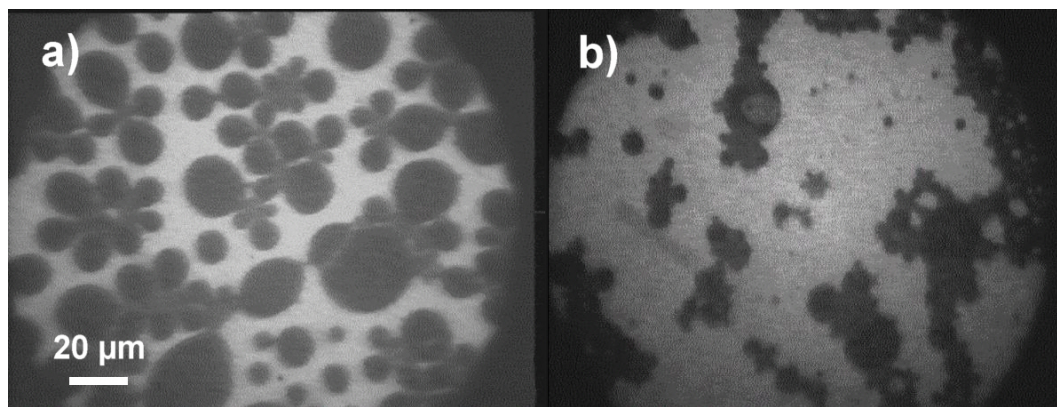


Figure 7.2.3: Fluorescence image of DPPC/dihydrocholesterol monolayer a) before and b) after injection of PLA₂. The composition of the phases is changed and results in a dramatic change in area fraction and structure. Before and after the hydrolysis three phases are observed (bright, grey and dark) and partial wetting is observed [101].

domains showed some tendency in time which might be interpreted as result of the enzyme reaction. Ruschel and Khattari counted the number of dewetted and wetted domains within a time interval of 60 s in the visible region of the monolayer [103]. The results are shown in figure 7.2.4. The occurrence of wetting or dewetting could be a result of the hydrolysis.

7.3 Discussion

The experiments indicate that a catalytic hydrolysis of monolayer phospholipids leads to a decrease of the line tension and structural changes. In both observed systems partial wetting domains are stable before and after the hydrolysis. In DMPC/dihydrocholesterol mixture the occurrence of dewetted and partially wetting domains changed significantly after the injection of the enzyme and could be an effect of the hydrolysis. The hydrolysis of DPPC or DMPC does not seem to be suitable in order to trigger the wetting mode but seems to be suitable to affect the length scale and topology of the formed patterns. Probably in other phospholipid/enzyme systems also a switching of the wetting mode by the injection of the enzyme can be induced. Are these results transferable to biological membranes? Different miscibilities of lipids lead to phase separation or the formation of lipid rafts in biological membranes [99, 104]. Since several components are involved in the membrane several phases with intersection points are expected and 2D wetting occurs. In membranes the length scale of the formed domains is much smaller (nm) than in Langmuir monolayers (μm) [91]. If the order of magnitude of the determined cut-off-length in MOD monolayer $\Delta_r \approx 0.1 \mu\text{m}$ (section 6.2.4) is similar in biological membranes, then the theory presented here reaches its limits. Δ is then large compared to the length scale of the system and the long range dipole interaction has only slight effects on the droplet shape

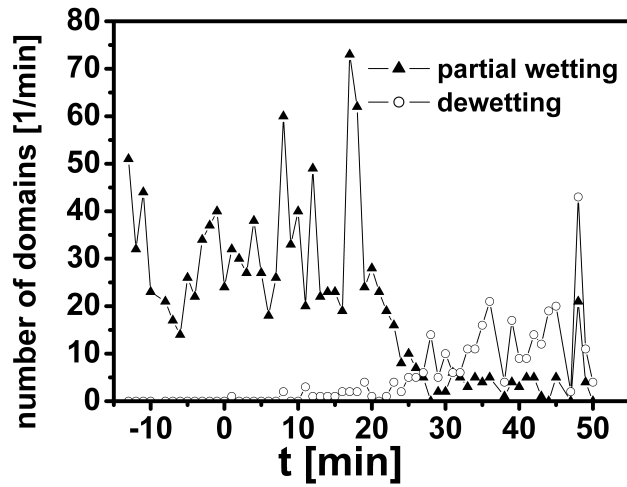


Figure 7.2.4: Occurrence of partial wetting domains and completely dewetted domains in DMPC/dihydrocholesterol mixture after injection of PLA₂ versus time. The injection was performed at $t = 0$. Although the stability of the wetting phase does not change with respect to the wetting mode the relative occurrence of partial wetting compared with dewetted domains decreases in time [103].

and stability. Small changes of the materials parameters have only small effects on the wetting mode, and parameter scenaria which were found to be optimal for wetting control (section 7.1) do not occur. However, if Δ is self consistent (i.e. the dipolar healing length depends on the length scale of the structures) then the results of the theory should be well transferable to biological membranes.

Chapter 8

Apparent violation of Gibbs' phase rule in monolayers

8.1 First order phase transition and Gibbs' phase rule

If the free energy F (or any other thermodynamical potential) is not differentiable with respect to the thermodynamic state variables (for instance pressure p) one speaks of a phase transition of first order at this point. Characteristic for this phase transition is a latent heat and an entropy change upon conversion from one phase to another.

Assume a system consisting of K components forming P phases. The following variables are needed in order to describe the thermodynamic state: the temperatures T_i (P variables) and the partial pressures p_{ij} of component j in phase i (KP variables).

The system is in thermodynamic equilibrium if thermal equilibrium $T_i = T$ ($P - 1$ equations), mechanical equilibrium $\sum_j p_{ij} = p$ (in the limit of plane interfaces, $P - 1$ equations) and diffusion equilibrium $\mu_{ij} = \mu_j$ ($(P - 1)K$ equations) are reached. Collecting the terms for the independent variables and equations gives the degrees of freedom f of the system

$$f = 2 + K - P. \quad (8.1.1)$$

This relation is the Gibbs' phase rule. It says for instance that in a one component system the coexistence of three phases is restricted to 0 dimensions, i.e. the triple point, while the pressure for two phase-coexistence is fixed for a given temperature.

How strong is the Gibbs' phase rule? The first assumption made for the theory is the intensivity of the pressure p ¹ and temperature T . I.e. the derivation of Gibbs' phase rule makes only sense within the limits of vanishing long range interactions. The short range interactions are not dealt with explicitly, but within the phase-concept they are included in the chemical potentials

¹the claim is equivalent to the free energy F to be an extensive variable

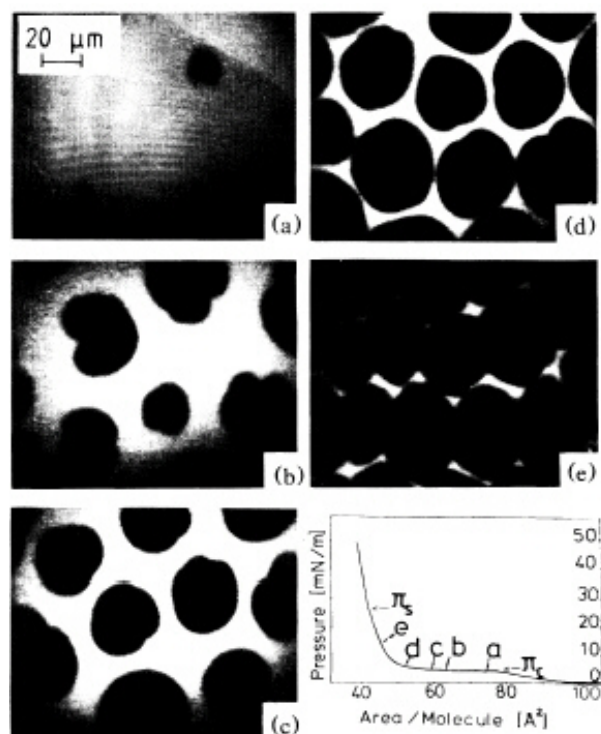


Figure 8.2.1: This figure was taken from a paper by Kjaer et al. [106]. It shows the isotherm and the corresponding fluorescence images of a dimyristoylphosphatidic acid (DMPA) monolayer at pH 5.5, 19°C. The discontinuity in the slope indicates a first order phase transition while the non-horizontal plateau of two phase coexistence pressure violates Gibbs' phase rule.

μ_{ij} . One should expect deviations from Gibbs' phase rule if long range interactions become important. Further the phases are assumed to be extended. I.e. no entropy contributions occur because of the mixing of the phases and all interfaces are unbended. The equations of mechanical equilibrium gain more degrees of freedom if also curved surfaces are considered. In macroscopic systems with the phases forming large volumina the effect of curved interfaces is very small, but in colloidal systems with structures on mesoscopic scales the curvature of the interfaces enters the equations as another degree of freedom [105].

8.2 Violations of Gibbs' phase rule observed in monolayers

Pressure-area isotherms in Langmuir monolayers exhibit a non-horizontal slope of the two phase coexistence pressure and violate Gibbs' phase rule. As an example in figure 8.2.1 the $\pi - A$ -isotherm of DMPA is shown. The figure was taken from [106]. The isotherm exhibits a discontinuity at $\alpha_k \approx 78 \text{ \AA}^2$ which indicates a first order phase transition. The fluorescence images show that two phases coexist over wide pressure range and the isotherm

in the coexistence region has a finite slope of at least $0.15 \text{ mN/m per } \text{\AA}^2$. This fact is in contradiction to the Gibbs' phase rule (8.1.1), which restricts two phase coexistence in a one component system at a given temperature to a single pressure. The non-horizontal slope of the isotherm at two phase coexistence is well reproducible and often reported in the literature. Another phenomenon apparently violating Gibbs' phase rule is the observation of an extended three phase coexistence region instead of a triple point. In figure 8.2.2 the temperature-molecular area phase diagram of MOD monolayer is plotted. MOD with 1% fluorescence dye was spread on pure water and observed using fluorescence microscopy. The phases were identified by eye inspection [107]. The phases G, LE and LC coexist over a temperature range of around 15 K. The phase coexistence regions violate Gibbs' phase rule (8.1.1) which predicts a triple-point and two phase coexistence only along *lines* within this diagram.

In older literature both effects are accounted to impurities [108–110]. The good reproducibility of the isotherms, however, point toward a 'real' effect induced by special features of the observed system. So several papers occurred in the recent years claiming to identify the cause for the apparent violation of Gibbs' phase rule. Israelachvili [111] and Fainerman and Vollhardt [112–114] presented theories based on the formation of large clusters ideally mixing with monomers. Ruckenstein and Li [115] found a phase-transition-like behaviour for the ideal mixing of large clusters. They explained the non-horizontal shape of the isotherm as an effect of non-ideal mixing (generalized Flory-Huggins-mixing) of the large clusters (=domains) with the monomers (or free spaces in a Flory-lattice). An estimation of the effect of the dipole interaction has been done by Möhwald [116] with the result that the effect of the long range interaction is too small. Nevertheless, later Ruckenstein [117] suggests the dipole long range interaction to cause the searched deviation from ideality. Unfortunately the presented theory

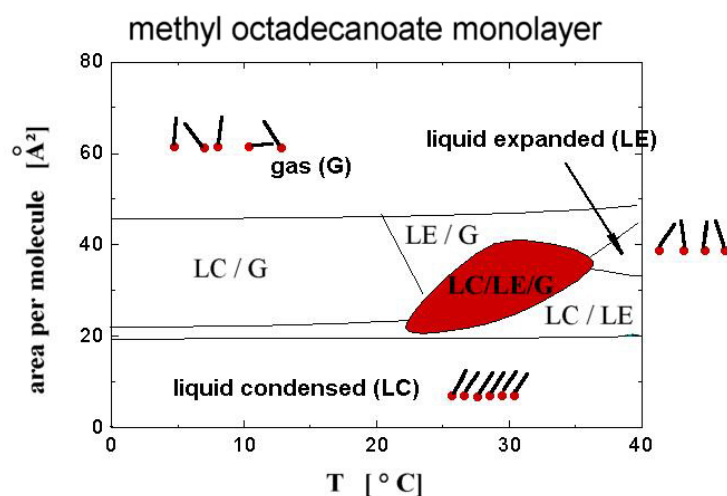


Figure 8.2.2: Phase diagram of MOD monolayer. The phase coexistence regions violate Gibbs' phase rule.

does not make any predictions comparable to experimental results. Kaganer already reported on strain-mediated phases [118] in other systems. In this section the influence of the long range interaction, the mixing of clusters or impurities and curved interfaces will be studied.

8.3 Influence of electrostatics

8.3.1 Dipole pressure contribution in isotherm

The effect of the dipole interaction will be roughly estimated. The surface pressure is given as the derivative of the free energy with respect to the total area:

$$\pi = -\frac{\partial F}{\partial A}, \quad (8.3.1)$$

Let us consider a simplified model: a one phase system with the surface potential parameter μ . The dielectric contribution is given by

$$F_{\text{el.}} = \frac{1}{2} \int_{\text{trough}} \int_{\text{trough}} \frac{\mu^2}{\rho^3} dA dA'. \quad (8.3.2)$$

Plugging (8.3.2) into equation (8.3.1) yields the dipole pressure contribution

$$\pi_{\text{el}} = \int_{\text{trough}} \frac{\mu^2}{\rho^3} dA' = \frac{2\pi\mu^2}{\Delta}. \quad (8.3.3)$$

Note that the same result is obtained by application of equation (4.2.2). In order to estimate an upper limit of the dipole contribution to the total pressure a surface potential change of 0.5 V and a van-der-Waals cut-off length $\Delta = 5 \text{ nm}^2$ are plugged in. The result is 0.4 mN/m, much smaller than the observed pressure change. The isotherm slope in the coexistence region could only be explained with the dipole interaction if the cut-off-length is $\Delta \approx 1 \text{ \AA}$. In the expected range of Δ between nm and μm the effect of the electrostatics is small. Moehwald published an approximation with the same result [116].

8.3.2 Electrostatics smears triple point

In the previous section it has been shown that the non-horizontal shape of the isotherm can probably not be explained by the presence of the dipolar long range interaction since the electrostatic pressure is too small. Now the effect of long range interaction on the three phase coexistence will be studied.

²The $\Delta \approx 0.1 \mu\text{m}$ determined in section 6.2.4 is a property of the interface. Here we have to guess the cut-off length in the bulk.

The hypothesis is the following: In a system without long range interaction (=undisturbed) with phase transitions between the three phases (LC, LE and G) one triple point exists (α_{triple} , π_{triple}) and two phase coexistence occurs on (one-dimensional) lines. In the presence of long range interactions the pressure is not an intensive quantity but depends on the system geometry and is different in each point. This leads to a broadening of the two-phase coexistence lines and the triple point to coexistence regions.

The slope of the two phase coexistence line of the phases i and j is given by the Clausius-Clapeyron equation:

$$\frac{d\pi_{ij}}{dT} = \frac{\xi_{ij}}{(\alpha_j - \alpha_i)T}, \quad (8.3.4)$$

where ξ_{ij} is the latent heat per molecule of the transition from phase i to phase j and $\alpha_j - \alpha_i$ is the change of molecular area during the transition. For monolayers direct measurement of the latent heat by calorimetry is problematic since the total amount of heat is very small in the monolayer compared to the bulk. However, the latent heat can be estimated out of the line tension, as suggested by Laplace (in 3D systems) and Muller and Gallet [31] (in Langmuir monolayers). In this picture the interfacial tension is a result of the energy loss of a particle on the interface with n_{int} neighbours compared to a particle in the bulk with $n_{\text{bulk}} > n_{\text{int}}$. In the model of Laplace, or rather Muller and Gallet, the interfacial tension is exactly the energy loss per interface occupied by the particle. Better consistency with experimental results, however, is obtained by models taking the entropy change into account as well [119]. For 2D and the simpler theory one finds the estimation

$$K\lambda_{ij} = \frac{\xi_j}{\sqrt{\alpha_j}} - \frac{\xi_i}{\sqrt{\alpha_i}}, \quad (8.3.5)$$

where K is the Laplace ratio and contains information about the number of the interacting neighbours in the bulk and on the interface. The quantities ξ_i and ξ_j are molecular bulk energies and the latent heat is their difference

$$\xi_{ij} = \xi_j - \xi_i. \quad (8.3.6)$$

The bulk energy of gaseous phase is approximated by 0

$$\xi_G = 0. \quad (8.3.7)$$

Now the phase diagram for the 'unperturbed' system can be estimated. The line tensions between the phases are known for MOD from 2D pendant drop experiments described in chapter 4 (or [54]) and from experiments by Wurlitzer et al. [35, 36]. The Laplace ratio is expected to have a value between 2 and 3, for the calculation it is set to $K = 3$ in order to obtain an upper limit. A calculated phase diagram is shown in figure 8.3.1 (solid lines).

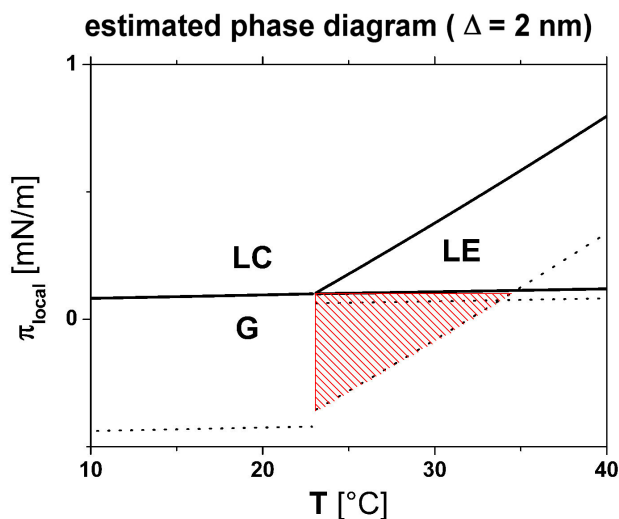


Figure 8.3.1: estimated local pressure-temperature phase diagram using material parameters of MOD. Solid lines: unperturbed. Dotted lines: pressure variation due to dipole interaction. The cut-off length Δ was chosen in a way to obtain the phase coexistence region within a temperature range corresponding to the experiments presented in figure 8.2.2.

In figure 8.3.1 also the electrostatic perturbation is plotted (dotted lines). The electrostatic pressure has been calculated using (4.2.2) for planes consisting of one phase only. The so calculated electrostatic pressure represents an upper limit for the real effect.

$$\pi_{\text{el,max}} = \frac{2\pi}{\Delta}(\mu_i^2 - \mu_j^2) \quad (8.3.8)$$

The size of the three phase coexistence region is very sensitive to the cut-off-length Δ . The smaller the scaling parameter Δ the bigger is the effect of the long range interaction. The phase behaviour is not invariant with respect to the shape invariant scaling transformation (4.3.1). Setting $\Delta = 0.1 \mu\text{m}$ as determined in subsection 6.2.4 yields a three phase coexistence region within a temperature range of $\approx 0.2\text{K}$. Only a Δ smaller than 2 nm (plotted in figure 8.3.1) could explain the extended coexistence region within this theory. We conclude that the extended three phase coexistence could be due to long range interactions, but the contributions of this dipole interactions are very small.

8.4 Finite size effects become important on nm scale

8.4.1 Mixing entropy due to cluster formation

ideal mixing At phase coexistence in Langmuir monolayers mesoscopic patterns are formed. Contributions from the entropy of the mixing of these phases in general signify an increase of the probability of phase coexistence and enlarge the region of phase coexistence. The system

can be modeled as a chemical reaction of monomers to clusters, each domain representing one cluster. Let all clusters have the same size.



Domains visualized using fluorescence or Brewster angle microscopy have a diameter from $\approx 10 \mu\text{m}$ up to $\approx 1000 \mu\text{m}$, i.e. aggregation numbers n ranging from 10^8 to 10^{12} . For this chemical reaction the mass action law holds

$$\frac{C_{\mathbf{A}_n}}{C_{\mathbf{A}}^n} = K. \quad (8.4.2)$$

Let the system be a mixture of monomers and clusters in chemical equilibrium. Both components are assumed to be ideal gases. The total pressure is the sum of the two partial pressures related to one another via the mass action law (8.4.2). In figure 8.4.1 the pressure versus the molecular area in arbitrary units for different cluster sizes are plotted. The shape of the isotherm strongly depends on the aggregation number n . If n is small (≈ 3) the behaviour differs slightly from a one-component ideal gas. There is no discontinuity in slope or plateau-region in the isotherm. If the aggregation number is increased up to ≈ 100 then a plateau with non-horizontal shape and a 'discontinuity' in the slope of the isotherm occur. At large $n \gg 100$ the plateau of the isotherm is horizontal. Israelachvili [111] published a similar approach and found the same results.

In contradiction to that Fainerman et. al. [112, 114, 120] predicted an indirect proportional behaviour of the pressure with respect to the molecular area in the two phase coexistence region especially for large $n > 1000$. Most probably this is an artifact of their approximation

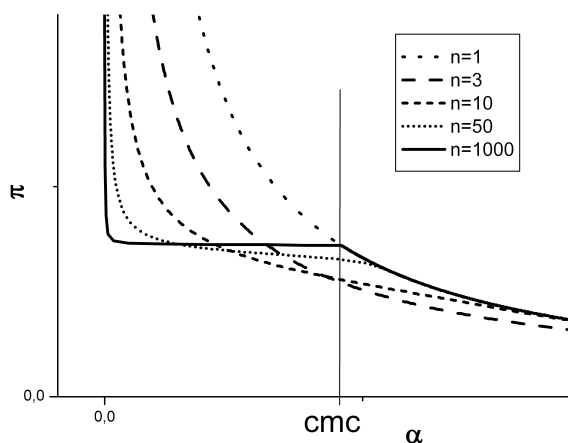


Figure 8.4.1: Calculated surface pressure - molecular area isotherms in arbitrary units for a monomer-cluster reaction. For large aggregation numbers $n > 1000$ the isotherm exhibits a discontinuity and a flat plateau.

³. Nevertheless, the empirical isotherms are well described by an indirect proportionality to the molecular area $\pi \propto 1/\alpha$.

The experimental isotherms (figure 8.2.1) agree very well to the $n \approx 100$ isotherms. Could a demixing transition of $n = 100$ -clusters to the mesoscopic domains explain the shape of the isotherms? The answer is no. Plugging two components (monomers, $n = 100$ -clusters) and two phases (LE = monomer rich, LC = cluster rich) into the Gibbs' phase rule yields two degrees of freedom. The equation for chemical equilibrium between clusters and monomers (8.4.2) reduces the degrees of freedom by one. So the isotherm-plateau of such a system is horizontal. Clusters ideally mixing with monomers strictly follow Gibbs' phase rule and do not explain the non-horizontal shape of the isotherm-plateau.

non-ideal mixing described by generalized Flory-Huggins equation Ruckenstein and coworkers published a paper taking non-ideal mixing of large clusters (domains) into account [115]. Dipole interaction enters the equations in the equilibrium size of the formed domains using the equation of McConnell (3.4.2). The van-der-Waals interaction is represented by some kind of latent heat. In the limit of ideal mixing they found that the formation of the domains with the equilibrium size is phase-transition-like and agrees with the calculations presented in the previous paragraph. In the theory of Ruckenstein and Li the non-horizontal plateau of the isotherm is explained as an effect of the non-ideal mixing of the domains within the monomers.

Flory and Huggins found that the entropy of mixing of long chain-like molecules is larger than the mixing entropy of hard spheres. The Flory-Huggins mixing entropy provides an upper limit for this entropy of mixing. The Flory-Huggins entropy for monolayers is

$$S = -k \sum_i \ln \Phi_i, \quad (8.4.3)$$

with summation over all species (phases) i and the area fraction Φ_i . The entropy arises due to the number of micro states N realizing the macroscopic state.

$$S = k \ln N \quad (8.4.4)$$

For rigid circular particles the micro states are realized just by different positions of the center of mass of the particles. The mixing is almost ideal. For long flexible chains many conformations for the particle exist and therefore much more micro states realize one macro

³The author suspects that Fainerman et al. made a mistake in the mathematics in [112], affecting all following papers. Equation (11) is obtained by approximating equation (10) (by the way, the approximation does not hold for large aggregation numbers). Then equation (11) is plugged directly in (10), i.e. a circle conclusion. The result is an artifact of the approximation. Without the approximation one would get an equation like $0 = 0$.

state. Flory and Huggins modeled this mixing as the mixing of area elements of the molecules with the free sites of a so called Flory-lattice. The ideal mixing of each chain-segment of the molecule in the total volume provides an upper limit for the entropy, where one chain segment has the size of a Flory-lattice free site. That's why the area fraction is taken in the Flory-Huggins equation but the particle number concentration is not.

So the mixing entropy of real mixtures lies between the mixing entropy of ideal mixing and the Flory-Huggins mixing entropy $S_{\text{ideal}} < S < S_{\text{FH}}$. To express this fact Donohue and Prausnitz [121] constructed a generalized Flory-Huggins equation

$$S = -k \sum_i N_i \ln \frac{\Phi_i \gamma_i^{p_i-1}}{\sum_j \Phi_j \gamma_j^{p_j-1}} \quad (8.4.5)$$

where N_i is the number of particles of species i , γ_i the number of Flory-lattice free sites occupied by one particle of species i and p_i the parameter describing the unideality of the mixing. For $p = 0$ the ideal mixing entropy is obtained and for $p = 1$ the Flory-Huggins mixing entropy is obtained.

Ruckenstein et al. fitted isotherms with the entropy given by equation 8.4.5 and determined the exponents p for several shapes. They found best agreement for a value of $p = 0.93$ - i.e. almost the Flory-Huggins mixing.

Let us try to calculate the exponent p . Since the observed domains are almost circular additional entropy can occur only due to variation in the cluster size. In appendix A.9 the equation of state is calculated considering the entropy of cluster size. One finds that the reaction is described by the mass action law with reaction constant K'

$$\frac{C_c}{C_g^{\langle n \rangle}} = K'(\epsilon, \langle n \rangle), \quad (8.4.6)$$

i.e. $p = 0$. So the behaviour for large aggregation numbers n is the same as for the ideal mixing system discussed in the previous paragraph. Physically it seems to be not justified to apply the Flory-Huggins entropy to this system.

8.4.2 Curved interfaces stabilize particles smaller than 1 nm

If an interface is plane the pressure in both phases is the same in mechanical equilibrium. For curved interfaces the Young-Laplace-equation (4.2.1) describes the mechanical equilibrium of an interface. In general the Laplace pressure inside a droplet is larger than outside and the droplet might be stabilized even if the outside pressure is below the phase transition pressure. Plugging in some example values can show the order of magnitude of the effect: In order to obtain a pressure of more than 1 mN/m inside a domain with the line tension 1 pN, the domain radius has to be smaller than 1 nm. So finite size effects do not cause the apparent violation of Gibbs' phase rule.

8.5 Impurity could explain the apparent violation of Gibbs' phase rule

The classical explanation for the non-Gibbsian behaviour of the Langmuir-monolayers is the presence of impurities. In fact it seems to be a killing argument explaining everything and nothing. Since all other approaches give no convincing answer, we would like to add this section and present arguments and estimations about impurity effects.

Phases in systems consisting of one component and impurities are mixtures. The properties of these phases depend on their composition. There are some experimental data pointing toward this mixture hypothesis: Wurlitzer et. al. [38] found that gas-bubbles in dry foams are bigger than expected (using the electrostatic theory with constant line tensions and surface potentials presented in chapter 3) and suggests interpreting the result as an *increase* in the line tension by *decreasing* LE fraction. Further circular LC-domains in gas or LE are smaller than the predicted radius calculated in section 5.2. Fluorescence images of both processes are shown in figure 8.5.1, the latter of which points toward *decreasing* line tension by *increasing* the amount of the denser phase. A mixture of two components could explain the effect. The composition of the phases changes on changing the area fraction. Increasing the area fraction of the denser phase increases the relative amount of impurity within the phase and leads to a decrease of the line tension.

Another indication is the following: Khattari observed a shape instability of an LE-domain confined in a gas hole in LC in MOD monolayer. The instability occurred on compression, i.e. on decreasing the size of the gas hole. The common electrostatic and hydrodynamic theory does not explain this phenomenon [48]. According to the results of the 2D foam simulations and calculations for the wetting droplets a confinement is expected to stabilize the droplet. If impurities are present, the phenomenon could be interpreted as a mixing transition. Mixing transitions of cholesterol-rich and cholesterol-poor phases were extensively studied by Radhakrishnan et al. [122–124]. In figure 8.5.2 the corresponding fluorescence images are shown. Both are monolayer observations on compression. The experimental observations show a big similarity.

The impurity theory is also supported by the work of Priester et al. [125]. They could experimentally show that normally Gibbs' monolayers are polluted and that the impurity has big effects on the thermodynamic behaviour of the monolayer. So trace impurities cause a linear shape of the surface pressure-concentration isotherm in Gibbs' monolayers. The isotherms became non-linear after application of a purification procedure [126]. The purification is done by sucking the monolayer from the interface and remove surface active impurities in this way. Melzer et. al reported on similarities between the surface concentration-surface pressure isotherms in (unpurified) Gibbs' and Langmuir monolayers [127]. Both isotherms exhibit a

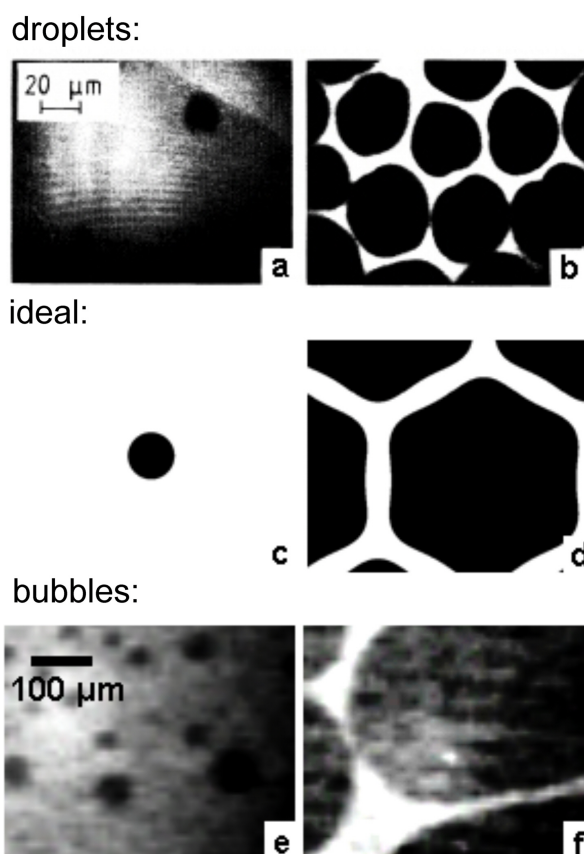


Figure 8.5.1: (a) and (b): LC-domains in LE-matrix of a dimyristoylphosphatidic acid monolayer at 19 °C taken from [106]. (a) shows an isolated domain and (b) the structure at an area fraction of LC of about $\Phi = 0.77$.

(c) and (d): theoretical calculated structure assuming constant line tensions (see section 5.2). (c) $\Phi \approx 0$ (d) $\Phi = 0.77$

(e) and (f): gas bubbles in LE-matrix of MOD monolayer at 20 °C taken from [38]. (e) low area fraction (f) fraction of gas phase $\Phi = 0.8$

The LC-domains are smaller than the theoretical predicted size, the gas bubbles bigger. Both observations point toward a decrease of the line tension of the denser phase on increasing its area fraction. Or: compression lowers the line tension.

plateau region with a non-horizontal shape. So it might be possible to check the influence of the impurity on the isotherm using a purified Gibbs' monolayer. Pallas and Pethica [108] used very pure substances and measured the isotherm of Langmuir monolayers. Within the error their data is compatible to a horizontal isotherm within two phase coexistence. Experiments by Miller and Möhwald [109] showed that the adding of 1-3% impurities has indeed an effect large enough in order to explain experimental data.

Let us estimate the order of magnitude of the expected effect in an ideal system. Consider a one component monolayer with the area concentration of surfactants α with a small amount of

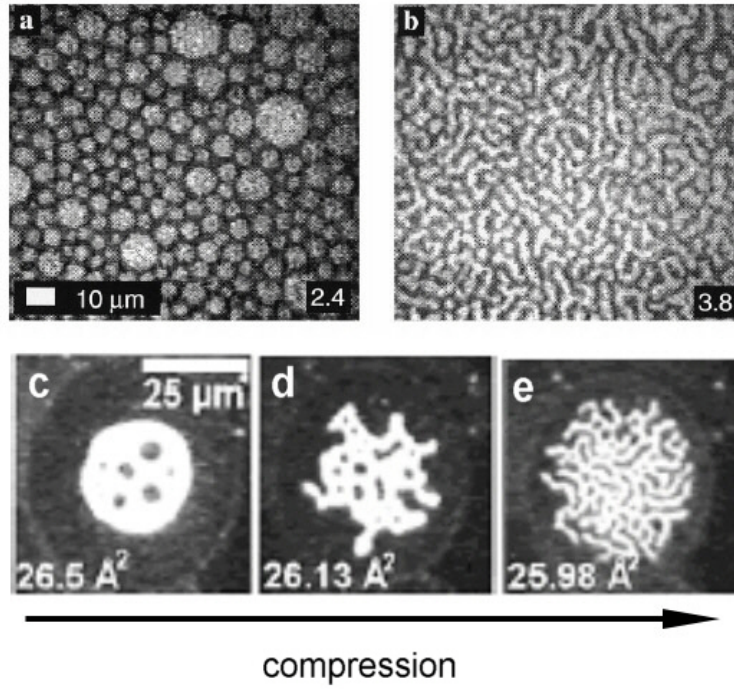


Figure 8.5.2: (a) and (b) are taken from [122]. They show fluorescence images of a monolayer consisting of a Dicholesterol/phospholipid mixture. (1:3) On compression (pressure increase from 2.4 mN/m to 3.8 mN/m) the topology changes from a emulsion (circular domains in matrix phase) to a stripe phase with a strong decrease of the characteristic length scale of the patterns. Radhakrishnan and McConnell interpret the phenomenon as an effect of mixing leading finally to a miscibility transition.

(c), (d) and (e) are fluorescence images of MOD monolayer taken from [48]. Khattari and Fischer could show that the shape instability can't be explained within the 'classical' theory (homogeneous phases, constant line tension and surface potentials). The similarity to the above observation points toward an effect of mixing.

a second component, the impurity with an area concentration $\alpha^* = c^*\alpha$. The pure monolayer exhibits a gas/liquid phase transition at a surface pressure π_0 , the molecules in the liquid have the constant molecular area α_1 . The total pressure π_{total} of the gaseous phase then is the sum of the partial pressures of substance π and impurity π^* . The liquid phase is assumed as a mixture with the fraction of substance Φ_1 and $1 - \Phi_1$ impurity. According to Raoult's and Henry's law the partial vapor pressures are directly proportional to the fraction in the solution:

$$\pi = \Phi_1 \pi_0 \quad (8.5.1)$$

$$\pi^* = (1 - \Phi_1) \pi_0^* \quad (8.5.2)$$

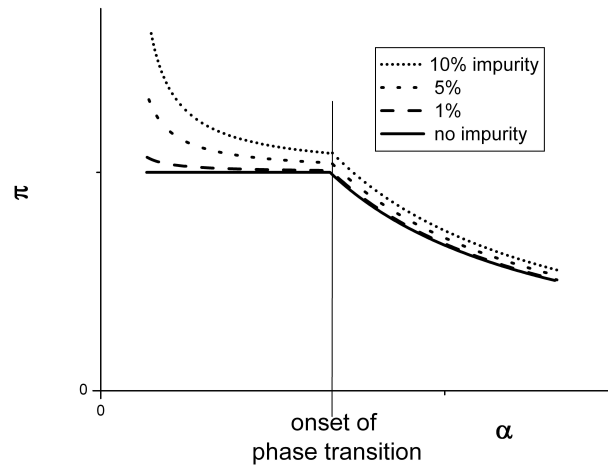


Figure 8.5.3: Calculated isotherms with 0%, 1%, 5% and 10% impurity in arbitrary units. The coefficient π_0^* defined in equation (8.5.1) has been chosen $\pi_0^* = 8\pi_0$ and the density of the liquid phase $\alpha_1 = \frac{1}{5\pi_0}$. Compared to the experimental isotherm in figure 8.2.1 the effect even for larger amounts of impurity is quite small.

The balance equation for the number of molecules is:

$$c^* = \frac{\alpha_1 \pi^* \Phi + (1 - \Phi_1)(1 - \Phi)}{\alpha_1 \pi \Phi + \Phi_1(1 - \Phi)} \quad (8.5.3)$$

with the area fraction of the phases Φ . Plugging the pressures (8.5.1) into this equations, Φ_1 can be eliminated and one can formulate equations for the molecular area and the total pressure (appendix A.10)

$$\pi_{\text{total}} = \pi_{\text{total}}(c^*, \pi_0, \pi_0^*, \alpha_1, \Phi) \quad (8.5.4)$$

$$\alpha = \alpha(c^*, \pi_0, \pi_0^*, \alpha_1, \Phi) \quad (8.5.5)$$

Figure 8.5.3 shows some isotherms calculated using equations (8.5.4). The parameter Φ (area fraction of the phases) was varied between 0 and 1, note that equations (8.5.4) describe only the plateau region. Comparison with experimental isotherms points toward impurity amounts larger than 5%, if, off course, the behaviour of the substance/impurity mixture is almost ideal. Experiments by Miller and Möhwald [109] found already effects of this magnitude with only 1-3% impurity.

8.6 Summary

Neither the electrostatics nor finite size effects as entropy of mixing or curvature can explain the apparent violation of Gibbs' phase rule in the non-horizontal slope of the isotherm in many

Langmuir monolayers or the extended three phase coexistence region in MOD monolayer. Impurity could explain the isotherm slope. The dependence of the line tension on the area fraction is an experimental evidence supporting the impurity hypothesis.

Chapter 9

Summary

The pattern formation and equilibrium structure of liquid Langmuir monolayer domains were investigated theoretically and experimentally. Langmuir monolayers are isolated 2D systems of amphiphiles on the air/water interfaces exhibiting 2D crystalline, liquid crystalline, liquid and gaseous phases. The asymmetric arrangement of the molecules, with their hydrophilic head groups immersed into the aqueous phase, gives rise to permanent electric dipole moments that are not completely screened and result in a long range dipole repulsion. This long-range interaction and the two-dimensionality lend these systems most interesting features. The geometry of liquid domains is determined by the long-range dipole interaction and was optically measured. The common interaction model is presented taking into account attractive short range interactions (represented by the *bare* line tensions) and long range dipole interaction $\propto 1/r^3$ (represented by surface potentials). The separating length between short and long range interactions is described by a scale parameter Δ . The interaction model has been consequently applied to describe the drying of 2D foams and the shapes and contact angles of 2D wetting droplets quantitatively.

Using the interaction model conditions for local thermodynamic equilibrium were derived within this work: The shape of an interface line is described by a 2D analogue to the Young-Laplace equation including a dipole pressure term. The contact angle is a materials parameter described by Young's equation and determined by the bare line tensions.

It has been shown that the Young-Laplace equation is invariant to a transformation of the bare line tensions with respect to the scale parameter Δ . This fact has been used in order to measure the line tension of 2D pendant droplets in methyl octadecanoate by application of the Young-Laplace equation to their shape (pendant droplet tensiometry).

Further the Young-Laplace equation has been solved numerically in order to predict the shape of bubbles of a 2D dipolar foam. The competition between long range and short range interactions leads to the formation of mesoscopic patterns on a well defined length scale. It has been found within the present work that the bubble shapes in a metastable thermodynamic

equilibrium of an ideal foam are universal, i.e. they depend only on the area fraction of the phases and not on any materials parameter. The size of the bubbles is described by a universal size function and the equilibrium size of an isolated domain. The latter is the only materials parameter needed to describe ideal 2D foams. Experimental 2D foams observed in Langmuir monolayers are in general polydisperse and far away from ideality. The onset of bubble deformation upon drying the foam (from diluted emulsion with circular bubbles to dry foams with hexagonal bubbles) has been compared with the ideal foam. Significant deformations occur in both systems at $\approx 70\%$ area fraction of the bubble phase. The ideal and the polydisperse dipolar foam dry at lower area fraction than short range interaction foams (91% and 84% respectively).

In three phase coexistence regions besides the shapes of the droplets the topology of the phases depends on the electrostatic interactions as well. Consequently the equilibrium thermodynamics of 2D wetting has been studied. It is shown that contact angles are not invariant to shape invariant scale transformation. The contact angle of experimental wetting droplets were determined on a well defined scale Δ by fitting the droplets with numerical solutions of the Young-Laplace equation. The experiments approved Young's equation (in methyl octadecanoate monolayer).

It has been found that the restriction of the contact angle to values between 0 and 2π provides a lower limit for the scale parameter Δ of $\approx 0.1 \mu\text{m}$. The parameter Δ was measured for the first time. In literature it was interpreted as a lattice constant of the dipole lattice or the range of van-der-Waals interactions. The present work shows that this interpretations do not hold and an interpretation of Δ as a dipole correlation or healing length on the interface line is suggested.

Theory and experiment of droplet shape bifurcations of wetting droplets are presented. The competition between long and short range interactions lead to shape bifurcations of isolated domains. A variational approach restricting the shape of wetting droplets to circular segments predicts shape bifurcations when the droplet carries the highest dipole density of the three coexisting phases. In general the presence of the substrate has a stabilizing effect on wetting droplets.

Studies on the relevance of the wetting results for biological systems showed that the control of the wetting mode may play a role in biological membranes. In our group the membrane has been modelled experimentally by a Langmuir monolayer containing phospholipids and the wetting behaviour of different 2D liquids has been observed during an enzymatic hydrolysis of the phospholipid. Experiments performed by Khattari, Fischer and Ruschel did not exhibit a change in the wetting mode but a change in the occurrence of partial wetting and dewetted domains.

Finally, possible explanations for the apparent violation of Gibbs' phase rule in Langmuir

monolayers were studied. The nonhorizontal plateau of the surface pressure-molecular area isotherm in the phase coexistence region is a well reproduced feature of Langmuir monolayers and in contradiction to Gibbs' phase rule. Also the extended three phase coexistence region observed for instance in methyl octadecanoate monolayers violates Gibbs' phase rule. A quantitative analysis of finite size effects (entropy effects, curved interfaces) revealed that these effects are too small and play a role only for nm sized particles. Also, the effect of the electrostatics treated as a perturbation ideal system is too small by two orders of magnitude. Impurities could explain the isotherm as well as the extended three phase coexistence region. Several evidences are presented supporting the impurity hypothesis.

In summary, the present work shows that the theory based on a competition of short and long range interactions is suitable in order to describe a wide field of phenomena, such as shapes, topology of phases coexisting in Langmuir monolayers and it may possibly be extended to systems such as ferrofluids or biological membranes. There it might also have technical applications such as the control of specific signal cascades across the membrane via the membrane potential.

Appendix A

A.1 Relative potentials

Let $\Psi_{i,j}(|\mathbf{r}_i - \mathbf{r}_j|)$ be a general pair interaction between area elements of the phases i and j and $U_i(\mathbf{r}_i)$ an external potential. The interaction energy of the potentials depend on the interacting phases i and j . The free energy is

$$F_{PU} = \frac{1}{2} \sum_i \int_{A_i} \sum_j \int_{A_j} \Psi_{i,j} dA_i dA_j + \sum_i \int_{A_i} U_i dA_i. \quad (\text{A.1.1})$$

The aim is to find a transformation $\Psi_{i,j} \rightarrow \hat{\Psi}_{i,j}$, $U_i \rightarrow \hat{U}_i$ with $\hat{\Psi}_{1,i} = 0$, $\hat{U}_1 = 0$ for all i leaving the shape dependent terms invariant. Allowed transformations are:

- add to the free energy

$$+ \sum_{i,j} \int_{A_i} \int_{A_j} P_{k,l} dA_i dA_j \quad (\text{A.1.2})$$

with fixed k and l . This term depends only on the total area of the monolayer.

- add to the free energy

$$+ \int_{A_i} \sum_j \int_{A_j} P_{i,k} dA_i dA_j \quad (\text{A.1.3})$$

with fixed k . This term just depends on the area of the individual phases.

- add to the free energy the shape independent term

$$+ \sum_i \int_{A_i} U_k dA_i. \quad (\text{A.1.4})$$

One finds that

$$\hat{\Psi}_{i,j} = \Psi_{i,j} - \Psi_{i,1} \quad (\text{A.1.5})$$

(rule (A.1.3) applied for each phase i) and

$$\hat{U}_i = U_i - U_1 \quad (\text{A.1.6})$$

(rule (A.1.4)) fulfil don't change the shape dependent terms in (A.1.1).

A symmetrical transformation is

$$\hat{\Psi}_{i,j} = \Psi_{i,j} - \Psi_{i,1} - \Psi_{1,j} + \Psi_{1,1} \quad (\text{A.1.7})$$

(using rule (A.1.2) and (A.1.3)). Using this transformation for the dipole interaction transforms $\mu_i \rightarrow \mu_{i1}$, with $\mu_{ij} = \mu_i - \mu_j$. Since $\mu_{ii} = 0$ the dipole density of one phase can be chosen as a reference potential with vanishing contribution from this phase.

A.2 Variation problem

A.2.1 Young-Laplace equation

Let the free energy F in a 2D system have the form

$$F = \frac{1}{2} \sum_{i,j} \left(\lambda_{ij} \int_{\{ij\}} ds_{ij} + \int_i \int_j \Psi_{ij}(|\mathbf{r}_i - \mathbf{r}_j|) dA_i dA_j \right) + \sum_i \int_i U_i(\mathbf{r}_i) dA_i, \quad (\text{A.2.1})$$

i.e. the sum of the line energy proportional to the length of the interface lines between the phases i and j , self interaction energy described by the pair interaction potential Ψ_{ij} and the energy of phase i in an external potential U_i . The summation is performed over all phases i and j .

Further assume a mirror symmetrical droplet (phase 1) $y = \pm y(x)$ attached to a (long enough) straight solid interface ($x = 0$) (substrate phase 2 extended to $x < 0$) with the contact points $\pm y(0)$ and the height h , $y(h) = 0$. Using (A.1.5) and (A.1.6) the contribution of the matrix phase 3 is set to 0. In thermodynamical equilibrium the droplet free energy (summation over domains i)

$$\begin{aligned} F_{\text{drop}} &= 2 \int_0^h dx_1 ((\lambda_{23} - \lambda_{12})y') + 2 \int_0^h dx_1 \left(\lambda_{13} \sqrt{1 + y'^2} \right) \\ &+ \int_0^h dx_1 \int_{-y(x_1)}^{y(x_1)} dy_1 \sum_{i \neq \text{drop}} \int_{A_i} dA_i (\Psi_{1,i}(|\mathbf{r}_{\text{drop}} - \mathbf{r}_i|) - \Psi_{1,3}(|\mathbf{r}_{\text{drop}} - \mathbf{r}_i|)) \\ &+ \frac{1}{2} \int_0^h dx_1 \int_{-y(x_1)}^{y(x_1)} dy_1 \int_0^h dx_2 \int_{-y(x_2)}^{y(x_2)} dy_2 (\Psi_{1,1}(|\mathbf{r}_1 - \mathbf{r}_2|) - \Psi_{1,3}(|\mathbf{r}_1 - \mathbf{r}_2|)) \\ &+ \int_0^h dx_1 \int_{-y(x_1)}^{y(x_1)} dy_1 (U_1(\mathbf{r}_1) - U_3(\mathbf{r}_1)) \end{aligned} \quad (\text{A.2.2})$$

is a minimum. This is a minimization problem with moveable contact point under the constraint of constant area

$$A = 2 \int_0^h dx_1 y(x_1). \quad (\text{A.2.3})$$

The solutions fulfil the Euler-Lagrange equation for the shape

$$\frac{\partial \hat{F}}{\partial y} - \frac{d}{dx} \frac{\partial \hat{F}}{\partial y'} = 0 \quad (\text{A.2.4})$$

and for the contact point

$$\left. \frac{\partial \hat{F}}{\partial y'} \right|_{x=0} = 0, \quad (\text{A.2.5})$$

with

$$\begin{aligned} \hat{F} &= 2(\lambda_{23} - \lambda_{12})y' + 2\lambda_{13}\sqrt{1+y'^2} \\ &+ \int_{-y(x_1)}^{y(x_1)} dy_1 \sum_{i \neq \text{drop}} \int_{A_i} dA_i (\Psi_{1,i}(|\mathbf{r}_{\text{drop}} - \mathbf{r}_i|) - \Psi_{1,3}(|\mathbf{r}_{\text{drop}} - \mathbf{r}_i|)) \\ &+ \frac{1}{2} \int_{-y(x_1)}^{y(x_1)} dy_1 \int_0^h dx_2 \int_{-y(x_2)}^{y(x_2)} dy_2 (\Psi_{1,1}(|\mathbf{r}_1 - \mathbf{r}_2|) - \Psi_{1,3}(|\mathbf{r}_1 - \mathbf{r}_2|)) \\ &+ \int_{-y(x_1)}^{y(x_1)} dy_1 (U_1(\mathbf{r}_1) - U_3(\mathbf{r}_1)) + 2p_{13}y(x_1), \end{aligned} \quad (\text{A.2.6})$$

with the Lagrange parameter p_{13} . The individual derivatives are

$$\begin{aligned} \frac{\partial \hat{F}}{\partial y} &= 2 \left(\sum_{i \neq \text{drop}} \int_{A_i} dA_i (\Psi_{1,i}(|\mathbf{r}_{\text{drop}} - \mathbf{r}_i|) - \Psi_{1,3}(|\mathbf{r}_{\text{drop}} - \mathbf{r}_i|)) \right. \\ &\quad \left. + \int_0^h dx_2 \int_{-y(x_2)}^{y(x_2)} dy_2 (\Psi_{1,1}(|\mathbf{r}_1 - \mathbf{r}_2|) - \Psi_{1,3}(|\mathbf{r}_1 - \mathbf{r}_2|)) + U_1(\mathbf{r}_1) - U_3(\mathbf{r}_1) + p_{13} \right) \\ \frac{\partial \hat{F}}{\partial y'} &= 2 \left(\lambda_{23} - \lambda_{12} + \lambda_{13} \frac{y'}{\sqrt{1+y'^2}} \right) \\ \frac{d}{dx} \frac{\partial \hat{F}}{\partial y'} &= 2\lambda_{13} \frac{y''}{\sqrt{1+y'^2}^3} = -2\lambda_{13}\kappa(x) \end{aligned} \quad (\text{A.2.7})$$

Formulating the Euler-Lagrange equation and collecting all the terms yields the general Young-Laplace equation

$$\lambda_{ij}\kappa_{ij}(\mathbf{r}) = p_{ij} - \sum_k \int_{A_k} \left((\Psi_{i,k}(|\mathbf{r}_{ij} - \mathbf{r}_k|) - \Psi_{j,k}(|\mathbf{r}_{ij} - \mathbf{r}_k|)) \right) dA_k - (U_i - U_j) \quad (\text{A.2.8})$$

Setting $U_i = 0$ and $\Psi_{i,j}(|\mathbf{r}_i - \mathbf{r}_j|) = \mu_i \mu_j / (|\mathbf{r}_i - \mathbf{r}_j|^2 + \Delta^2)^{3/2}$ yields the Young-Laplace equation with dipolar interaction (4.2.1).

A.2.2 Young's equation

Plugging (A.2.7) in (A.2.5) directly yields the stability criteria for the contact point. Note that the potentials Ψ and U don't occur in this equation.

$$\begin{aligned} \left(\lambda_{23} - \lambda_{12} + \lambda_{13} \frac{y'}{\sqrt{1+y'^2}} \right) \Big|_{x=0} &= 0 \\ \lambda_{23} - \lambda_{12} - \lambda_{13} \cos \theta &= 0, \end{aligned} \quad (\text{A.2.9})$$

with the contact angle θ . Resolving for $\cos \theta$ yields the Young-condition (6.2.1).

A.3 Line integral expression of dipolar energy and pressure

It is

$$\frac{1}{\rho^3} = \nabla_1 \cdot \frac{(\mathbf{r}_1 - \mathbf{r}_2)}{\Delta(\rho + \Delta)\rho} \quad (\text{A.3.1})$$

with $\rho = \sqrt{|\mathbf{r}_1 - \mathbf{r}_2|^2 + \Delta^2}$. Application of Green's theorem

$$\int_A \nabla \Phi dA = \oint_{\partial A} \mathbf{n} \Phi ds, \quad (\text{A.3.2})$$

where Φ denotes an arbitrary potential, yields the line integral expression of the pressure integral

$$\int_{A_1} \frac{dA_1}{\rho^3} = \int_{\partial A_1} \mathbf{n}_1 \cdot \frac{(\mathbf{r}_1 - \mathbf{r}_2)}{\Delta(\rho + \Delta)\rho} ds_1. \quad (\text{A.3.3})$$

It holds

$$\frac{1}{\rho^3} = -\nabla_1 \cdot \nabla_2 \frac{\ln(\rho + \Delta)}{\Delta}. \quad (\text{A.3.4})$$

Twice application of Green's theorem (A.3.2) yields the line integral expression of the dipolar energy

$$\int_{A_1} \int_{A_2} \frac{dA_1 dA_2}{\rho^3} = \int_{\partial A_1} \int_{\partial A_2} \frac{\mathbf{n}_1 \cdot \mathbf{n}_2 \ln(\rho + \Delta)}{\Delta} ds_1 ds_2. \quad (\text{A.3.5})$$

A.4 Scaling laws

A.4.1 shape invariant scaling

In the theoretical model a somewhat arbitrary distinction has been made between short range interactions adsorbed into a bare line tension and long range dipole-dipole interactions taken into account at length scales larger than the scale parameter Δ . The theory is constructed in order to explain the macroscopic shapes of domains. If such a theory makes any sense, the macroscopic shapes should not depend on the choice of scale parameter Δ provided the typical length scale of the macroscopic shapes (the radius of curvature of the shapes) is large compared to Δ . For a meaningful theory there must exist a transformation from the microscopic parameters λ, p, Δ onto renormalized parameters λ^*, p^* , and Δ , where in terms of renormalized parameters the shapes are functions of the renormalized parameters only and Δ drops out of the equations. If such a transformation would not exist, then all the macroscopic details would depend on an arbitrary choice of the parameter Δ making the theory meaningless. Equilibrium shapes are determined by the Young Laplace equation, i.e. the shapes satisfy the equation

$$\frac{\delta F}{\delta \mathbf{r}_{ij}(s_{ij})} = 0 \quad (\text{A.4.1})$$

Now take an arbitrary not necessarily equilibrium shape $\mathbf{r}_{ij}(s_{ij})$. Calculate the functional derivative $\delta F / \delta \mathbf{r}_{ij}(s_{ij})$. In the limit $\lim_{\kappa\Delta \rightarrow 0}$ and in terms of renormalized quantities this functional derivative should not depend on Δ , i.e.:

$$\lim_{\kappa\Delta \rightarrow 0} \frac{\partial}{\partial \Delta} \left[\left(\frac{\delta F}{\delta \mathbf{r}_{ij}(s_{ij})} \right)_{\mathbf{x}_n} \right]_{\lambda_{ij}^*, p^*} = 0, \quad (\text{A.4.2})$$

Equation (A.4.2) is the renormalization group equation, defining (up to some constants) the renormalized line tension and pressure. If it holds for any shape, so it does for an equilibrium shape. Hence, if the functional derivative vanishes for a certain shape and set of bare parameters λ, p , and Δ , it does vanish on a whole one dimensional family of parameters defined by $\lambda^*(\lambda, p, \Delta) = \text{const}$ and $p^*(\lambda, p, \Delta) = \text{const}$. The shapes are independent of Δ in terms of renormalized quantities. Writing the functional derivative (Appendix A.2) using the line integral expression of the dipole energy (Appendix A.3) yields:

$$\frac{\delta F}{\delta \mathbf{r}_{ij}(s_{ij})} = \left[\lambda_{ij} \kappa_{ij}(s_{ij}) - p_{ij} + \sum_{\{kl\}} \mu_{ij} \mu_{kl} \int_0^{P_{kl}} ds_{kl} \frac{\mathbf{n}_{kl} \cdot (\mathbf{r}_{ij} - \mathbf{r}_{kl})}{\Delta(\rho + \Delta)\rho} \right] \mathbf{n}_{ij}. \quad (\text{A.4.3})$$

(Compare with [54]). Making use of

$$\frac{1}{\Delta(\rho + \Delta)\rho} = \frac{1}{\Delta(\mathbf{r}_{kl} - \mathbf{r}_{ij})^2} - \frac{1}{\rho(\mathbf{r}_{kl} - \mathbf{r}_{ij})^2} \quad (\text{A.4.4})$$

and the fact that

$$\nabla \cdot \frac{(\mathbf{r} - \mathbf{r}')}{(\mathbf{r} - \mathbf{r}')^2} = 2\pi\delta(\mathbf{r} - \mathbf{r}') \quad (\text{A.4.5})$$

(with the δ -function) and taking the derivative of (A.4.3) with respect to Δ at fixed renormalized quantities results in

$$\begin{aligned} \frac{\partial}{\partial\Delta} \left[\left(\frac{\delta F}{\delta \mathbf{r}_{ij}(s_{ij})} \right)_{\mathbf{x}_n} \right]_{\lambda_{ij}^*, p^*} &= \\ \left[\left(\frac{\partial \lambda_{ij}}{\partial \Delta} \right)_{\lambda_{ij}^*} \kappa_{ij}(s_{ij}) - \left(\frac{\partial p_{ij}}{\partial \Delta} \right)_{p^*} - \frac{(\mu_i^2 - \mu_j^2)\pi}{\Delta^2} + \sum_{\{kl\}} \mu_{ij} \mu_{kl} \int_0^{P_{kl}} ds_{kl} \frac{\Delta \mathbf{n}_{kl} \cdot (\mathbf{r}_{ij} - \mathbf{r}_{kl})}{(\mathbf{r}_{ij} - \mathbf{r}_{kl})^2 \rho^3} \right] \mathbf{n}_{ij}. \end{aligned} \quad (\text{A.4.6})$$

The integral on the right hand side of (A.4.6) vanishes in the limit $\lim_{\kappa\Delta \rightarrow 0}$ everywhere provided $(\mathbf{r}_{ij} - \mathbf{r}_{kl})^2$ remains finite. The expression $(\mathbf{r}_{ij} - \mathbf{r}_{kl})^2$ only vanishes, if the ij boundary coincides with the kl boundary i.e. if $\mathbf{r}_{kl}(s_{kl}) = \mathbf{r}_{ij}(s'_{ij})$. We may expand the expression

$$\frac{\mathbf{n}'_{ij} \cdot (\mathbf{r}_{ij} - \mathbf{r}'_{ij})}{(\mathbf{r}_{ij} - \mathbf{r}'_{ij})^2 \rho^3} \quad (\text{A.4.7})$$

around $\mathbf{r}_{ij}(s_{ij})$ with the result:

$$\begin{aligned} \frac{\mathbf{n} \cdot (\mathbf{r} - \mathbf{r}')}{(\mathbf{r} - \mathbf{r}')^2 \rho^3} &\approx \frac{(\mathbf{n} - \kappa(s' - s)\mathbf{t}) \cdot (-(s' - s)\mathbf{t} - \kappa/2(s' - s)^2\mathbf{n})}{(s' - s)^2 \sqrt{(s' - s)^2 + \Delta^2}^3} \\ &= \frac{\kappa/2}{\sqrt{(s' - s)^2 + \Delta^2}^3} \end{aligned} \quad (\text{A.4.8})$$

Inserting (A.4.8) into (A.4.6) and taking the limit $\lim_{\Delta \rightarrow 0}$ results in

$$\begin{aligned} \lim_{\kappa\Delta \rightarrow 0} \frac{\partial}{\partial\Delta} \left[\left(\frac{\delta F}{\delta \mathbf{r}_{ij}(s_{ij})} \right)_{\mathbf{x}_n} \right]_{\lambda_{ij}^*, p^*} &= \\ &= \left[\left(\frac{\partial \lambda_{ij}}{\partial \Delta} \right)_{\lambda_{ij}^*} \kappa_{ij}(s_{ij}) - \left(\frac{\partial(p_{ij} - \frac{\pi(\mu_i^2 - \mu_j^2)}{\Delta})}{\partial \Delta} \right)_{p^*} + \lim_{\kappa\Delta \rightarrow 0} \mu_{ij}^2 \int_{-1}^1 ds \frac{\Delta \kappa_{ij}/2}{\sqrt{s^2 + \Delta^2}^3} \right] \mathbf{n}_{ij}. \\ &= \left[\left(\frac{\partial \lambda_{ij}}{\partial \Delta} \right)_{\lambda_{ij}^*} \kappa_{ij}(s_{ij}) - \left(\frac{\partial(p_{ij} - \frac{\pi(\mu_i^2 - \mu_j^2)}{\Delta})}{\partial \Delta} \right)_{p^*} + \frac{\kappa_{ij} \mu_{ij}^2}{\Delta} \right] \mathbf{n}_{ij}. \\ &= \left[\left(\frac{\partial(\lambda_{ij} - \mu_{ij}^2 \ln \sqrt{A}/\Delta)}{\partial \Delta} \right)_{\lambda_{ij}^*} \kappa_{ij}(s_{ij}) - \left(\frac{\partial(p_{ij} - \frac{\pi(\mu_i^2 - \mu_j^2)}{\Delta})}{\partial \Delta} \right)_{p^*} \right] \mathbf{n}_{ij}. \end{aligned} \quad (\text{A.4.9})$$

If this expression should vanish for any shape defined by κ_{ij} as required by (A.4.2) both partial derivatives in the last line of (A.4.9) must vanish individually. It is easy to see, that the definitions:

$$\lambda_{ij}^* = \lambda_{ij} - \mu_{ij}^2 \ln \frac{\sqrt{A}}{\Delta} \quad (\text{A.4.10})$$

and

$$p^* = p - \frac{(\mu_i^2 - \mu_j^2)\pi}{\Delta} \quad (\text{A.4.11})$$

satisfy the renormalization group equation (A.4.2). A change in Δ at constant renormalized quantities does not change the shape. From this it follows directly, that (4.3.1) is a shape invariant scale transformation. The shape invariance strictly holds only in the limit $\lim_{\kappa\Delta \rightarrow 0}$. At finite Δ the shape changes when performing a shape invariant scale transformation. The changes are most pronounced in regions, where the curvature of the shape boundary is large (near the three phase contact points), while far away from divergencies in the curvature the shape invariance still holds to a very good approximation.

A.4.2 contact angle invariant scaling

In Appendix A.2.2 we have shown that the boundary condition at the three phase contact point satisfies Young's condition with the bare line tensions. Expressing Young's equation in terms of renormalized line tensions leads to an equation which is not independent of Δ . The functional derivative of the free energy with respect to the intersection points satisfies:

$$\frac{\partial}{\partial \Delta} \left[\left(\frac{\delta F}{\delta \mathbf{x}_n} \right)_{\mathbf{r}(s)} \right]_{\lambda_{ij}} = 0, \quad (\text{A.4.12})$$

i.e. the contact point stability is invariant at fixed bare line tensions, not at fixed renormalized line tensions. The derivation of (A.4.12) from (6.2.1) is trivial. As a consequence of this the total variation of the free energy cannot satisfy a renormalization group equation of the kind

$$\lim_{\kappa\Delta \rightarrow 0} \frac{\partial}{\partial \Delta} [\delta F]_{\lambda_{ij}^{**}, p^{**}} = 0, \quad (\text{A.4.13})$$

Therefore the entire monolayer structure depends on all three parameters λ , Δ and p . It is the boundary condition at the three phase intersection point, where Δ reenters into the renormalized equations. This does not render the theory meaningless, as the stability condition at the contact point is clearly a microscopic condition, even if in the current frame it is an equation somewhat extrapolated from the macroscopic concept of infinitely sharp phase boundaries. Ultimately, when the dipole-dipole interaction really dominates, all droplets must dewet the phase boundaries, such that no three phase intersection points exist, and the pattern becomes completely shape invariant under shape invariant scale transformations. For the pendant droplet in the current paper a droplet exceeding a maximum size must disjoin into a small droplet partially wetting the LC-wall and a second disjoined droplet, detaching from the wall. Indeed the droplet of size $A = 8.9 * 10^{-10} \text{m}^2$ is the largest partially wetting droplet observed in the monolayer ever, while LE-droplets of larger size are observed frequently inside the gaseous phase.

A.5 Foam energy minimization

Since $\left. \frac{\partial}{\partial A} AN \right|_{\Phi} = \left. \frac{\partial}{\partial A} A_{\text{total}} \Phi \right|_{\Phi} = 0$ the equilibrium condition (5.1.3) corresponds to minimizing the function F^*

$$\left. \frac{\partial F^*}{\partial A} \right|_{\Phi, \Delta, \lambda, \mu^2} = 0, \quad \text{where} \quad F^* = \frac{F - F_0}{AN} - \frac{\mu^2 \pi}{\Delta}. \quad (\text{A.5.1})$$

It has been shown by de Koker and McConnell [40] that F^* is invariant to shape invariant scaling transformation and so - similar to \mathbf{r} - it can be expressed in the form:

$$F^*(\lambda, \mu^2, \Delta, A, \Phi) = \frac{\mu^2}{\sqrt{A}} \tilde{F}^*(\tilde{\lambda}^*, \Phi), \quad (\text{A.5.2})$$

with the dimensionless \tilde{F}^* .

With $\partial \tilde{\lambda}^* / \partial A = -1/(2A)$ one finds (5.1.4), which determines a relation between the interaction parameter $\tilde{\lambda}^*$ and the area fraction Φ . We express the solution of equation (5.1.4) in the form:

$$\tilde{\lambda}^* = \tilde{\lambda}_0^* - Y(\Phi), \quad (\text{A.5.3})$$

with $\tilde{\lambda}_0^*$ defined in (5.1.7). Using the definition of $\tilde{\lambda}^*$ (5.1.1) yields equation (5.1.6).

For numerical minimization we used the expression

$$\tilde{F} = -\frac{1}{2} \oint_{\substack{\text{central domain} \\ \text{boundary}}} \oint_{\substack{\text{all domain} \\ \text{boundaries}}} \frac{d\tilde{\mathbf{s}} \cdot d\tilde{\mathbf{s}}'}{\sqrt{(\tilde{\mathbf{r}} - \tilde{\mathbf{r}}')^2 + \Delta^2/A}} + (\lambda/\mu^2 - 1) \oint_{\substack{\text{central domain} \\ \text{boundary}}} d\tilde{s}, \quad (\text{A.5.4})$$

where the integration over s (s') is performed along the interface of the central domain (all domains). We fixed without loss of generality $\sqrt{A}/\Delta = 100$. A Newton procedure has been used in order to solve equation (5.1.4). The accuracy of the calculated interaction parameter $\tilde{\lambda}^*$ is about ± 0.01 .

A.6 Numerical solution of the Young-Laplace-equation for an ideal foam

The procedure is similar to the numerical solution of the Young-Laplace-equation for a pendant droplet on a wall described in appendix A.7. In contrast to that a C_{6v} symmetry is included in the Young-Laplace-equation. The shape of the bubble is described by $\mathbf{r}(s)$, where s is the arc length with values between 0 and the perimeter P . It is chosen in a way such that $\mathbf{r}(0)$ points to an edge of the bubble.

Further we use a damped iteration method instead of normal iteration in appendix A.7:

$$\kappa_{n+1}(s) = (1 - q)\kappa_n(s) + q \left(\frac{2\pi}{P} - \frac{\mu^2}{\lambda} \delta I_n(s) \right), \quad \text{with} \quad (\text{A.6.1})$$

$$\delta I_n(s) = I_n(s) - \frac{12}{P} \int_0^{P/12} ds' I_n(s'), \quad \text{with} \quad (\text{A.6.2})$$

$$I_n(s) = -12 \sum_{i=\text{all bubbles}} \int_0^{P/12} ds' \frac{\mathbf{n}'_n \cdot (\mathbf{r}_n - \mathbf{r}'_n)}{(\mathbf{r}_n - \mathbf{r}'_n)^2 \rho_n}, \quad (\text{A.6.3})$$

where n denotes the iteration step and $0 < q \leq 1$ the damping factor. The choice of $q = 0.5$ showed best results.

The curvature $\kappa_{n+1}(s)$ determines the shape $\mathbf{r}_{n+1}(s)$ and the interaction integral $\delta I_{n+1}(s)$ also described in appendix A.7. As in appendix A.7 the perimeter P is replaced by the bubble area \tilde{A} by application of a regula falsi iteration. The procedure is repeated until the bubble area \tilde{A} equals 1 with sufficient precision. As a result we obtain the bubble shape $\tilde{\mathbf{r}}(s)$ as function of the dimensionless parameters $(\lambda/\mu^2, \Delta/\sqrt{\tilde{A}}, \Phi)$, where $\sqrt{\tilde{A}}/\Delta = 100$ is kept fixed.

The arc-segment is discretized by 100 sampling points, i.e. 1200 sampling points for the whole domain. So Δ is larger than the numerical step width and smaller than the curvature radius ($ds < \Delta < \kappa_{\min}^{-1}$), a necessary condition for the validity of the scaling law and equation (5.1.1).

A.7 Numerical solution of the Young-Laplace-equation for a pendant droplet

Finding theoretical equilibrium droplet shapes is equivalent to finding solutions of the Young-Laplace equation (4.2.1) and Young's-condition (6.2.1). These two equations define a nonlinear set of integro differential equations and are solved numerically. The calculation time can be reduced drastically if the line integral expression (A.3.3) instead of the surface integral representation in (4.2.1) is used. For further use we transform (A.3.3) in order to remove the divergency in the integral. We drop the subscripts characterizing the position, tangent vector, normal vector, arc length and curvature of the LE/G boundary. Then we multiply the line integral expression of (4.2.1) with $[\delta(s - s') - \frac{1}{P}]$ and integrate over the entire LE/G-interface to obtain:

$$\lambda_{\text{LE/G}} \left(\kappa(s') - \frac{2\theta}{P} \right) + \sum_{\{kl\}} \mu_{\text{LE/G}} \mu_{kl} \int_0^P ds \int_0^{P_{kl}} ds_{kl} \left[\delta(s - s') - \frac{1}{P} \right] \frac{\mathbf{n}_{kl} \cdot (\mathbf{r} - \mathbf{r}_{kl})}{\Delta(\rho + \Delta)\rho} = 0. \quad (\text{A.7.1})$$

where we have made use of $\kappa = d\phi/ds$ with ϕ the angle of the tangent vector with respect to some reference direction. Also the total angular change in orientation of the LE/G-interface

equals twice the contact angle θ with the LC-boundary. Collecting the terms in equation (A.7.1) proportional to $\mu_{\text{LE/G}}$ and to $\mu_{\text{LC/G}}$ we might rewrite it as (using (4.4.7,4.4.8)):

$$\kappa(s) = \frac{2\theta}{P} - \frac{\tilde{\mu}}{\tilde{\lambda}_{\text{LE/G}}} \delta I_{\text{LE}}(s) - \frac{1}{\tilde{\lambda}_{\text{LE/G}}} \delta I_{\text{LC}}(s). \quad (\text{A.7.2})$$

The scale parameter Δ is chosen in the order of μm , such that its product with the curvature remains small $\Delta\kappa \ll 1$, but larger than the numerical integration step width ds .

The self interaction integral I_{LE} is defined by:

$$I_{\text{LE}}(s) = - \oint_{\partial A_{\text{LE}}} ds' \frac{\mathbf{n}' \cdot (\mathbf{r} - \mathbf{r}')}{(\mathbf{r} - \mathbf{r}')^2 \rho}, \quad (\text{A.7.3})$$

where we have made use of

$$\oint_{\partial A_{\text{LE}}} ds' \frac{\mathbf{n}' \cdot (\mathbf{r} - \mathbf{r}')}{\Delta(\rho + \Delta)\rho} = \frac{\pi}{\Delta} - \oint_{\partial A_{\text{LE}}} ds' \frac{\mathbf{n}' \cdot (\mathbf{r} - \mathbf{r}')}{(\mathbf{r} - \mathbf{r}')^2 \rho}. \quad (\text{A.7.4})$$

The LC droplet interaction integral I_{LC} reads:

$$\begin{aligned} I_{\text{LC}}(s) &= \int_{\text{half plane}} \frac{dA'}{\rho^3} \\ &= \frac{2}{\Delta} \operatorname{arccot} \frac{-\mathbf{n}_{\text{LC}} \cdot (\mathbf{r} - \mathbf{r}_{\text{LC}})}{\Delta} \end{aligned} \quad (\text{A.7.5})$$

Here \mathbf{n}_{LC} is the inward normal to the LC-half plane and \mathbf{r}_{LC} lies on the LC-interface. The integrals $\delta I_{\text{LE}}(s)$ and $\delta I_{\text{LC}}(s)$ are defined via:

$$\delta I_j(s) = I_j(s) - \frac{1}{P} \int_0^P ds' I_j(s') \quad (\text{A.7.6})$$

The simplest procedure to resolve the integro differential equation (A.7.2) is to iterate it in the form

$$\kappa_{n+1}(s) = \frac{2\theta}{P} - \frac{\tilde{\mu}}{\tilde{\lambda}_{\text{LE/G}}} \delta I_{\text{LE},n}(s) - \frac{1}{\tilde{\lambda}_{\text{LE/G}}} \delta I_{\text{LC},n}(s), \quad (\text{A.7.7})$$

and integrate to the new shape

$$\phi_{n+1}(s) = \phi_0 + \int_0^s ds' \kappa_{n+1}(s'), \quad (\text{A.7.8})$$

$$\mathbf{t}_{n+1}(s) = \begin{pmatrix} \cos \phi_{n+1}(s) \\ \sin \phi_{n+1}(s) \end{pmatrix}, \quad (\text{A.7.9})$$

$$\mathbf{r}_{n+1}(s) = \int_0^s ds' \mathbf{t}_{n+1}(s'), \quad (\text{A.7.10})$$

$$\mathbf{n}_{n+1}(s) = \begin{pmatrix} 0 & -1 \\ 1 & 0 \end{pmatrix} \mathbf{t}_{n+1}(s), \quad (\text{A.7.11})$$

where n denotes the iteration step. If the procedure is converging during iteration the shape \mathbf{r}_n is approaching the final shape \mathbf{r}_∞ fulfilling the Young-Laplace-equation (A.7.2). The perimeter P of the LE/G droplet interface is conserved during this procedure.

The iteration procedure showed good convergence in a large range of parameters. Starting for instance with $\kappa_0(s) = \text{const.}$ (circle) repeated application of equations (A.7.8-A.7.11), (A.7.3), and (A.7.5-A.7.7) may lead to shapes fulfilling equation (A.7.2) for a given set $(\tilde{\mu}, \tilde{\lambda}_{\text{LE/G}}, \Delta, P, \theta)$. The iteration procedure was successful for sufficiently small droplet areas. Droplets in a parameter range where shape instabilities occur did not converge.

In order to replace the perimeter P by the droplet area

$$A = -\frac{1}{2} \oint_{\partial A_{\text{LE}}} ds \mathbf{r} \cdot \mathbf{n}, \quad (\text{A.7.12})$$

we applied a regula falsi iteration, i.e. the converged droplet $\mathbf{r}(s)$ is rescaled to the target area A_0 . The new droplet is taken as initial droplet for another droplet shape iteration:

$$\tilde{\mathbf{r}}(\tilde{s}) = \gamma \mathbf{r}(\tilde{s}/\gamma), \quad (\text{A.7.13})$$

where

$$\gamma = \sqrt{\frac{A_0}{A}}, \quad (\text{A.7.14})$$

and \tilde{s} ranges from 0 to $\tilde{P} = \gamma P$. The procedure is repeated until the droplet area A equals A_0 with sufficient precision. As a result we obtain the droplet shape $\mathbf{r}(s)$ with perimeter P as function of the parameters $\tilde{\mu}$, $\tilde{\lambda}_{\text{LE/G}}$, Δ/\sqrt{A} , and θ .

The renormalized pressure is given by:

$$p^* = \frac{\mu_{\text{LE/G}}\mu_{\text{LC/G}}}{P} \left(\theta \tilde{\lambda} + \frac{\tilde{\mu}}{2} \int_0^P ds I_{\text{LE}}(s) + \frac{1}{2} \int_0^P ds I_{\text{LC}}(s) \right) \quad (\text{A.7.15})$$

The renormalized pressure coincides with the left hand side in equations (6.2.5) and (6.2.6).

A.8 Lower limit for phase specific cut-off lengths Δ_i

The Young-equation has only a solution if

$$\cos \theta = \frac{\lambda_{\text{LC/G}} - \lambda_{\text{LC/LE}}}{\lambda_{\text{LE/G}}} \leq 1. \quad (\text{A.8.1})$$

Plugging the general scaling law for the line tension

$$\lambda_{ij,2} = \lambda_{ij,1} - \mu_i \mu_{ij} \ln \frac{\Delta_{i,2}}{\Delta_{i,1}} + \mu_j \mu_{ij} \ln \frac{\Delta_{j,2}}{\Delta_{j,1}}. \quad (\text{A.8.2})$$

into the Young-condition 6.2.1 yields

$$\begin{aligned} & \lambda_{\text{LC/G}}^{1\mu\text{m}} - \lambda_{\text{LC/LE}}^{1\mu\text{m}} - \mu_{\text{LC/G}} \left(\mu_{\text{LC}} \ln \frac{\Delta_{\text{LC}}}{1\mu\text{m}} - \mu_{\text{G}} \ln \frac{\Delta_{\text{G}}}{1\mu\text{m}} \right) + \mu_{\text{LC/LE}} \left(\mu_{\text{LC}} \ln \frac{\Delta_{\text{LC}}}{1\mu\text{m}} - \mu_{\text{LE}} \ln \frac{\Delta_{\text{LE}}}{1\mu\text{m}} \right) \\ & \leq \lambda_{\text{LE/G}} - \mu_{\text{LE/G}} \left(\mu_{\text{LE}} \ln \frac{\Delta_{\text{LE}}}{1\mu\text{m}} - \mu_{\text{G}} \ln \frac{\Delta_{\text{G}}}{1\mu\text{m}} \right) \end{aligned}$$

Collecting the terms and rearrange them leads to

$$\lambda_{\text{LC/G}}^{1\mu\text{m}} - \lambda_{\text{LC/LE}}^{1\mu\text{m}} - \lambda_{\text{LE/G}}^{1\mu\text{m}} - \mu_{\text{LC}} \ln \frac{\Delta_{\text{LC}}}{1\mu\text{m}} \mu_{\text{LE/G}} + \mu_{\text{G}} \ln \frac{\Delta_{\text{G}}}{1\mu\text{m}} \mu_{\text{LC/LE}} + \mu_{\text{LE}} \ln \frac{\Delta_{\text{LE}}}{1\mu\text{m}} (\mu_{\text{LE/G}} - \mu_{\text{LC/G}}) \leq 0 \quad (\text{A.8.3})$$

Plugging in the experimental values for the line tensions $\lambda_{\text{LE/G}}^{1\mu\text{m}} = 0.32$ pN and $\lambda_{\text{LC/G}}^{1\mu\text{m}} - \lambda_{\text{LC/LE}}^{1\mu\text{m}} = 0.094$ pN as well as $\mu_{\text{LE}} = 2.85 \times 10^{-7} \sqrt{\text{N}}$, $\mu_{\text{G}} = 1.19 \times 10^{-7} \sqrt{\text{N}}$ and $\mu_{\text{LC}} = 5.94 \times 10^{-7} \sqrt{\text{N}}$ in this inequation yields:

- the smaller Δ_{G} the smaller the left hand side of the inequation
- the bigger Δ_{LE} the smaller the left hand side of the inequation
- the bigger Δ_{LC} the smaller the left hand side of the inequation

If $\Delta_{\text{LE}} = \Delta_{\text{LC}} = 10$ nm are set to their maximum acceptable value within the interpretation as length scale of van-der-Waals interaction then Δ_{G} has to be smaller than 0.1\AA in order to obtain a real contact angle. The wetting cannot be explained with phase specific Δ_i in the range of some \AA to several nm.

A.9 Mass action law for monomer-cluster reaction considering entropy in the cluster size

Consider N_{g} gas molecules in chemical equilibrium with N_{c} clusters of the average aggregation number $\langle n \rangle$. The total number of molecules shall be conserved

$$N = \langle n \rangle N_{\text{c}} + N_{\text{g}}. \quad (\text{A.9.1})$$

The size of the clusters shall be variable (≥ 1) and the binding energy per molecule ϵ in a cluster shall be a constant. In real systems clusters smaller than the critical nucleation radius are not stable. The entropy in the model is a bit bigger than in real systems and gives an upper limit of the effect. The entropy from the cluster-arrangement is proportional to the logarithm of the number of micro states realizing the macro state of N_{c} clusters made of $\langle n \rangle N_{\text{c}}$ molecules¹. Throw $N_{\text{c}} - 1$ cuts (without recurrence) on the $\langle n \rangle N_{\text{c}} - 1$ 'cutting places'. Since the cuts

¹Calculation: Number the clusters from 1 to N_{c} and the molecules used for the cluster formation from 1 to $\langle n \rangle N_{\text{c}}$

and the cutting places are not distinguishable there exist $\langle n \rangle N_c - 1$ over $N_c - 1$ possibilities. Distribute the molecule pieces on the clusters according to their number.

$$\begin{aligned} S_c &= k \ln \frac{(\langle n \rangle N_c - 1)!}{(\langle n \rangle N_c - N_c)!(N_c - 1)!} \\ &\approx k((\langle n \rangle N_c - 1) \ln(\langle n \rangle N_c - 1) - (\langle n \rangle - 1)N_c \ln((\langle n \rangle - 1)N_c) - (N_c - 1) \ln((\langle n \rangle - 1)N_c)), \end{aligned} \quad (\text{A.9.2})$$

where the Stirling formula is used in order to obtain the approximation valid for large numbers $N_c \gg 10$. The equation can be simplified and one finds for large N_c

$$S_c = kN_c \ln \frac{\langle n \rangle^{\langle n \rangle}}{(\langle n \rangle - 1)^{\langle n \rangle - 1}} \quad (\text{A.9.3})$$

So the total free energy of the system is the sum of the binding energy, the entropy of the unbound gas molecules (assumed is ideal mixing), the mixing entropy of the cluster-location points and the entropy arising from the cluster size:

$$F = \langle n \rangle N_c \epsilon - N_g kT \ln C_g - N_c kT \ln C_c + TS_c, \quad (\text{A.9.4})$$

where C_g denotes the concentration of gas molecules (number of molecules per unit area) and C_c denotes the concentration of clusters. In thermodynamic equilibrium the partial derivative of the free energy with respect to the number of clusters vanishes

$$\frac{\partial F}{\partial N_c} = 0. \quad (\text{A.9.5})$$

Solving this equation leads to an equation similar to the mass action law

$$\frac{\frac{(\langle n \rangle - 1)^{\langle n \rangle - 1}}{\langle n \rangle^{\langle n \rangle}} C_c}{C_g^{\langle n \rangle}} = K(\epsilon, \langle n \rangle, T), \quad (\text{A.9.6})$$

where K is the equilibrium constant depending on materials parameters and the temperature T . The coefficient $\frac{(\langle n \rangle - 1)^{\langle n \rangle - 1}}{\langle n \rangle^{\langle n \rangle}}$ is a materials constant and can be absorbed by the equilibrium constant

$$\frac{C_c}{C_g^{\langle n \rangle}} = K'(\epsilon, \langle n \rangle). \quad (\text{A.9.7})$$

Ergo: the variety in size of the clusters has no effect on the shape of the isotherm except in a change of the equilibrium constant.

A.10 Monolayer isotherm with impurity

Using equation (8.5.3) the fraction of substance and impurity in the liquid phase can be expressed in terms of c^* , π_0 , π_0^* , α_1 and Φ :

$$\Phi_1 = \frac{\alpha_1 \pi_0^* \Phi + 1 - \Phi}{c^*(\alpha_1 \pi_0 \Phi + 1 - \Phi) + \alpha_1 \pi_0^* \Phi + 1 - \Phi} \quad (\text{A.10.1})$$

Using then equations (8.5.1) one can calculate the pressures π , π^* and $\pi_{\text{total}} = \pi + \pi^*$. One finds for the molecular area

$$\alpha = \frac{1}{\alpha_1\pi\Phi + \Phi_1(1 - \Phi)}. \quad (\text{A.10.2})$$

A.11 Software

This appendix contains special information on the software and is addressed especially to future group members.

A.11.1 Manual

On the whole the controlling software is self-explanatory. In the corners measured values as well as date and time are shown (figure A.11.1). The up/down buttons in the lower left allow the manipulation of the target area. Clicking the checkmark starts the motion, another mouse click on the same button stops the motion. The velocity of barrier movement can be manipulated by the up/down buttons in the lower right. The menu-button in the upper right opens another window where the concentration and spread volume of the used sample can be entered (needed for the calculation of molecular area) and calibration of area and pressure can be performed. The program can be stopped by clicking on the cross button in the upper right. The input line on the bottom allows to add comments also visible on the recorded video tape.

A.11.2 Multimeters

Two multimeters (METEX-22, Digitek DT-4000ZC) purchased from Conrad electronics with RS-232 interface were used. The data transfer and interpretation has been implemented in Delphi using the component 'CommPortDriver' downloaded from the world wide web (www) [128]. The provided manual of the METEX-22 contains all relevant information on the data format. The transfer parameter have to be set to the following values:

- 2400 baud transfer rate
- 7-bit ASCII data format
- no parity
- 2 stop bits

In order to start the data transfer from the PC a letter 'D' has to be sent.

The manual of the Digitek DT-4000ZC does not contain a description of the data format. The information was got from the www [129]: The multimeter always sends data if the RS232-button on the multimeter is activated. So here it is not necessary to send a request from the

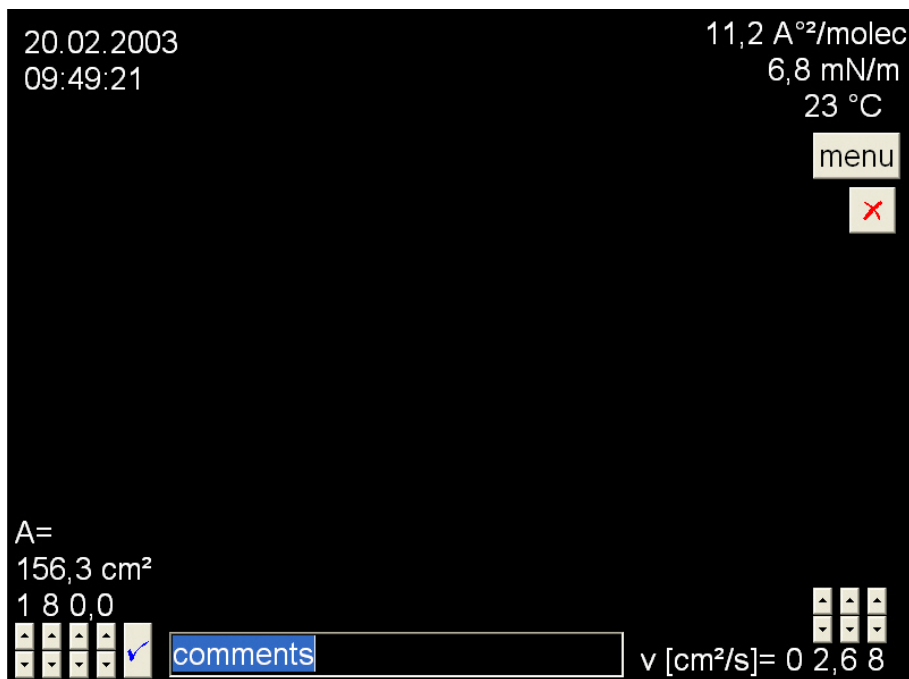


Figure A.11.1: Screenshot of the film balance control software. The computer image and fluorescence image from the SIT camera (positioned in the center) are overlaid by a Genlock adapter. Upper left corner: date and time. Upper right corner: area per molecule, surface pressure, temperature. Lower left corner: actual area and target area. Lower right corner: barrier velocity.

PC. The information of all display segments is encoded in 14 data bytes which are always repeated. The transfer parameter have to be set to

- 2400 baud transfer rate
- 8 data bits
- no parity
- one stop bit.

The higher order half byte contains the number of the byte (1-14) and the lower order half byte contains the information of the display segments as listed in the table (the number in the first row is the number of the byte).

	1.	2.	3.	4.	5.	6.	7.	8.	9.	10.	11.	12.	13.	14.
2 ⁰	RS232	a1	a2	b1	b2	c1	c2	d1	d2	Dio	Sound	Hold	Bat	
2 ¹	Auto	a6	a7	b6	b7	c6	c7	d6	d7	K	M	Δ	Hz	HFE
2 ²	DC	a5	a3	b5	b3	c5	c3	d5	d3	n	%	Ω	V	°C
2 ³	AC	S	a4	p1	b4	p2	c4	p3	d4	μ	m	F	A	

The denotation of the display segments is shown in figure A.11.2.

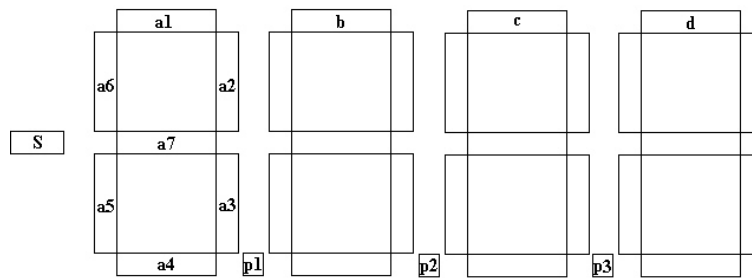


Figure A.11.2: Denotation of display segments.

A.11.3 Stepper motors

The stepper motors are controlled by a PC card from PI. The procedures and functions are in the unit 'motorctrl.pas' which uses a DLL file provided by PI. Additionally to the provided procedures and functions well described in the manual the following procedures and functions were added:

- **function** motorsteuerung_init:integer

Call this procedure in the beginning of the program. The procedure reads the position of the barriers from hard disc and initializes the motor control card. Before break up of the program the positions of the barriers have to be saved. Declare `f:textfile`; `l1,l2:longint` and use the following code:

```
set_vel(1,0); set_vel(2,0);
assignfile(f,'parameter.dat');
rewrite(f);
l1:=get_pos(1); l2:=get_pos(2);
writeln(f,inttostr(l1));
writeln(f,inttostr(l2));
closefile(f);
```

The function returns an error code, the value is 0 if no error occurred.

- **function** postoflaeche(pos1,pos2:longint):extended;

Converts motor counts in the corresponding area between the barriers (in cm^2). The variables `pos1` and `pos2` are the positions of the motors in counts.

- **procedure** flaecheeinstellen(fl:extended);

Starts the motion of the barriers to the target area `fl` (in cm^2). If the target area is reached then the motion stops. The velocity of the motion is set with the procedure `set_vel`.

- **procedure** `area_calibration`;

Sets the velocity to the standard calibration value. Then moves the barriers to maximum area (until they touch the limit switches). This area is taken as the standard maximum area. Parameters of the film balance are saved in the file 'einstellungen.dat'. To read them out use the code:

```
assignfile(f,'einstellungen.dat');
reset(f);
readln(f,s);
maximalflaeche:=strtofloat(s);
readln(f,s);
minimalflaeche:=strtofloat(s);
readln(f,s);
maximum_counts:=strtoint(s);
readln(f,s);
flaeche_pro_count:=strtofloat(s);
closefile(f);
```

where `f:textfile`; `s:string`; `maximalflaeche,minimalflaeche:extended` (maximum area and minimum area in cm^2); `maximum_counts:longint` (corresponding number of counts between maximum and minimum area); `flaeche_pro_count` (area per count in cm^2/count).

Note: If the program is interrupted in another way than by clicking the cross-button the area has to be calibrated again.

List of Figures

1.0.1 Surfactants	1
2.1.1 Film balances - sketch	3
2.1.2 Principle of fluorescence	4
2.1.3 Images by fluorescence microscopy and BAM	5
2.2.1 Apparatus	6
2.3.1 XY table	8
3.1.1 Dipolar repulsion	10
3.2.1 Droplet fusion	13
3.4.1 Shape instabilities	16
3.4.2 Connectivities of periodic structures	16
4.1.1 3D pendant drop in gravity	17
4.2.1 Monolayer sketch	18
4.4.1 Pendant droplets in MOD monolayer	20
4.4.2 Pendant droplet tensiometry - calculation example	22
5.0.1 Foams observed in myristic acid monolayer	26
5.1.1 Sketch - ideal foam	27
5.2.1 Theoretical bubble shapes of ideal foams	28
5.2.2 Plot - Bubble size versus area fraction	29
5.2.3 Plot - shape parameter versus area fraction	30
5.3.1 Plot - bubble deformation in monolayers of myristic and pentadecanoic acid	31
6.0.1 Sketch - wetting	33
6.1.1 Sketch - electro-wetting	35
6.2.1 Contact angle scaling - demo	37
6.2.2 Size dependence of the droplet shape in MOD monolayer	39
6.2.3 Sketch - contact angle fitting	39
6.2.4 Simulated droplets	40

6.2.5 Contact angle scaling - two droplets	41
6.2.6 Contact angle scaling - plot	42
6.2.7 Sketch - wetting regimes	43
6.3.1 Circular segment - sketch	46
6.3.2 Circular segment - results	48
6.3.3 Bifurcation at wetting	49
7.0.1 Biowetting	51
7.2.1 Lipases	54
7.2.2 AMD-TLC analysis	56
7.2.3 Enzyme reaction in monolayer	57
7.2.4 Wetting occurrence	58
8.2.1 DMPA isotherm	60
8.2.2 Phase diagram of MOD monolayer	61
8.3.1 Estimated phase diagram for MOD	64
8.4.1 Isotherms for cluster formation	65
8.5.1 Droplets and Bubbles	69
8.5.2 Demixing transition	70
8.5.3 Calculated isotherms with 0%, 1%, 5% and 10% impurity	71
A.11.1 Screenshot	91
A.11.2 Display segments	92

Bibliography

- [1] M. C. Petty. *Langmuir-Blodgett films: an introduction*. Cambridge University press, 1996.
- [2] J. M. Andreas, E. A. Hauser, and W. B. Tucker. Boundary tension by pendant drops. *J. Phys. Chem.*, 42:1001–1019, 1938.
- [3] M. Lösche, E. Sackmann, and H. Möhwald. A fluorescence microscopic study concerning the phase diagram of phospholipids. *Ber. Bunsenge, Phys. Chem.*, 87:848–852, 1983.
- [4] H. M. McConnell, L. K. Tamm, and R. M. Weis. Periodic structures in lipid monolayer phases transitions. *Proc. Natl. Acad. Sci. (USA)*, 81:3249–3253, 1984.
- [5] D. Hönig and D. Möbius. Direct visualization of monolayers at the air-water interface by Brewster angle microscopy. *J. Phys. Chem.*, 95:4590–4592, 1991.
- [6] S. Hénon and J. Meunier. Microscope at the Brewster angle: Direct observation of first-order phase transitions in monolayers. *Rev. Sci. Instrum.*, 62:936–939, 1991.
- [7] Z. Khattari, E. Hatta, P. Heinig, P. Steffen, Th. M. Fischer, and R. Bruinsma. Cavitation of Langmuir monolayers. *Phys. Rev. E*, 65:041603, 2002.
- [8] N. Uyeda, T. Takenaka, K. Aoyama, M. Matsumoto, and Y. Fujiyoshi. Holes in a stearic-acid monolayer observed by dark-field electron-microscopy. *Nature*, 327:619–621, 1987.
- [9] P. Dutty, Peng J. B, B. Lin, Ketterson J. B, M. Prakash, P. Georgopoulos, and S. Ehrlich. X-ray diffraction studies of organic monolayers on the surface of water. *Phys. Rev. Lett.*, 58:2228–2231, 1987.
- [10] R. G. Greenler. Infrared study of adsorbed molecules on metal surfaces by reflection techniques. *J. Chem. Phys.*, 44:310, 1966.
- [11] G. Binnig, C. F. Quate, and C. Gerber. Atomic force microscopy. *Phys. Rev. Lett.*, 56:930–933, 1986.

- [12] S. Wurlitzer, C. Lautz, M. Liley, C. Duschl, and Th. M. Fischer. Micromanipulation of Langmuir-monolayers with optical tweezers. *J. Phys. Chem. B*, 105:182–187, 2001.
- [13] A. Ashkin. Applications of lasers - radiation pressure. *Science*, 210:4474–, 1980.
- [14] S. Wurlitzer. *Diplomarbeit: Herstellung und Charakterisierung Dünner Schichten*. University of Leipzig, 1996.
- [15] R. J. Demchak and Jr. T. Fort. Surface dipole moments of close-packed un-ionized monolayers at the air-water-interface. *J. Colloid and Interfaces*, 46(2):191, 1973.
- [16] P. Heinig, S. Wurlitzer, P. Steffen, F. Kremer, and Th. M. Fischer. Local surface potentials in the three-phase coexistence region of a Langmuir monolayer. *Langmuir*, 16:10254–10257, 2000.
- [17] H. M. McConnell and V. T. Moy. Shapes of finite two-dimensional lipid domains. *J. Phys. Chem.*, 92:4520–4525, 1988.
- [18] J. G. Petrov, E. E. Polymeropoulos, and H. Möhwald. Three-capacitor model for surface potential of insoluble monolayers. *J. Phys. Chem.*, 100:9860–9869, 1996.
- [19] P. Dynarowicz. Recent developments in the modeling of the monolayers structure at the water/air interface. *Adv. Colloid Interf. Sci.*, 45:215–241, 1993.
- [20] W. Harkins and E. Fischer. Contact potentials and the effects of unimolecular films on surface potentials. I. Films of acids and alcohols. *J. Chem. Phys.*, 1:852–862, 1933.
- [21] A. Alexander and J. Schulmann. Orientation in films of long-chain esters. *Proc. Roy. Soc. Ser. A*, 161:115–127, 1937.
- [22] O. N. Oliveira, Jr., and C. Bonardi. The surface potential of Langmuir monolayers revisited. *Langmuir*, 13:5920–5924, 1997.
- [23] *Physical chemistry of surfaces*. Wiley, 1990.
- [24] C. Helm. PhD thesis, 1988.
- [25] A. Miller, C. Helm, and H. Möhwald. The colloidal nature of phospholipid monolayers. *Journal de Physique*, 48:693–701, 1987.
- [26] S. Wurlitzer. *Statische und dynamische Eigenschaften von Mikrostrukturen in Langmuir-Monolagen*. PhD thesis, 2001.
- [27] H. M. McConnell, P. A. Rice, and D. J. Benvegnu. Brownian motion of lipid domains in electrostatic traps in monolayers. *J. Phys. Chem.*, 94:8965–8968, 1990.

- [28] D. J. Benvegnu and H. M. McConnell. Surface dipole densities in lipid monolayers. *J. Phys. Chem.*, 97:6686–6691, 1993.
- [29] P. Heinig. *Diplomarbeit: Kontaktwinkeldynamik im Dreiphasengebiet eines Langmuir-filmes*. University of Leipzig, 2000.
- [30] K. J. Klopfer and T. K. Vanderlick. Isothermes in dipalmitoylphosphatidylcholine (DPPC) monolayers: features revealed and features obscured. *J. Coll. & Int. Sci.*, 182:220–229, 1996.
- [31] P. Muller and F. Gallet. First measurement of the liquid- solid line energy in a Langmuir monolayer. *Phys. Rev. Lett.*, 67(9):1106–, 1991.
- [32] P. Muller and F. Gallet. Ordered domains in a Langmuir monolayer: structure and line energy. *Thin Solid Films*, 210/211:138–140, 1992.
- [33] D. J. Benvegnu and H. M. McConnell. Line tension between liquid domains in lipid monolayers. *J. Phys. Chem.*, 96:6820–6824, 1992.
- [34] E. K. Mann, S. Henon, D. Langevin, and J. Meunier. Hydrodynamics of domain relaxation in a polymer monolayer. *Phys. Rev. E*, 51:5708–5720, 1995.
- [35] S. Wurlitzer, P. Steffen, M. Wurlitzer, Z. Khattari, and Th. M. Fischer. Line tension in Langmuir monolayers probed by point forces. *J. Chem. Phys B*, 113(9):3822–3828, 2000.
- [36] S. Wurlitzer, P. Steffen, and Th. M. Fischer. Line tension of Langmuir monolayer phase boundaries determined with optical tweezers. *J. Chem. Phys.*, 112(13):3822–3828, 2000.
- [37] S. Rivière, S. Henon, and J. Meunier. Electrostatic pressure and line tension in a Langmuir monolayer. *Phy. Rev. Lett.*, 75:Nr. 13, 1995.
- [38] S. Wurlitzer, H. Schmiedel, and Th. M. Fischer. Equilibrium size of circular domains in Langmuir monolayers. *J. Chem. Phys.*, 116:10877–10881, 2002.
- [39] H. M. McConnell. Structures and transitions in lipid monolayers at the air-water interface. *Annu. Rev. Phys. Chem.*, 42:171–95, 1991.
- [40] R. de Koker and H. M. McConnell. Circle to dogbone: shapes and shape-transition of lipid monolayer domains. *J. Phys. Chem.*, 97:13419–13424, 1993.
- [41] K. Y. C. Lee and H. M. McConnell. Quantized symmetry of liquid monolayer domains. *J. Phys. Chem.*, 97:9532–9539, 1993.

-
- [42] V. M. Kaganer, H. Möhwald, and P. Dutta. Structure and phase transitions in Langmuir monolayers. *Rev. of modern Phys.*, 71(3):779–819, 1999.
- [43] S. Perkovic and H. McConnell. Cloverleaf monolayer domains. *J. Phys. Chem B*, 101:381–388, 1997.
- [44] M. Seul and D. Andelman. Domain shapes and patterns: The phenomenology of modulated phases. *Science*, 267:476–483, 1995.
- [45] T. K. Vanderlick and H. Möhwald. Mode selection and shape transitions of phospholipid monolayer domains. *J. Phys. Chem.*, 94:886–890, 1990.
- [46] H. M. McConnell and R. de Koker. Note on the theory of the sizes and the shapes of lipid monolayers. *J. Phys. Chem*, 96:7101–7103, 1992.
- [47] J. M. Deutch and F. E. Low. Theory of shape transitions of two-dimensional domains. *J. Phys. Chem*, 96:7097–7101, 1992.
- [48] Z. Khattari and Th. M. Fischer. Shapes of Langmuir monolayer domains in confined geometries. *J. Phys. Chem.*, 106:1677–1683, 2002.
- [49] D. Vanderbilt. Phase segregation and work-function variations on metal surfaces: spontaneous formation of periodic domain structures. *Surf. Sci. Lett.*, 268:L300–L304, 1992.
- [50] Kwok-On Ng and D. Vanderbilt. Stability of periodic domain structures in a two-dimensional dipolar model. *Phys. Rev. B*, 52:2177–2183, 1995.
- [51] K. J. Stine, M. F. Bono, and J. S. Kretzer. Observation of a foam morphology of the liquid-condensed phase of a Langmuir monolayer. *J. of Coll. and Surf. Sci.*, 162:320–322, 1994.
- [52] C. E. Stauffer. The measurement of surface tension by the pendant drop technique. *Journal of Physical Chemistry*, 69(6):1933–1938, 1965.
- [53] D. S. Ambwani and T. Fort. Pendant drop technique for measuring liquid boundary tension. *Surf. Colloid Sci.*, 11:93, 1979.
- [54] P. Heinig, P. Steffen, S. Wurlitzer, and Th. M. Fischer. Two dimensional pendant droplet tensiometry in a Langmuir Monolayer. *Langmuir*, 17(21):6633–6637, 2001.
- [55] S. Dietrich. Grenzflächenstrukturen von Fluiden. *Physik Journal*, 2002.
- [56] K. R. Mecke and S. Dietrich. Effective Hamiltonian for liquid-vapor interfaces. *Phys. Rev. E*, 59:6766–6784, 1999.

- [57] A. Yeung, T. Dabros, and J. Masliyah. Dissipative interfaces and departures from the Young-Laplace equation. *Langmuir*, 13:6597–6606, 1997.
- [58] A. D. Rey. Young-Laplace equation for liquid crystal interfaces. *J. Chem. Phys.*, 113:10820–10822, 2000.
- [59] E. Minkov and A. Novick-Cohen. Droplet profiles under the influence of van der Waals forces. *Euro. J. of applied mathematics*, 12:367–393, 2001.
- [60] D. Weaire and S. Hutzler. *The physics of foams*. Clarendon Press, 1999.
- [61] F. Graner, Y. Jiang, and C. Flament. Equilibrium states and ground state of two-dimensional fluid foams. *Phys. Rev. E*, 63:011402, 2000.
- [62] H. M. Princen. *J. of Coll. and Int. Sci.*, 71:55, 1979.
- [63] J. A. Glazier and D. Weaire. The kinetics of cellular patterns. *J. Phys: Condensed Matter*, 4:1867–1894, 1992.
- [64] *Phil. Mag. B*, 65:473, 1992.
- [65] B. Berge, A. J. Simon, and A. Libchaber. Dynamics of gas bubbles in monolayers. *Phys. Rev. A*, 41:6893–6900, 1990.
- [66] H. M. McConnell. Theory of hexagonal and stripe phases in monolayers. *Proc. Natl. Acad. Sci. USA*, 86:3452–3455, 1989.
- [67] J. P. Kermode and D. Weaire. 2D-froth: a program for the investigation of 2-dimensional froths. *Comp. Phys. Comm.*, 60:75–109, 1990.
- [68] F. Elias, C. Flament, J.-C. Bacri, O. Cardoso, and F. Graner. Two-dimensional magnetic froth: Coarsening and topological correlations. *Phys. Rev. E*, 56:3310–3318, 1997.
- [69] F. Elias, C. Flament, J.-C. Bacri, and S. Neveu. Macro-Organized Patterns in Ferrofluid Layer: Experimental Studies. *J. Phys. I France*, 7:711–728, 1995.
- [70] S. Herminghaus, K. Jakobs, K. Mecke, J. Bischof, A. Fery, M. Ibn-Elhaj, and S. Schlagowski. Spinodal dewetting in liquid crystal and liquid metal films. *Science*, 282:916–919, 1998.
- [71] F. Brochard-Wyart and J. Dailant. Drying of solids wetted by thin liquid-films. *Can. J. Phys.*, 68:1084–1088, 1990.
- [72] G. Reiter. Dewetting of thin polymer films. *Phys. Rev. Lett.*, 68:75–78, 1992.

- [73] C. Quilliet and B. Berge. Electrowetting: a recent outbreak. *Curr. Opin. Coll. Interf. Sci.*, 6:34–39, 2001.
- [74] F. Mugele and S. Herminghaus. Electrostatic stabilization of fluid microstructures. *Appl. Phys. Lett.*, 81, 2002.
- [75] T. Young. An essay on the cohesion of fluids. *Phil. Trans. Royal soc. London*, 95, 1805.
- [76] J. E. McNutt and J. M. Andes. Relationship of the contact angle to interfacial energies. *J. Chem. Phys.*, 30:1300–1303, 1959.
- [77] P. G. de Gennes. Wetting: statics and dynamics. *Rev. Mod. Phys.*, 57(3) Part 1:827–863, 1985.
- [78] G. Lippmann. Relation entre les phénomènes électriques et capillaires. *Ann. Chim. Phys.*, 5:494–549, 1875.
- [79] R. Hoffman. Study of advancing interface . 1. interface shape in liquid-gas systems. *Fluid-Dynamics-New York*, 50:228, 1975.
- [80] R. G. Cox. The dynamics of the spreading of liquids an a solid surface. Part1. Viscous flow. *J. Fluid. Mech.*, 168:169–194, 1986.
- [81] J. P. Hagen and H. M. McConnell. Three-phase intersection points in monolayers. *Colloids and Surfaces*, 102:167–172, 1995.
- [82] R. Pandit and M. E. Fisher. Wetting transitions near bulk triple points. *Phys. Rev. Lett.*, 51(19):1772–1775, 1983.
- [83] J. D. van der Waals. The thermodynamic theory of capillarity under the hypothesis of a continuous variation of density. *J. Stat. Phys.*, 20:200–244, 1979. (translation by J. S. Rowlinson).
- [84] F. P. Buff, R. A. Lovett, and F. H. Stillinger Jr. Interfacial density profile for fluids in the critical region. *Phys. Rev. Lett.*, 15(15):621–623, 1965.
- [85] R. D. Gretz. Line-tension effect in a surface energy model of a cap-shaped condensed phase. *J. Chem. Phys.*, 45:3160–3161, 1966.
- [86] A. I. Milchev and A. A. Binder. Wetting behaviour of nanodroplets: The limits of Young’s rule validity. *Europhys. Lett.*, 56(5):695–701, 2001.
- [87] J. F. Joanny and P. G. de Gennes. Role of long-range forces in heterogeneous nucleation. *J. Coll. Interf. Sci.*, 111:94–101, 1986.

- [88] A. Milchev and K. Binder. Polymer melt droplets adsorbed on a solid wall: a Monte Carlo simulation. *J. Chem. Phys.*, 114:8610–8618, 2001.
- [89] A. Milchev, A. Milchev, and K. Binder. Nanodroplets on a solid plane: wetting and spreading in a Monte Carlo simulation. *Comp. Phys. Comm.*, 146:28–53, 2002.
- [90] Z. Khattari, P. Heinig, S. Wurlitzer, P. Steffen, M. Lösche, and Th. M. Fischer. Wetting in asymmetric quasi-2D systems. *Langmuir*, 18:2273–2279, 2002.
- [91] G. J. Schütz, G. Kada, V. Ph. Pastushenko, and H. Schindler. Properties of lipid microdomains in a muscle cell membrane visualized by single molecule microscopy. *EMBO*, 19:892, 2000.
- [92] C. Souvignet, J. M. Pelosin, S. Daniel, E. M. Chambaz, S. Ransac, and R. Verger. Activation of protein kinase C in lipid monolayers. *The Journal of Biological chemistry*, 206(1):40–44, 1991.
- [93] G. Piéroni, Y. Gargouri, L. Sarda, and R. Verger. Interactions of lipases with lipid monolayers facts and questions. *Advances in Colloid and Interface Science*, 32:341–378, 1990.
- [94] H. M. Verheij, M. C. Boffa, C. Rothen, M. C. Bryckaert, R. Verger, and Gerhard de Haas. Correlation of enzymatic activity and anticoagulant properties of phospholipase A₂. *Eur. J. Biochem.*, 112:25–32, 1980.
- [95] U. Dahmen-Levison and G. Brezesinski. Methyl-branched glycerophosphocholines: monolayer disorder and its effect on the rate of phospholipase A₂ catalyzed hydrolysis. *Phys. Chem. Chem. Phys.*, 2:4605–4608, 2000.
- [96] U. Dahmen-Levison, G. Brezesinski, and H. Möhwald. Monolayer structures of triple-chain phosphatidylcholines as substrates for phospholipases. *Coll. Surf.*, 171:97–103, 2000.
- [97] G. H. Peters, U. Dahmen-Levison, K. de Meijere, G. Brezesinski, S. Toxvaerd, H. Möhwald, A. Svendsen, and P. K. J. Kinnunen. Influence of surface properties of mixed monolayers on lipolytic hydrolysis. *Langmuir*, 16:2779–2788, 2000.
- [98] U. Dahmen-Levison, G. Brezesinski, and H. Möhwald. Specific adsorption of PLA₂ at monolayers. *Thin Solid Films*, 327-329:616–620, 1998.
- [99] C. DeWolf, S. Leporatti, C. Kirsch, R. Klinger, and G. Brezesinski. Phase separation in phosphatidylinositol/phosphatidylcholine mixed monolayers. *Chemistry and Physics of Lipids*, 97:129–138, 1998.

- [100] M. Grandbois, B. Desbat, D. Blaudez, and C. Salesse. Polarization-modulated infrared reflection absorption spectroscopy measurement of phospholipid monolayer hydrolysis by phospholipase C. *Langmuir*, 15:6594–6597, 1999.
- [101] A. Fischer. private communication.
- [102] A. Fischer. *Diplomarbeit (in preparation)*. University of Potsdam.
- [103] Z. Khattari. private communication.
- [104] A. Rietveld and K. Simons. The differential miscibility of lipids as the basis for the formation of functional membrane rafts. *Biochim. et Biophys. Acta*, 1376:467–479, 1998.
- [105] D. Li, J. Gaydos, and A. W. Neumann. The phase rule for systems containing surfaces and lines 1. moderate curvature. *Langmuir*, 5:1133–1140, 1989.
- [106] K. Kjaer, J. Alsnielsen, C. A. Helm, L. A. Laxhuher, and H. Möhwald. Ordering in lipid monolayers studied by synchrotron X-ray-diffraction and fluorescence microscopy. *Phys. Rev. Lett.*, 58:2224–2227, 1987.
- [107] T. Fischer. private communication.
- [108] N. R. Pallas and B. A. Pethica. Liquid-expanded to liquid-condensed transitions in lipid monolayers at the air/water interface. *Langmuir*, 1:509–513, 1985.
- [109] A. Miller and H. Möhwald. Diffusion limited growth of crystalline domains in phospholipid monolayers. *J. Chem. Phys.*, 86(7):4258–4265, 1986.
- [110] T. Gutberlet and D. Vollhardt. Thermally induced domain growth in fatty acid ester monolayers. *J. Coll. Int. Sci.*, 173:429–435, 1995.
- [111] J. Israelachvili. Self-assembly in two dimensions: surface micelles and domain formation in monolayers. *Langmuir*, 10:3774–3781, 1994.
- [112] V. B. Fainerman, D. Vollhardt, and V. Melzer. Equation of state for insoluble monolayers of aggregating amphiphilic monolayers. *J. Phys. Chem.*, 100:15478–15482, 1996.
- [113] V. B. Fainerman and D. Vollhardt. Equations of state for Langmuir monolayers with two-dimensional phase transitions. *J. Phys. Chem.*, 103:145–150, 1999.
- [114] D. Vollhardt and V. Fainerman. Phase transitions in Langmuir monolayers. *Coll. & surf.*, 176:117–124, 2002.
- [115] E. Ruckenstein and B. Li. Surface equation of state for insoluble surfactant monolayers at the air/water interface. *J. Phys. Chem.*, 102:981–989, 1998.

- [116] H. Möhwald. *T. Riste and D. Sherrington (eds): Phase transitions in soft condensed matter*. Plenum press, 1989.
- [117] E. Ruckenstein. On the nature of the liquid expanded/ liquid condensed phase transition in monolayers of polar molecules. *J. coll. & int. sci.*, 196:313–315, 1997.
- [118] V. M. Kaganer, B. Jenichen, F. Schippan, W. Braun, L. Däweritz, and K. H. Ploog. Strain-mediated phase coexistence in heteroepitaxial films. *Phys. Rev. Lett.*, 85(2):341–344, 2000.
- [119] D. C. Agrawal. Surface tension and evaporation: An empirical relation for water. *Phys. Rev. A*, 46:2166–2169, 1992.
- [120] V. B. Fainerman, E. H. Lucassen-Reynders, and R. Miller. Adsorption of surfactants and proteins at fluid interfaces. *Colloids Surfaces*, 143:141–165, 1998.
- [121] M. D. Donohue and J. M. Prausnitz. Combinatorial entropy of mixing molecules that differ in size and shape. A simple approximation for binary and multicomponent mixtures. *Can. J. Chem.*, 53:1586–1592, 1974.
- [122] A. Radhakrishnan and H. M. McConnell. Condensed complexes of cholesterol and phospholipids. *Biophys. J.*, 77:1507–1517, 1999.
- [123] A. Radhakrishnan and H. M. McConnell. Chemical activity of cholesterol in membranes. *Biochemistry*, 39:8119–8124, 2000.
- [124] S. L. Keller, A. Radhakrishnan, and H. M. McConnell. Saturated phospholipids with high melting temperatures for, complexes with cholesterol in monolayers. *J. Phys. Chem. B*, 104:7522–7527, 2000.
- [125] T. Priester, M. Bartoszek, and K. Lunkenheimer. Influence of surface-active trace impurities on the surface properties of aqueous solutions of oligoethylene glycol monoethyl ethers. *J. Coll. Interf. Sci.*, 208:6–13, 1998.
- [126] K. Lunkenheimer, H. J. Pergande, and H. Krüger. Apparatus for programmed high-performance purification of surfactant solutions. *Rev. Sci. Instrum.*, 58:2313–2316, 1987.
- [127] V. Melzer, D. Vollhardt, G. Brezesinski, and H. Möhwald. Similarities in the phase properties of Gibbs and Langmuir monolayers. *J. Phys. Chem.*, 102:591–597, 1997.
- [128] http://sdiclub.tms.ru/files_table.phtml?ipath=ACE.
- [129] <http://www2.brd.nrw.de/schule/physik/material/digitek/digitek.htm>.

List of publications

- P. Heinig and Th. M. Fischer. Long range interaction foams dry at lower gas fraction than short range interaction foams. *submitted*
- P. Heinig, S. Wurlitzer, Th. John, and Th. M. Fischer. Stability criteria for two-dimensional wetting in monolayers. *J. Phys. Chem.* , 106:11951-11960, 2002.
- Z. Khattari, P. Heinig, S. Wurlitzer, P. Steffen, M. Lösche, and Th. M. Fischer. Wetting in asymmetric quasi-2D systems. *Langmuir*, 18:2273-2279, 2002.
- Z. Khattari, E. Hatta, P. Heinig, P. Steffen, Th. M. Fischer, and R. Bruinsma. Cavitation of Langmuir monolayers. *Phys. Rev. E*, 65:041603, 2002.
- P. Heinig, P. Steffen, S. Wurlitzer, and Th. M. Fischer. Two dimensional pendant droplet tensiometry in a Langmuir Monolayer. *Langmuir*, 17:6633-6637, 2001.
- P. Steffen, P. Heinig, S. Wurlitzer, Z. Khattari, and Th. M. Fischer. The translational and rotational drag on Langmuir monolayer domains. *J. Chem. Phys.* , 115:994-997, 2001.
- P. Heinig, S. Wurlitzer, P. Steffen, F. Kremer, and Th. M. Fischer. Local surface potentials in the three-phase coexistence region of a Langmuir monolayer. *Langmuir*, 16:10254-10257, 2000.

Conferences and talks

Oral contributions

P. Heinig, S. Wurlitzer, P. Steffen, and Th. M. Fischer. On 2D wetting in monolayers. *Summer school of interface department*, Schorfheide/Germany, July 22-24, 2002.

P. Heinig. 2D wetting - droplet shapes and contact angles. *Fachübergreifendes Doktorandentreffen am IAPD*, Dresden/Germany, April 20, 2002.

P. Heinig, S. Wurlitzer, P. Steffen, and Th. M. Fischer. On the shapes of 2D wetting droplets. *Nachwuchstage der Kolloidgesellschaft Berlin*/Germany, March 21-22, 2002

P. Heinig, S. Wurlitzer, P. Steffen, and Th. M. Fischer. 2D-Benetzung im Langmuir Monolayer: Tropfenform und Kontaktwinkel. *Doktorandenworkshop: Dünne organische Schichten und biochemische Schichten*. Potsdam/Germany, November 22-23, 2001.

P. Heinig, S. Wurlitzer, P. Steffen, and Th. M. Fischer. On the shapes of 2D wetting droplets. *International Nanostructured Interfacial Technique Symposium*, Zhuhai/China, November 1-6, 2001.

Poster presentations

P. Heinig, T. John, and Th. M. Fischer. Stability criteria for 2D wetting in monolayers. *Gordon Research Conference - Complex Fluids*, Oxford/UK, June 30 - July 4, 2002.

P. Heinig, S. Wurlitzer, P. Steffen, and Th. M. Fischer. Pendant droplet tensiometry in 2D-system with dipolar interaction. *European Conference Organised Films 8*, Lecce/Italy, September 1-7, 2001.

P. Heinig, S. Wurlitzer, P. Steffen, and Th. M. Fischer. 2D-wetting in methyl octadecanoate monolayer. *Doktorandenworkshop des Schwerpunktes Benetzung der DFG*. Günzburg, July 18-21, 2001.

Curriculum vitae

Personal data

name: Peter Heinig
date of birth: July 25 1974
place of birth: Zschopau/Germany
nationality: German

Education

1993 general qualification for university entrance, Kepler-Gymnasium
(Chemnitz/Germany)
1993-1995 undergraduate study of physics and arabic at Kuwait university
(Kuwait city/Kuwait)
1995-1996 civil service
1996-1999 study of physics at the University of Leipzig (Germany)
1999-2000 diploma student at the Max Planck institute for colloids and interfaces (MPI-CI)
(Golm/Germany)
2000 diploma in physics, University of Leipzig (Germany)
2000-present Ph.D. student at the MPI-CI (Golm/Germany)

Acknowledgements

The present work has been funded by the Max-Planck-Society and the German Science Foundation within the program 'Wetting and structure formation at interfaces'. I would like to thank all the people supporting me during my PhD work. The supervision by Th. M. Fischer providing a fruitful research climate is gratefully acknowledged. An important contribution to the success of this dissertation has to be accounted to his guidance and scientific advice. I thank all present and former group members: Z. Khattari, S. Wurlitzer, P. Steffen, A. Fischer, H. Wen, L.-E. Helseth and Y. Ruschel for the friendly cooperation. Furthermore I would like to express my gratitude to Prof. Möhwald for providing a PhD fellowship and for stimulating discussion. I thank the whole interface department for having a valuable and nice time at the institute. Finally, I like to thank H. Frank for proofreading the manuscript and H.B. Kalbsbry for the support in the typesetting with \LaTeX .

Thesen

1. In idealen² 2D Phasenkoexistenzgebieten mit dipolarer Wechselwirkung erfüllen Phasengrenzen im Gleichgewicht die 2D Young-Laplace-Gleichung. Zusätzlich zur 3D Young-Laplace-Gleichung enthält diese einen Term für den elektrostatischen Druck.
2. Kontaktwinkel in den genannten Systemen folgen der Young-Bedingung und sind eine Materialeigenschaft des Systems. Die These wurde durch Experimente in einer Stearinsäuremethylester-Monolage (SME-Monolage) bestätigt.
3. Die Auswertung der Form experimenteller 2D Tropfen erlaubt die Messung von Linienspannung durch hängende-Tropfen-Tensiometrie und wurde in einer SME-Monolage durchgeführt.
4. Hexagonale monodisperse 2D Schäume mit dipolarer Wechselwirkung haben universelle Blasenformen, die nur vom Phasenanteil aber nicht von Materialparametern abhängen.
5. Die Blasengröße in diesen Schäumen wird durch eine ebenfalls universelle Größenfunktion in Einheiten der Gleichgewichtsgröße einer isolierten Blase beschrieben.
6. Sowohl ideale als auch experimentelle 2D Schäume mit repulsiver Dipolwechselwirkung trocknen (=Verformung der Blasen bezüglich der Kreisform) bei kleineren Phasenanteilen der Blasenphase als Schäume ohne langreichweitige Wechselwirkung.
7. Die Cut-off-Länge der dipolaren Wechselwirkung in SME-Monolage ist größer als $0.1 \mu\text{m}$. Der Autor schlägt eine Interpretation als dipolare Korrelationslänge an der Phasengrenze vor.
8. Dipolwechselwirkung von benetzenden 2D Tropfen mit dem 2D Substrat stabilisiert die Tropfen bezüglich Formbifurkationen.
9. Eine Kontrolle des Benetzungsverhaltens der Phasen einer Phospholipid enthaltenden Langmuir-Monolage durch enzymatische Hydrolyse ist prinzipiell möglich.
10. Eine biologische Relevanz dieser Kontrolle des Benetzungsverhalten zur Steuerung der Reaktionskinetik in biologischen Membranen kann vermutet werden.
11. Die wahrscheinlichste Erklärung für die (auch in der Literatur oft reproduzierte) scheinbare Verletzung der Gibbs'schen Phasenregel in Langmuir-Monolagen sind Verunreinigungen während Erklärungen, die auf finite-size-Effekten oder dem Einfluss der langreichweitigen Wechselwirkung beruhen, eher unwahrscheinlich sind.

²2D Phasen im Sinne Gibbs'